Comparison of two avalanche terrain classification approaches:

Avalanche Terrain Exposure Scale - Classified Avalanche Terrain

Master's Thesis

in Atmospheric and Cryospheric Sciences

Submitted to the
Faculty of Geo- and Atmospheric Sciences
of the
University of Innsbruck

in Partial Fulfillment of the Requirements for the Degree of
Master of Science

by
Paula Spannring

Advisors
Ass. Prof. Lindsey Nicholson
Priv.-Doz. Dipl.-Phys. Dr.techn. Jan-Thomas Fischer
Dr. Christoph Mitterer

Innsbruck, June 2024

Acknowledgments

Finally, writing acknowledgments means almost finishing the chapter master thesis and finishing my study time. This amazing time was only enabled by the people around me.

First, I am very grateful to my supervisors Lindsey Nicholson, Jan-Thomas Fischer and Christoph Mitterer for your invaluable support, guidance and inputs. I never thought I would have so much fun with my Master's thesis. Thank you for making this thesis possible with your expertise and mentorship.

Special thanks go to the Austrian Forest Research Center (Bundesforschungszentrum für Wald, BFW), Department of Natural Hazards, unit Snow and Avalanches offering a working space. Without the support, the thesis would be far from finished. And a big thanks to the entire BFW team around Jan-Thomas Fischer and Michaela Teich for your inclusion, assistance with helping out in technical, programming or organisational questions and for camaraderie during breaks. Without your thesis, Chris Hesselbach, mine would not have existed. Thanks for forming the basis of my research, helping me out no matter when and giving me several inputs.

I am grateful to the team of the Avalanche Warning Service Tyrol, especially Christoph, for your insights into the world of snow and avalanches that fascinated me, and thanks for discussions and advices, which greatly enriched this thesis and presentations.

I am grateful to Stephan Harvey and Yves Bühler (WSL Institute for Snow and Avalanche Research SLF) for providing CAT and ATH maps and for your inputs and ideas for my research.

Thanks to my family and friends for support and encouragement during the entire study time. Thanks for enabling the real fun part besides work. Special thanks go to Nico for your patience and endurance with me.

Abstract

Avalanche terrain is classified according to the size of avalanches, depending on spatial distribution of potential release areas and corresponding runout. Maps classifying avalanche-prone terrain aid in planning activities. Examples generated by computational algorithms include the automated Avalanche Terrain Exposure Scale (autoATES) and the Classified Avalanche Terrain (CAT).

This study aims to compare autoATES and CAT classification qualitatively and quantitatively. Therefore, both classification methods are applied to two test regions: an area around Davos (Switzerland) and one in Sellrain (Austria).

While autoATES combines model chain results to classify terrain into four classes from simple to extreme, CAT explicitly delineates potential release areas, maximal runout, zones for potential remote triggering and very steep slopes. Despite differing outputs, both algorithms share similar intermediate steps, computing potential release areas and simulating avalanche runout using different tools.

Although intermediate results and end products depend on the choice of parameter, we can make the following general observations based on our comparison: ATES class 'simple' aligns well with areas not classified as avalanche prone in CAT maps, and ATES class 'extreme' aligns well with the CAT categories indicating slopes steeper than 50°. The distribution of CAT categories is widely spread within ATES classes 'challenging' and 'complex'. One reason for mismatches in classifications between the methods is the divergence in results from avalanche runout simulations used in the model chain modules for each classification method. For the parameterisations used to calculate the classification maps, autoATES' avalanche simulation tool Flow-Py simulations result in larger avalanches compared to RAMMS::EXTENDED used in the CAT workflow.

Furthermore, we make two modifications to the open-source autoATES model chain: Firstly, we implement the interaction of avalanches and forested areas resulting in a qualitative improvement of the ATES maps, particularly in areas where avalanches

interacted with forests previously. Secondly, we extend the open-source autoATES model chain to analyse the avalanche paths and corresponding thalwegs simulated with Flow-Py according to their size. For the autoATES workflow, we simulate avalanches using Flow-Py with a parameterisation aiming at size class 3. The majority of resulting paths are classified as avalanche size classes 2 and 3. However, some paths are classified as larger size classes. Moreover, we employ this Flow-Py extension quantifying the potential size of avalanches as a tool to compare the two test regions in terms of their destructive potential depending on the terrain. The Flow-Py simulation results include more paths and respective thalwegs with a higher destructive size in Sellrain than in Davos.

Avalanche terrain classification maps can be useful for terrain assessment and, consequently, for the reduction of risk. However, it is crucial to be aware of the utilized parameterisation, potential for inaccuracy, limitations and differences between the maps when using them.

Contents

Chapter 1

Motivation and Goals

Avalanches pose a danger for humans and infrastructure in mountainous winter terrain. The destructive potential of avalanches extends beyond damage to settlements, roads and other infrastructure to include fatal consequences posing a critical concern for residents and travelers. Between 1970 and 2015, 100 fatalities occurred on average each year due to avalanches. Each year, avalanches were responsible for 100 fatalities in the Alps in average between 1970 - 2015, with the majority occurring during outdoor activities (Techel et al. 2016).

The avalanche risk is defined as the probability of damage depending on avalanche danger and vulnerability combined with exposure of a certain element, such as persons, infrastructure and forest (Statham 2008). The avalanche risk for individuals traveling in avalanche-prone terrain is determined by a combination of factors including human behaviour, snowpack stability and terrain conditions (Jamieson and Geldsetzer 1996). To reduce avalanche risk, detailed trip planning is essential. Therefore, assisting tools are available. Avalanche warning services offer detailed information about current and predicted snowpack stability through their avalanche bulletins (Techel et al. 2018). To assess avalanche prone terrain, various maps are available. The most simple and widely accessible maps illustrate slope inclination, derived from digital elevation data. For example on the FATMAP (2023) website, the overlay including slope inclination is accessible worldwide. Several decision tools help to assess the avalanche risk by combining avalanche danger information with slope inclination, for example Munter's reduction method (Munter 1997), 'Stop or Go' (Larcher 1999) or 'Snow Card' (Engler 2001).

Slope inclination is not the sole contributing terrain factor for avalanche formation. Other factors, such as curvature, roughness and forests have a significant impact (Schweizer et al. 2003; Vontobel 2011). Additionally, the exposure to avalanches depends on overhead hazard. Including these parameters, several maps are created

to assess avalanche-prone terrain (Statham et al. 2006; Schmudlach and Köhler 2016b; Harvey et al. 2018; Larsen et al. 2020b).

Statham et al. (2006) and Statham and Campbell (2023) developed the Avalanche Terrain Exposure Scale (ATES) to classify terrain into four classes based on terrain characteristics, such as slope angle, curvature, forest density, avalanche frequency and start zone density. Larsen et al. (2020b) and Toft et al. (2023) developed a fully automated algorithm for generating ATES maps (autoATES). To clarify terminology, in this thesis 'autoATES' is used to refer to the automated workflow for generating 'ATES' maps. Harvey et al. (2018) developed Classified Avalanche Terrain (CAT) maps, which delineate potential release areas, remote triggering areas and maximal runout zones, along with Avalanche Terrain Hazard (ATH) maps that combine the potential for avalanches with their consequences. CAT and ATH maps are available in Switzerland. Schmudlach and Köhler (2016b) created different Avalanche Terrain Hazard Maps (ATHM) which classify the terrain into classes indicating the probability of avalanche triggering considering slope angle, size and shape. This map is available on the 'Skitourenguru' website, covering a large part of the Alps.

In comparison to site-specific avalanche hazard plans, that are also assessed by experts on site in respect to a specific annual avalanche occurrence (Sauermoser 2006), these maps provide a regional assessment focusing on avalanches of typical size for fatal accidents triggered by humans.

While CAT and ATH are exclusively available in Switzerland due to not open accessible tools required for the workflow (Harvey et al. 2018), ATES maps can be generated using open-source tools, enabling the classification in various regions (Larsen et al. 2020b; Toft et al. 2023). As these methods classify avalanche-prone terrain according to similar but not identical criteria, this thesis will describe several classifications. Furthermore, we apply autoATES and CAT in two Alpine test regions and compare both.

The main study aim of this thesis is to adopt the open-source autoATES workflow. This enables a comparison with other avalanche terrain classification approaches. Furthermore, the autoATES model chain allows for adaptations and extensions, enabling modifications and improvements to ATES maps, as well as a tool to classify simulated avalanche paths according to their size on a regional scale.

The initial research questions of this thesis are:

1. How do ATES and CAT maps compare in these two Alpine test regions?
2. How do the model chain modules of autoATES and CAT compare: potential release areas and avalanche runout?

Additional research questions motivated by this comparison and the possibility to adapt and extend the autoATES open-source model chain include:

3. Can we improve ATES maps with an adapted autoATES workflow including forest interaction?
4. How can we quantify and classify avalanche paths on a regional scale?
5. Do the two test regions exhibit different characteristics according to typical avalanche size through their given terrain characteristics?

This thesis is structured in the following chapters:

Chapter 2 represents the current state of resarch, fundamentally, of avalanche classification. Current avalanche terrain classification methods and their workflows are described, particularly autoATES and CAT.

Chapter 3 describes the data used for the application of autoATES and CAT as well as methods applied in the analyses of the several comparisons. Furthermore, implementations and extensions in the autoATES workflow are described.

Chapter 4 elaborates and discusses the results of the thesis answering the previously defined research questions.

Chapter 5 summarizes the key results and gives a short outlook for further research opportunities.

Chapter 2

Present State of Research

This section provides an overview of the current state of research on avalanche terrain classification methods. First, a short recap of various schemes to classify avalanches are provided (see sections 2.1 and 2.2). In the second part (section 2.3), existing methods for avalanche terrain classification based on automated workflows are described, particularly autoATES and CAT. Since the main model chain modules of these classification approaches are the delineation of Potential Release Areas and the simulation of avalanche runout, different methods for these processes are described in more detail in sections 2.4 and 2.5.

2.1 Classification of avalanches

Snow avalanches represent a major natural hazard in snow-covered mountains. Avalanches are mass flows containing snow moving down a descending slope due to gravity. Various models, described by Schweizer (1999), Schweizer et al. (2003), McClung and Schaerer (2006) and Rudolf-Miklau and Sauermoser (2011) explain mechanisms of avalanche formation. From a mechanical point of view, a prerequisite for avalanche formation is an exceeding stress within the snowpack compared to its strength. The stress increases due to loading on the snowpack such as artifical loading by humans or explosives and spatially even loading, for example by precipitation or wind drifted snow. The strength of the snowpack can decrease due to melting within the snowpack (Schweizer 1999; Schweizer et al. 2003).

Various schemes classify avalanches. UNESCO (1981) provides a morphological classification and a classification of avalanche conditions. Furthermore, numerous schmemes for classification exist (EAWS 2023; CAA 2016; Bühler et al. 2019).

2.1.1 Classification of avalanche conditions

Stress and strength of the snowpack and thus the avalanche formation depend on the complex interaction of terrain and meteorological conditions (Schweizer et al. 2003). Meteorological factors directly impact the snowpack, leading to temporal and spatial variations, while terrain conditions typically remain constant over longer time periods. UNESCO (1981) classifies avalanches according to terrain conditions, weather conditions, snowpack and triggering mechanisms. Schweizer et al. (2003) summarizes these parameters to the contributing factors of an avalanche formation. These are briefly outlined in this section. Further details can be found in the mentioned references.

Snowpack and meteorological conditions

Prerequisites for avalanche formation regarding the snowpack are the presence of a weak layer within the snowpack and an overlying cohesive slab-layer (Schweizer et al. 2003). The snowpack stratigraphy and its spatial distribution are directly influenced by previous and current meteorological conditions (Schweizer et al. 2003). Precipitation, wind and air temperature and humidity modify the snowpack and influence its stability. For example, a high rate of new snow deposition can rapidly increase the stress on the snowpack, often resulting in very large avalanches. Additionally in lee slopes, wind drifted snow is deposited leading to a higher loading and formation of a well bonded slab, which favours avalanche formation (Gauer 1999).

Terrain

Avalanche formation is based on gravitational forces requiring slope inclination. Numerous studies show that the gravitational force is sufficient to trigger avalanches on slopes steeper than approximately 30° (Schweizer et al. 2015). Schweizer and Lütschg (2001) analysed the slope angle in the starting zones of 617 human-triggered avalanches in Switzerland. The median of the slope angle was 38°, with a range between 27° and 51°. Particularly, large avalanches or wet-snow avalanches may also release in slopes with lower angles. However, the range where avalanches release differ slightly in various studies. Veitinger et al. (2016) suggest that avalanches can occur on slopes with slope angles ranging from 28° to 60°, while Harvey et al. (2018) considers slope angles between 30° and 50° for potential avalanche release areas.

The curvature of the terrain influences the avalanche probability, with concave terrain typically being more favourable for avalanches (Maggioni and Gruber 2003; Schweizer et al. 2003; Vontobel 2011). Additionally, the terrain roughness can hinder the formation of a continuous weak layer, especially when the snowpack is shallow. A high snow height smooths out the terrain and thus, decrease the influence of the roughness on avalanche formation (Schweizer et al. 2003).

In dense forests, the probability of an avalanche formation decreases (Schweizer et al. 2003). Tree stems interrupt the snow cover and therefore potential weak layers. Additionally, canopy cover modifies the snowpack regarding snow accumulation and radiation. Reduced snow accumulation and less radiative cooling in forested areas lead to lower stress on the snowpack due to less loading and to a reduced formation of surface hoar or facets that can form weak layers (Schweizer et al. 2003; McClung and Schaerer 2006). Furthermore, forests can decelerate avalanches and limit their runout distance (Teich et al. 2012). However, even very large avalanches can destroy forests without reduction in velocity (Margreth 2004).

2.1.2 Classification of avalanche morphology

An avalanche initiate in a zone of origin, also called release area. As the snow mass moves downslope, it accelerates and breaks into granular blocks until it reaches an approximately constant velocity in the zone of transition. In flat terrain, the movement decelerates in the deposition or runout zone (McClung and Schaerer 2006; Schweizer et al. 2015). These three main zones of avalanches, such as release area, transition zone and deposition zone are explained in this section (UNESCO 1981).

Zone of origin

In the zone of origin, the avalanche starts or rather releases. There are two main types of avalanche release characteristics based on the shape of the release area: loose snow avalanches (Figure 2.1a) and slab avalanches (Figure 2.1b).

A loose snow avalanche starts in a single point, a small volume of incohesive snow moves downslope and entrains further snow as it spreads. These avalanches typically have a triangular shape. Loose snow avalanches are usually small and harmless (Schweizer et al. 2015).

A slab avalanche is initiated by a failure and a crack propagation within a weak layer. This failure causes a bonded slab above the weak layer to move downslope if the slope is steep enough. The fracture line is usually sharp edged (Schweizer et al.

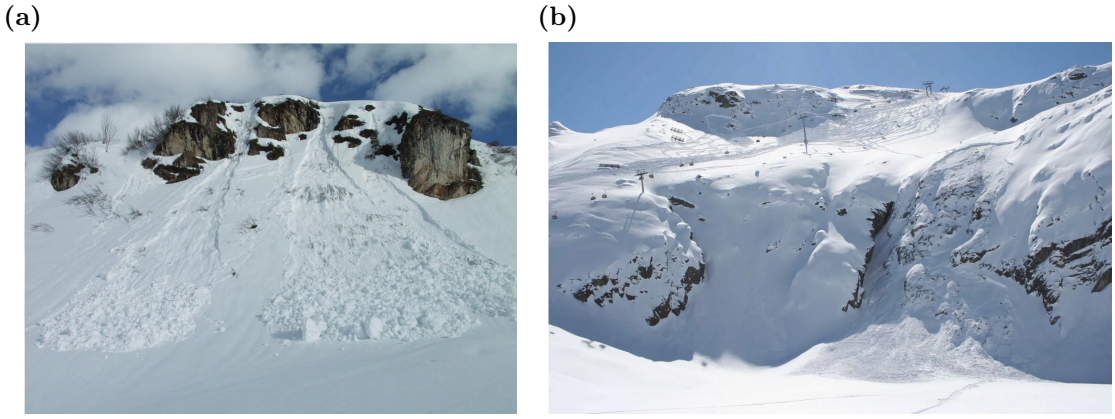

Figure 2.1: Examples of the two types of avalanche release mechanisms: (a) loose snow avalanche and (b) slab avalanche. Pictures from EAWS (2023).

2015).

Both, loose snow and slab avalanches can occur as dry and wet avalanches. Detailed information about the release mechanisms is reviewed in Schweizer et al. (2003, 2015) and specifically about wet snow avalanches in Mitterer and Schweizer (2013).

Zone of transition

The zone of transition describes the path of the avalanche flow influenced by the terrain surrounding the avalanche path and the properties of the moving snow. The flow can be categorized into two schemes: dense flow contains dense snow mass and powder flow contains a suspension of snow and air with a low density. Most avalanches consist of a dense snow part and a powder part, therefore they can be described by a combination of both schemes (Schweizer et al. 2015). Regarding the avalanche path, dense snow avalanches follow the terrain conditions, while powder snow avalanches are less constrained by terrain features and can flow over obstacles (Sauermoser et al. 2014).

Zone of deposition

In the zone of deposition or runout zone, the avalanche debris is deposited. It is marked from the point the avalanche begins decelerating to where it finally stops. Typically, the avalanche decelerates when friction energy exceeds the kinetic energy (Schweizer et al. 2015). Generally, large and dry avalanches start to decelerate in the point, where the slope angle of the terrain is 10° (Bakkehoi et al. 1983). However, this deceleration point may vary for smaller and larger avalanches. Avalanche size classifications are described in section 2.2.

2.2 Classification of avalanche size

Various systems are used to classify the avalanche size. European Avalanche Warning Services (EAWS) classify the avalanche size into five classes depending on their potential destructiveness, runout length and volume. The classes include small, medium, large, very large and extremely large avalanches (see Table 2.1) (EAWS 2023).

Table 2.1: Avalanche size classification method after EAWS (2023).

Size	Destructive potential	Length	Volume [m^3]
E1 - small	Unlikely to bury a person.	10 - 30 m	100
E2 - medium	May bury, injure or kill a person.	50 - 200 m	1 000
E3 - large	May bury and destroy cars, damage trucks, destroy small buildings and break a few trees.	several 100 m	10 000
E4 - very large	May bury and destroy trucks and trains, may destroy fairly large buildings and small areas of forest.	1 - 2 km	100 000
E5 - extremely large	May devastate the landscape and has catastrophic destructive potential.	$>$ 2 km	$>$ 100 000

The avalanche size classification by the Canadian Avalanche Association (CAA) presents a similar classification scheme (Table 2.2). The classification dependent on destructive potential involves describing destructive potential and considering values of impact pressure, additionally. Furthermore, CAA employs typical mass for size classification, while EAWS uses volume (CAA 2016).

Bühler et al. (2019) identify the size of mapped avalanches based on their affected area using satellite imagery (Table 2.3).

Table 2.2: Avalanche size classification method after CAA (2016).

Size	Destructive potential	Typical mass [t]	Typical path length [m]	Typical impact pressure [kPa]
C1	Relatively harmless to people.	< 10	10	1
C2	Could bury, injure, or kill a person.	100	100	10
C3	Could bury and destroy a car, damage a truck, destroy a wood-frame house or break a few trees	1 000	1 000	100
C4	Could destroy a railway car, large truck, several buildings or a forest area of approximately 4 hectares.	10 000	2 000	500
C5	Largest snow avalanche known. Could destroy a village or a forest area of approximately 40 hectares.	100 000	3 000	1 000

Table 2.3: Avalanche size classification method after Bühler et al. (2019).

Size	Affected area
B1 - Small	≤ 500 m^2
B2 - Medium	501 - 10 000 m^2
B3 - Large	10 001 - 80 000 m^2
B4 - Very large	80 001 - 500 000 m^2
B5 - Extremely large	> 500 000 m^2

2.3 Automated classification of avalanche terrain

Automatic algorithms for classifying avalanche terrain exhibit several advantages: They are more efficient, compared to manual classification methods. Algorithms enable classification of large areas and regions with difficult access using digital terrain data. Furthermore, they provide consistent results that are reproducible.

There are two main types of avalanche classification maps:
1) avalanche hazard zoning plans used for settlements, roads and generally infras-

tructure planing (CAA 2002; Sauermoser 2006) and
2) avalanche hazard classification maps designed for individuals traveling in avalanche-prone terrain.
These types differ primarily in the avalanche size taken into account. This thesis focuses on classification methods intended as planning tools for backcountry trips. These methods consider large avalanches (size 3 after the avalanche size classification by EAWS (2023)), which are typically triggered by skiers (Harvey et al. 2018; Larsen et al. 2020b).

Avalanche terrain classification can be categorized as static or dynamic. Static classification is primarily terrain-based and does not take snowpack stability into account. Dynamic classification methods combine terrain features with snowpack stability, for example including information of avalanche bulletins (Statham et al. 2006; Schmudlach and Köhler 2016b; Harvey et al. 2018).

The following sections describe methods for avalanche terrain classification, with a particular focus on ATES and the open-source workflow, which allows for further adaptation and extensions, while modules of the CAT model chain are not freely available.

2.3.1 Avalanche Terrain Exposure Scale

The Avalanche Terrain Exposure Scale (ATES) is a static avalanche terrain classification method developed in Parks Canada to offer (avalanche) terrain information of backcountry trips to the public, especially backcountry recreationists. The first published ATES version (v.1/04) classifies avalanche terrain into three classes: 'simple, 'challenging', 'complex'. The classification depends on different terrain parameters such as slope angle, forestation, curvature, start zone density and number of route options. The classification contains two models, the technical model describes the terrain parameters resulting in the classes (see the evolved version in Table 2.4). The public ATES model describes the classes in a simplified manner for the public (see the evolved version in Table 2.5). (Statham et al. 2006; Statham and Campbell 2023)

ATES is used for

1. rating tours: Every point in a route is classified, the overall class of the tour is usually the highest class of all points.

2. zoning terrain (Campbell and Gould 2013, 2014): In a larger area, the terrain is classified resulting in a static map.

Table 2.4: ATES techical model v.2 from Statham and Campbell (2023).

	Class 1 Simple	**Class 2 Challenging**	**Class 3 Complex**	**Class 4 Extreme**
Exposure	Minimal exposure (low frequency runout zones or short slopes)	Intermittent exposure (single path or paths with separation)	Frequent exposure (to starting zones, tracks or multiple overlapping paths)	Sustained exposure (within or below starting zones)
Slope angle and Forestation	$< 20°$ or steeper slopes in dense forest with openings for runout zones or short slopes	$< 30°$ open or gladed terrain with some open slopes or glades $> 35°$	$< 35°$ with large proportion of open slopes $> 35°$ and some isolated glades or tree bands	averaging $> 35°$ with a large proportion of slopes $> 45°$ and few or no trees
Slope shape	Straightforward undulating terrain	Mostly planar with isolated convex or unsupported slopes	Convoluted open slopes with intricate and varied terrain shapes	Intricate, often cliffy terrain with couloirs, spines and/or overhung by cornices
Terrain traps	Occasional creek beds, tree wells or drop-offs	Single slopes above gullies or risk of impact into trees or rocks	Multiple slopes above gullies and/or risk of impact into trees, rocks or crevasses	Steep faces with cliffs, cornices, crevasses and/or risk of impact into trees or rocks
Avalanche frequency: magnitude	1:100 - 1:30 for $\geq$ Size 2	1:1 for $<$ Size 2 1:30 - 1:3 for $\geq$ Size 2	1:1 for $<$ Size 3 1:1 for $\geq$ Size 3	10:1 for $\leq$ Size 2 $>$ 1:1 for $>$ Size 2
PRA size and density	Runout zones only except for isolated, small starting zones with $<$ Size 2 potential	Isolated starting zones with $\leq$ Size 3 potential or several start zones with $\leq$ Size 2 potential	Multiple starting zones capable of producing avalanches of all sizes	Many very large starting zones capable of producing avalanches of all sizes
Runout zone characteristics	Clear boundaries, gentle transitions, smooth runouts, no connection to starting zones above	Abrupt transitions, confined runouts, long connection to starting zones above	Multiple converging paths, confined runouts, connected to starting zones above	Steep fans, confined gullies, cliffs, crevasses, starting zones directly overhead
Route options	Numerous, terrain allows multiple choices; route often obvious	A selection of choices of varying exposure; options exist to avoid avalanche paths	Limited options to reduce exposure; avoidance not possible	No options to reduce exposure

Table 2.5: ATES public communication model for backcountry travel v.2 from Statham and Campbell (2023).

ATES class	Description
Class 0 (non-avalanche)	No known exposure to avalanches. Very low-angle or densley forested slopes located well away from avalanche paths, or designated trails/routes with no exposure to avalanches.
Class 1 (simple)	Exposure to low-angle or primarily forested terrain. Some forest openings may involve the runout zones of infrequent avalanches and terrain traps may exist. Many options to reduce or eliminate exposure.
Class 2 (challenging)	Exposure to well-defined avalanche paths, starting zones, terrain traps or overhead hazard. With careful route finding, some options will exist to reduce or eliminate exposure.
Class 3 (complex)	Exposure to multiple overlapping avalanche paths or large expanses of steep, open terrain. Frequent exposure to overhead hazard. Many avalanche starting zones and terrain traps with minimal options to reduce exposure.
Class 4 (extreme)	Exposure to very steep faces with cliffs, spines, couloirs, crevasses or sustained overhead hazard. No options to reduce exposure; even small avalanches can be fatal.

ATES was applied in various regions worldwide (Gavaldà et al. 2013; Martí et al. 2013; Gould et al. 2014; Pielmeier et al. 2014; Schmudlach and Köhler 2016a; Moner et al. 2018). In some studies, Geographical Information Systems (GIS) were used to develop (semi-) automated algorithms for zoning ATES maps (Campbell and Marshall 2010; Delparte et al. 2013; Schmudlach and Köhler 2016b; Nåfält 2016; Schmudlach et al. 2018). When zoning larger areas, Campbell et al. (2012) criticized that the parameters of the ATES v.1/04 model are not quantitative, making automated classification challenging. Campbell and Gould (2013, 2014) refined the original technical ATES v.1/04 model enabling the representation of parameters in GIS with quantitative thresholds. With this adapted Zoning model ATES maps can be computed with GIS.

Larsen et al. (2018) and Larsen et al. (2020a) developed a model for classifying terrain automatically into ATES classes, based on the Zoning ATES model by Campbell and Gould (2014). Using this workflow with only a digital elevation model as input, they produced nationwide ATES maps for Norway. Schumacher et al. (2022) improved the algorithm by including forest density data.

Statham and Campbell (2023) evolved the public and technical model into ATES v.2 (Tables 2.5 and 2.4) containing new ATES classes 0 (non avalanche terrain; optional) and 4 (extreme terrain). Additionally, the technical model is adapted to ATES Zoning model enabling automated ATES mapping.

Toft et al. (2023) updated the automated workflow developed by Larsen et al. (2020b) and Schumacher et al. (2022) for the ATES model v.2 (Statham and Campbell 2023), utilizing only open-source programs written in programming language Python (Van Rossum et al. 1995). They do not consider ATES class 0, instead, areas, that would be assigned to class 0, are included in class 1 (Sykes et al. 2024). Hesselbach (2023) adapted this algorithm for application in an Austrian test region located in Tyrol.

The autoATES-algorithm v.2 contains the following computation steps:

1. Potential Release Area (PRA) algorithm
   PRAs are calculated using the methodology developed by Veitinger et al. (2016) and Sharp (2018).

2. Avalanche mobility tool
   The corresponding runout length of an avalanche is simulated using Flow-Py (D'Amboise et al. 2022b).

3. autoATES classifier
   The PRA and avalanche mobility results, along with various terrain indicator, are then classified and mapped (Toft et al. 2023).

This workflow yields the four ATES classes (Toft et al. 2023; Hesselbach 2023).

Table 2.6 list references that use ATES including their used ATES version, application type and region as well as their results.

Table 2.6: Selection of studies applying ATES with a summary of the used ATES version, the applied region and main results.

Reference	**ATES version**	**Application**	**Results**
Statham et al. (2006)	ATES v.1/04 (manually)	tours in Canadian National Parks	ATES as a planning tool

Continued on next page

Table 2.6: Selection of studies applying ATES with a summary of the used ATES version, the applied region and main results.

Reference	ATES version	Application	Results
Campbell and Marshall (2010)	v.1/04 (local expertise)	zones in British Columbia (BC) parks	ATES maps in slope-to mountain scale, verified by field and aerial survey
Campbell et al. (2012), Campbell and Gould (2013), Campbell and Gould (2014)	Zoning model	zones in BC parks	refined ATES model for automated GIS model.
Gavaldà et al. (2013)	v.1/04 (manually)	tours and zones in Val d'Aran	information panels with ATES maps
Gould et al. (2014)	Zoning model	industrial projects in Canada	ATES as addition to atlas and locator mapping for terrain and hazard guidance
Pielmeier et al. (2014)	v.1/04	tours in Swiss Jura	ATES is suitable in Swiss Jura.
Nåfält (2016)	v.1/04 (modified for GIS)	zones in Nuolja (Sweden)	Including altitude as parameter does not improve ATES; model not suited for GIS; model subjective
Schmudlach and Köhler (2016b)	modified ATES model	area in Switzerland	new ATES criteria catalog resulting in ATES/ATHM rating between 0 and 100%.
Thumlert and Haegeli (2018)	mapping algorithm from movement of ski guides	zones in BC	avalanche condition-dependent maps
Bacardit et al. (2018)	v.1/04 & Zoning model	zones in Val d'Aran	Zoning model is more practical than original technical model.
Moner et al. (2018)	Zoning model	zones in Val d'Aran	Most accidents occurred in complex and challenging terrain; Avalanche size increased with complexity of terrain.
Larsen et al. (2020b), Larsen et al. (2020a)	autoATES v1.0	areas and routes in Norway	fully automated algorithm to create ATES maps
Schumacher et al. (2022)	autoATES v1.0	areas and routes in Norway	improved ATES maps including forest attributes

Continued on next page

Table 2.6: Selection of studies applying ATES with a summary of the used ATES version, the applied region and main results.

Reference	ATES version	Application	Results
Statham and Campbell (2023)	ATES V.2	areas, zones corridors, routes	combined ATES v.1/04 and Zoning Model; 5 ATES classes
Toft et al. (2023)	autoATES v2.0	areas in Glacier and Banff Nationalpark	improved algorithm including forest density compared to autoATES v1.0.
Hesselbach (2023), Huber et al. (2023)	autoATES v2.0	area in Austria	autoATES map with adapted parameter setup
Sykes et al. (2024)	autoATES v2.0	areas in Canada	autoATES maps align with ATES benchmark maps in 74.5% and 84.4%.

2.3.2 Classified Avalanche Terrain and Avalanche Terrain Hazard

Harvey et al. (2018) generated Classified Avalanche Terrain (CAT) and Avalanche Terrain Hazard (ATH) maps with a fully automated algorithm using GIS. CAT maps delineate potential release areas, areas with potential of remote triggering and runout zones of avalanches of size 3 (EAWS 2023). ATH maps contain a hazard indicator, expressed in continuous values indicating the potential of an avalanche release combined with its consequences when being caught.

Requiring a Digital Terrain Model (DTM) and a binary forest layer as input, the CAT map is computed using the following tools:

1. Potential release area (PRA) algorithm

2. RAMMS::EXTENDED
   for simulating the maximal runout of an avalanche of size 3

3. tool to delineate the potential of remote triggering.

Harvey et al. (2018) created nationwide CAT and ATH maps for Switzerland.

2.3.3 Other classification methods

Avaluator

The Avaluator (Haegeli et al. 2006) assesses avalanche risk by combining ATES maps with the current avalanche danger level. It serves as a dynamic trip planner providing decision guidelines.

Avalanche Terrain Hazard Map (ATHM)

Schmudlach and Köhler (2016a,b) offer an avalanche classification map (ATHM) and dynamic rating of backcountry tours through the platform 'Skitourenguru'. They developed a fully automated algorithm to compute maps rating the avalanche-prone terrain in continuous values based on a DEM and land cover data. The algorithm uses modified ATES criteria, aimed at computing the maps from a skiers' perspective. For every point in the map, the algorithm defines the environment, which is relevant according to avalanche exposure in this point. Further, this environment is assessed by the distribution of slope angles. Depending on this geomorphologic property in every point, a rating value between 0 and 100% is computed. Unlike to the previous described classification methods autoATES and CAT, this approach does not include the simulation of avalanches (Schmudlach and Köhler 2016b).

Furthermore, Schmudlach and Köhler (2016a) and Schmudlach et al. (2018) dynamically evaluate the risk of specific backcountry routes by combining the terrain assessment with the current avalanche danger level obtained from avalanche warning services.

2.4 Delineation of Potential Release Areas

Detecting the location of PRAs is an important step for deriving areas exposed to avalanches. Simulation tools rely on these PRAs to compute avalanche movement (Christen et al. 2010; D'Amboise et al. 2022b).

Vontobel (2011) analysed typical terrain characteristics of avalanche starting zones, the basis for automated algorithms to delineate PRAs (Maggioni and Gruber 2003; Veitinger et al. 2016; Bühler et al. 2018). As described in section 2.1.1, the range of typical slope angles of PRAs differ slightly in numerous studies (Schweizer et al. 2015; Veitinger et al. 2016; Harvey et al. 2018). After Schweizer and Lütschg (2001), avalanches typically release in terrain with slope angles between 27°

and 51°. In slopes below 27° the gravitational force is too weak, while terrain exceeding 51° is usually too steep for snow deposition, preventing the slab formation.

A main difference between the following algorithms is the output format. The algorithm of Veitinger et al. (2016) and the algorithm within the CAT workflow produce raster files, where each raster cell is assigned to a continuous value between 0 and 1, indicating the likelihood of an avalanche release. The model output of Bühler et al. (2018) is in vector format, with PRAs delineated as polygons.

2.4.1 Algorithm of Veitinger et al. (2016) and Sharp (2018)

The algorithm, originally developed in Programming language R by Veitinger et al. (2016) and Sharp (2018), was adapted to Python by Toft (2022). Toft et al. (2023) and Hesselbach (2023) used this Python version to compute PRAs.

The open-source algorithm developed by Veitinger et al. (2016) to delineate PRAs depends on slope, a wind shelter index and roughness, derived from a DTM. With an optional forest mask, PRAs are eliminated in forested areas. They use a fuzzy logic approach (Zadeh 1965) that assigns each element (in this case a raster cell) a degree of membership. This approach captures the complex and uncertain natural data and processes of avalanche release better than existing methods that assign elements to discrete classes, such as PRA and no PRA. To mitigate abrupt changes at the corners, this algorithm employs Cauchy membership functions to weigh the importance of the terrain parameters (Jang et al. 1997):

$$\mu(x) = \frac{1}{1 + (\frac{x-c}{a})^{2b}}, \tag{2.1}$$

with Cauchy membership value $\mu(x)$, variable x, and weighting coefficients a, b, c determing the position and shape of the function.

In this algorithm, the slope angle is accounted for a range between 28° and 60°. Using Cauchy membership functions, Veitinger et al. (2016) and Hesselbach (2023) show that slopes between 35° and 45° have the maximum of Cauchy membership value and thus the greatest influence on PRAs.

The wind shelter index, adopted from Plattner et al. (2004) and Winstral et al. (2002), considers spatial variations of snow deposition resulting from terrain curvature and wind drift (Gauer 1999; Maggioni and Gruber 2003; Lehning et al. 2008; Vontobel 2011). The Cauchy membership function assigns higher values and greater importance to PRAs on lee slopes, and lower values on windward slopes

(Veitinger et al. 2016; Sharp et al. 2018). Since the mean wind direction varies spatially at regional scale, Larsen et al. (2020b) and Hesselbach (2023) neglected a mean wind direction.

The roughness parameter takes into account the roughness morphology of the summer DEM, coupled with a smoothing factor to consider the terrain smoothing due to snow accumulation. Considering roughness, Veitinger et al. (2016) adopted the ruggedness measure proposed by Sappington et al. (2007) in the algorithm. Rough terrain is assigned to a low membership value, smooth terrain to high values (Veitinger et al. 2016; Hesselbach 2023). However, Larsen et al. (2020a) and Schumacher et al. (2022) neglected the roughness parameter arguing that the DEM used with 10 m resolution indirectly smooths the terrain. Hesselbach (2023) used a binary roughness parameter to compute PRAs.

Sharp et al. (2018) enhanced the PRA algorithm of Veitinger et al. (2016) by integrating a forest density variable into the fuzzy logic approach. This variable encompasses metrics such as basal area, stem density or canopy cover. Areas with a dens forest cover are assigned to low Cauchy membership values, and a lower significance for avalanche release, while not forested or sparse forested areas have a higher membership value and are more important for PRAs (Sharp et al. 2018; Hesselbach 2023).

The algorithm produces a raster file containing continuous values between 0 and 1, indicating the potential of an avalanche release. Hesselbach (2023) applies a threshold of 0.3 to convert the continuous output into a binary PRA raster file. Raster cells below 0.3 are not assigned as PRAs, cells with values equal or greater than 0.3 are designated as PRAs.

2.4.2 Algorithm for CAT

The delineation of PRAs in the CAT workflow is based on observed release areas, which are analysed for terrain features such as slope inclination, curvature and fold. A 3D Kernel density estimate is calculated including these parameters. This resulting density function enables the derivation of density values for release areas in each raster cell. It is worth noting that only release areas with slope angles between 30° and 50° are considered (Harvey et al. 2018).

2.4.3 Algorithm of Bühler et al. (2018)

Bühler et al. (2018) optimized the method developed by Bühler et al. (2013) for delineating PRAs using object-based image analysis. In a first step, PRAs are identified based on slope angle, curvature and ruggedness, derived from a DTM. The resulting PRAs are then segmented using a flow direction algorithm implemented in ArcGIS (ESRI 2018). PRAs within forested areas identified from a binary forest layer are excluded. For further refining, the PRAs are segmented dependent on variations in aspect, slope and fold. Unlike the methods for delineating PRAs described previously, this algorithm produces PRAs as polygons.

2.5 Avalanche mobility simulations

Avalanche simulation models encompass two main categories: process-based physically motivated and data-based empirically motivated approaches. Process-based models describe the motion using equations for physical processes, while data-based or conceptual approaches rely on conceptual and empirical relations. Compared to process-based models, data-based models typically require fewer input data and need lower computational costs, making them more suitable for large-scale applications. However, since they do not directly represent physical variables and processes, the interpretation of results may require a more nuanced understanding. (D'Amboise et al. 2022b)

This section describes the conceptual simulation tool Flow-Py, which is a part of the autoATES workflow, and the physically-based tool RAMMS::EXTENDED serving avalanche runout data for the CAT workflow.

2.5.1 Flow-Py

Flow-Py (com4FlowPy), developed by D'Amboise et al. (2022b), is a computational module within the Avaframe framework providing open-source avalanche simulation tools (Neuhauser et al. 2021; Oesterle et al. 2024). Flow-Py calculates runout and intensity of a gravitational mass flow (GMF), such as avalanches or rockfalls, based on a conceptual approach. Given a starting zone, it simulates the movement of a GMF according to routing and stopping routines dependent on a three-dimensional terrain. The computation is based on geometrical relations initially proposed by Heim (1932). In this thesis, Flow-Py is used to simulate snow avalanches. The direction of the movement (routing) depends on the local terrain and previous flow. The computation of runout length (stopping) is based on the runout angle (α-) model using geometric concepts (Heim 1932; Lied and Bakkehøi 1980; Bakkehoi

et al. 1983; D'Amboise et al. 2022b).

Figure 2.2 demonstrates the geometric relationships in a two-dimensional terrain. The gravitational mass flow starts at horizontally projected distance s_0 at an altitude $z(s_0)$, the movement stops at s_α. The runout angle α is defined as the angle between the horizontal and the line connecting the highest point of the starting zone with the lowest point of deposition. Dependent on a fixed α-angle the runout of the simulated avalanche is determined (main stopping criterion). Lied and Bakkehøi (1980) defined α statistically using the four topographic parameters: profile curvature and average slope of the avalanche path, vertical drop height and slope angle of the starting zone.

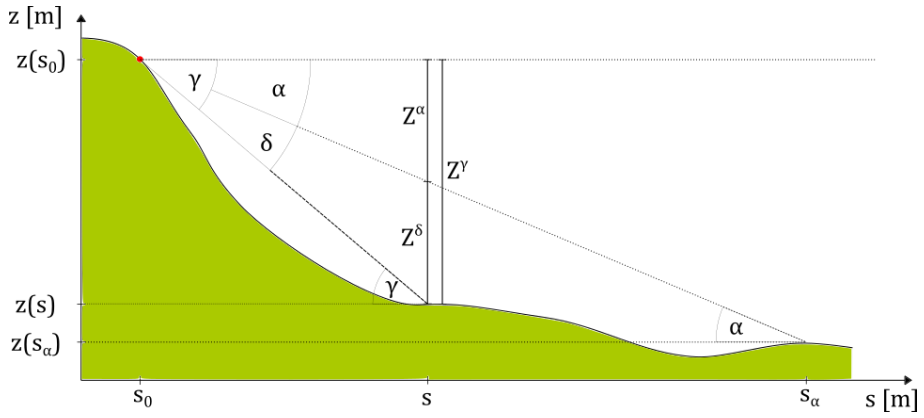

Figure 2.2: Two-dimensional representation of a gravitational mass flow path from release $(s_0, z(s_0)$ to deposition $(s_\alpha, z(s_\alpha))$ point with the corresponding runout angle α. s represents the horizontally projected travel length, z the altitude. At the point $(s, (z(s))$ with local travel angle γ the intensity parameters Z^α and Z^δ can be derived. Figure from D'Amboise et al. (2022b).

Flow-Py, written in Python3 language (Van Rossum et al. 1995), adopts object-oriented programming structured in three levels: cell, path and raster level. At the cell level iterative routing and stopping take place. The path level combines all cells, which belong to one release cell, while the raster level aggregates all paths.

At the cell level, routing depends on local terrain and the persistence of the prior flow, relying on the gravitational process path model after Wichmann (2017). Flow-Py simulates mass flow in mountainous terrain including downslopes, flat and uphill terrain. Stopping criteria determine the runout and intensity of the flow based on geometric relations derived from the runout angle concept (Heim 1932; Lied and Bakkehøi 1980; Körner 1980). The flow stops when the α-angle is reached. Additionally, thresholds limit lateral spreading considering

the concept that a mass flow requires a minimum mass for continuing the movement.

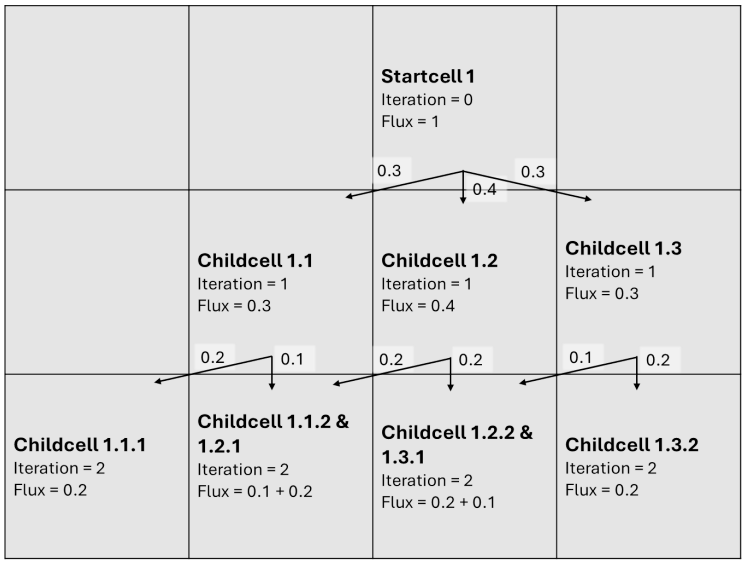

Figure 2.3: Schematic illustration of the routing flux distribution in Flow-Py. The startcell divides its flux to surrounding childcells along the arrows dependent on the terrain. The passed flux is marked at the arrows, respectively. In a futher iteration step, these childcells divide its flux to surrounding cells.

For every raster cell assigned to a release cell Flow-Py calculates a GMF path. Each release cell starts with a routing flux of 1. During the propagation the cells transfer routing flux to adjacent cells, where the movement continues to. This routing flux can be interpreted as mass. This distribution of flux to childcells is illustrated schematically in Figure 2.3.

The flow intensity (kinetic energy) can be derived by the energy height using the runout angle (α) concept (Heim 1932; Lied and Bakkehøi 1980; Körner 1980). The runout is determined by the α angle, leading in a total vertical drop height $z(s_0) - z(s_\alpha)$ and horizontally projected travel length $s = s_\alpha - s_0$. At each point s along the path, a travel angle γ with a corresponding vertical drop height z^γ can be derived:

$$z^\gamma = z(s_0) - z(s). \tag{2.2}$$

$$\gamma = \tan^{-1}(\frac{z^\gamma}{s}). \tag{2.3}$$

z^γ can be divided into z^δ, the kinetic energy height, indicating the intensity of the flow, and z^α, the frictional dissipation energy:

$$z^\gamma = z^\alpha + z^\delta \tag{2.4}$$

z^{α} can be calculated as:

$$z^{\alpha} = \tan(\alpha)\,(s - s_0) \tag{2.5}$$

So the intensity of the flow at point s is:

$$z^{\delta} = z^{\gamma} - z^{\alpha} = (z(s_0) - z(s)) - \tan(\alpha)(s - s_0) \tag{2.6}$$

z^{δ} is the kinetic energy height, from which process intensity and velocity are derived (Heim 1932; Körner 1980; D'Amboise et al. 2022b).

Flow-Py requires two main input data: a DTM and a raster file delineating release areas, indicated by values larger than zero. Both datasets must have the same extent and raster resolution. Additionally, the following parameter can be selected that determine the flow:

1. alpha (angle): is a stopping criterion for the runout. The runout extends until the alpha line intersects with the terrain (see Figure 2.2).

2. exp: determines the lateral spreading in the terrain-based routing process. A larger exponent exp concentrates the flow more towards the steepest descent, while a smaller exponent results in a wider spread flow.

3. R_{stop}: is a stopping criterion. The flow stops, when the routing flux is smaller than the critical routing flux threshold R_{stop}.

4. Z^{δ}_{lim}: maximum value of Z^{δ}, which limits the intensity or kinetic energy of the flow.

Outputs of Flow-Py are raster layers with the same extent and resolution as the input files. Variables describing the GMF are:

- z^{δ} is associated with the intensity and kinetic energy at every cell.
- The local routing flux corresponds to the flow concentration or a theoretical mass.
- Cell count contains the number of paths that hit a raster cell.
- The local travel angle is a measure of exposure.

From z^{δ} the impact pressure can be derived by (Körner 1980; Rudolf-Miklau and Sauermoser 2011)

$$impact\,pressure = \rho v^2 \tag{2.7}$$

with velocity v:

$$v = \sqrt{2z^{\delta}g} \tag{2.8}$$

the snow density ρ in the flow is assumed as 200 kg m^{-3} (McClung and Schaerer 2006), g indicates the gravitational acceleration.

2.5.2 Rapid Mass Movement Simulation (RAMMS)

To represent the maximal runout in the CAT map, avalanches are simulated using RAMMS::EXTENDED (Bartelt et al. 2012, 2016). RAMMS is a process-based avalanche simulation model that computes avalanche dynamics based on the terrain for predefined release areas (Christen et al. 2010).

RAMMS is based on the Voellmy-Salm model (Salm 1993) and a flow model that considers random kinetic energy, determined by the kinetic energy and mass of snow granules in the flow.

Shortly summarized, the Voellmy-Salm model employs a coordinate system (with x, y, z coordinates) along the surface topography, with z-axis perpendicular to the profile. Equations governing the Voellmy-Salm model include those for mass balance, accounting for snow entrainment and deposition as well as momentum balance. The effective acceleration of an avalanche is determined for the x- and y-component by:

$$g_x H - S_{fric,x} \tag{2.9}$$

and

$$g_y H - S_{fric,y} \tag{2.10}$$

with respective components of gravitational acceleration $g_{x,y}$, snow height H and components of friction $S_{fric;x,y}$. The friction parameter is divided into a dry-Coulomb term independent of velocity and a velocity dependent 'turbulent' term. The friction terms are described in more detail in section 4.3.2.

The random kinetic energy model adds to the depth-averaged motion fluctuations of granulars within the avalanche flow, which vary in smaller time scales compared to the previously described depth-averaged flow. The total velocity is then the sum of velocity of depth-averaged flow and the fluctuations. Thus, internal motions within the avalanche are considered resulting in more reasonable velocity outputs. These mathematical equations are numerically solved using primarily numerical methods for a shallow water model (LeVeque 2002).

According to Christen et al. (2010), input parameters for RAMMS include

1. DEM
2. release zone area (in vector format) and fracture depth
3. friction parameters

Regarding the CAT workflow, the input PRAs are computed using the object-based algorithm developed by Bühler et al. (2018). The average fracture depth is set to 50 cm to simulate avalanches of size 3 (Harvey et al. 2018).

2.6 Additional tools for autoATES and CAT

In addition to the PRA algorithms and avalanche simulation tools, the autoATES classifier combines intermediate results to ATES classes in the autoATES workflow. In the CAT workflow potential remote triggering zones are calculated.

2.6.1 autoATES classifier

The classifier of the autoATES v1.0 (Larsen et al. 2020b; Schumacher et al. 2022) is extended by Toft et al. (2023) for use of the autoATES v2.0 workflow, which is employed in this thesis. The classifier classifies the terrain into four classes: 'simple', 'challenging', 'complex' and 'extreme' depending on slope angle, PRA, avalanche runout and a forest density. Optionally, an overhead exposure can be computed using cell count and z delta. Hesselbach (2023) included a glacier layer in the classification process.

Input data required for the classifier include:

1. DEM: for deriving slope angle
2. PRA-layer
3. travel angle layer (Flow-Py output)
4. forest layer

The thresholds determining the boundaries of the classes, as figured out by Hesselbach (2023) and applied in this thesis, are shown in section 3.3.1.

In a first step, cells are classified based on their slope angles. Additionally, the terrain is classified regarding the travel angle. The intermediate class is determined

as the maximal classification obtained from slope and travel angle.

In a next step the classes are reclassified using forest and PRA data. Forest density and PRA can cause the reclassification of previous classes to lower classes. For example, in areas without PRA and in sparse forests, the ATES classes are reduced by one (ATES class 1 remains unchangend). In moderate forests, previous class 4 becomes class 3, while others become class 1. In dense forest previous class 4 is reclassified to class 2. In PRAs, classes within the same forest categories are reclassified to a lesser extent.

Finally, small isolated areas of a class are removed. The parameter 'ISL SIZE' determines the threshold for the size of the area that is removed.

2.6.2 Delineation of remote triggering zones

For the CAT maps zones where remote triggering is likely within the avalanche runout area are delineated using a dataset of 75 observed remotely triggered avalanches. From these observations, the distance from the trigger point to the release area was computed to estimate the probability of remote triggering depending on the distance to release area. The ArcGIS function "path distance" was used to calculate the potential for remote triggering based on the distance and the terrain curvature. (Harvey et al. 2018)

Chapter 3

Data and Methodology

We apply the two avalanche terrain classification methods, autoATES and CAT, to two test regions located in the Alps that are described in the following. In this thesis, the Institute for Snow and Avalanche Research (SLF) of Swiss Federal Institute for Forest, Snow and Landscape research (WSL) computed the CAT maps. We generated the ATES maps using the same algorithm and parameter settings as described by Hesselbach (2023) and Huber et al. (2023) in the conservative case. Section 3.2 outlines the used data for each classification method. Furthermore, the analyses and implementations in Flow-Py are described, as well as statistical methods employed for comparisons.

3.1 Study areas

One test region is a 150 km^2 area in the Austrian Alps (Sellrain, Tyrol) It is a popular region for skitouring with altitudes up to 3 100 m above sea level. Since 79% of the area is located above 2 000 m above sea level, only small parts are forested. The area is shown in Figure 3.2. It is a part of the study area analysed in Hesselbach (2023) and Huber et al. (2023) applying autoATES.

The second study region is an area of 600 km^2 located in the Swiss Alps (Davos, Grisons), the altitude ranges between 1 000 m and 3 200 m above sea level. 40% of the area is below 2 000 m, so a larger area is covered by forest compared to Sellrain region. The study area Davos is shown in Figure 3.3.

The study area Davos is four times larger than study area Sellrain. As a larger part of the area in Sellrain is located above 2 000 m above sea level than in Davos, smaller areas are forested in Sellrain than in Davos (see Table 3.1).

Table 3.1: Topographic facts of the study areas Sellrain (Tyrol, Austria) and Davos (Grisons, Switzerland).

	Sellrain	**Davos**
extent	150 km²	600 km²
area above 2 000 m	79%	60%
forested area	8%	24%
steep terrain (> 50°)	8.4%	2.8%

Figure 3.1 shows the hypsometry of each test region. In both test regions, the majority of the terrain lies between 2000 m and 2500 m above sea level. In Davos a larger area is below 1500 m above sea level compared to Sellrain. In both regions, the terrain is forested up to 2200 m above sea level. Because the terrain is lower in Davos, the percentage of forested area is higher than in Sellrain. Above 2800 m above sea level, a large percentage of the area is assigned to PRA, and the percentage decreases at lower elevation. In general, the mean slope angle increases with elevation. The decreasing slope angle above 3000 m in Sellrain is due to the small number of samples.

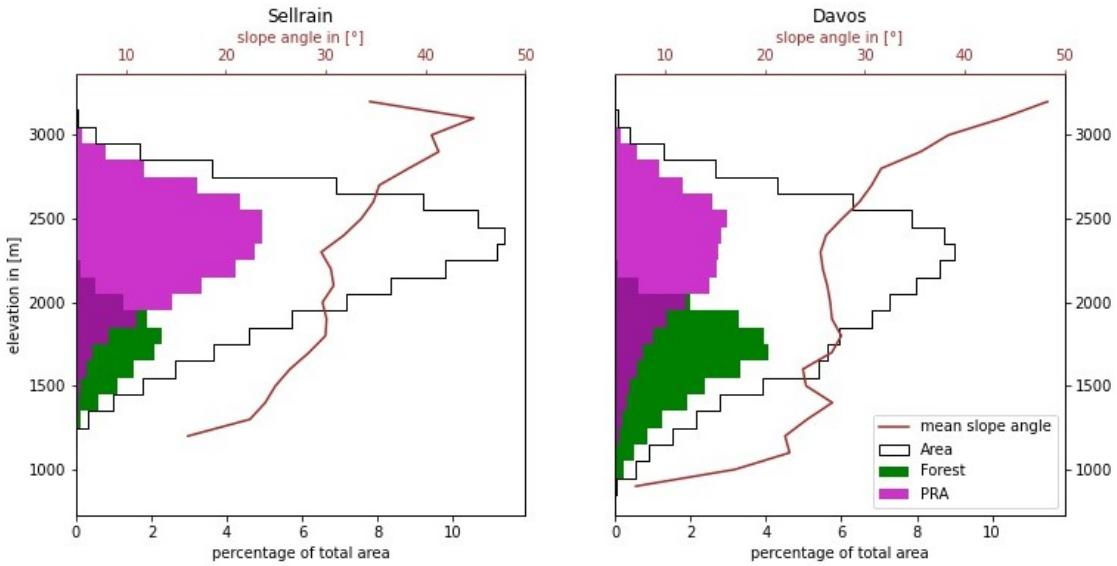

Figure 3.1: Hypsometry of each study region: the black line shows the distribution of elevation (in 100 m elevation bands). The green bars show the distribution of forest, the purple bars the PRAs (calculated using the algorithm of Veitinger et al. (2016)) relative to the total area of the test regions. The red line represents the mean slope angle in each elevation band.

3.2 Terrain and forest data

We generate ATES maps following the workflow initially developed by Larsen et al. (2020b), improved by Toft et al. (2023) and adapted to a test area in Tyrol by Hesselbach (2023). In the following we use the setup of parameters investigated by Hesselbach (2023).

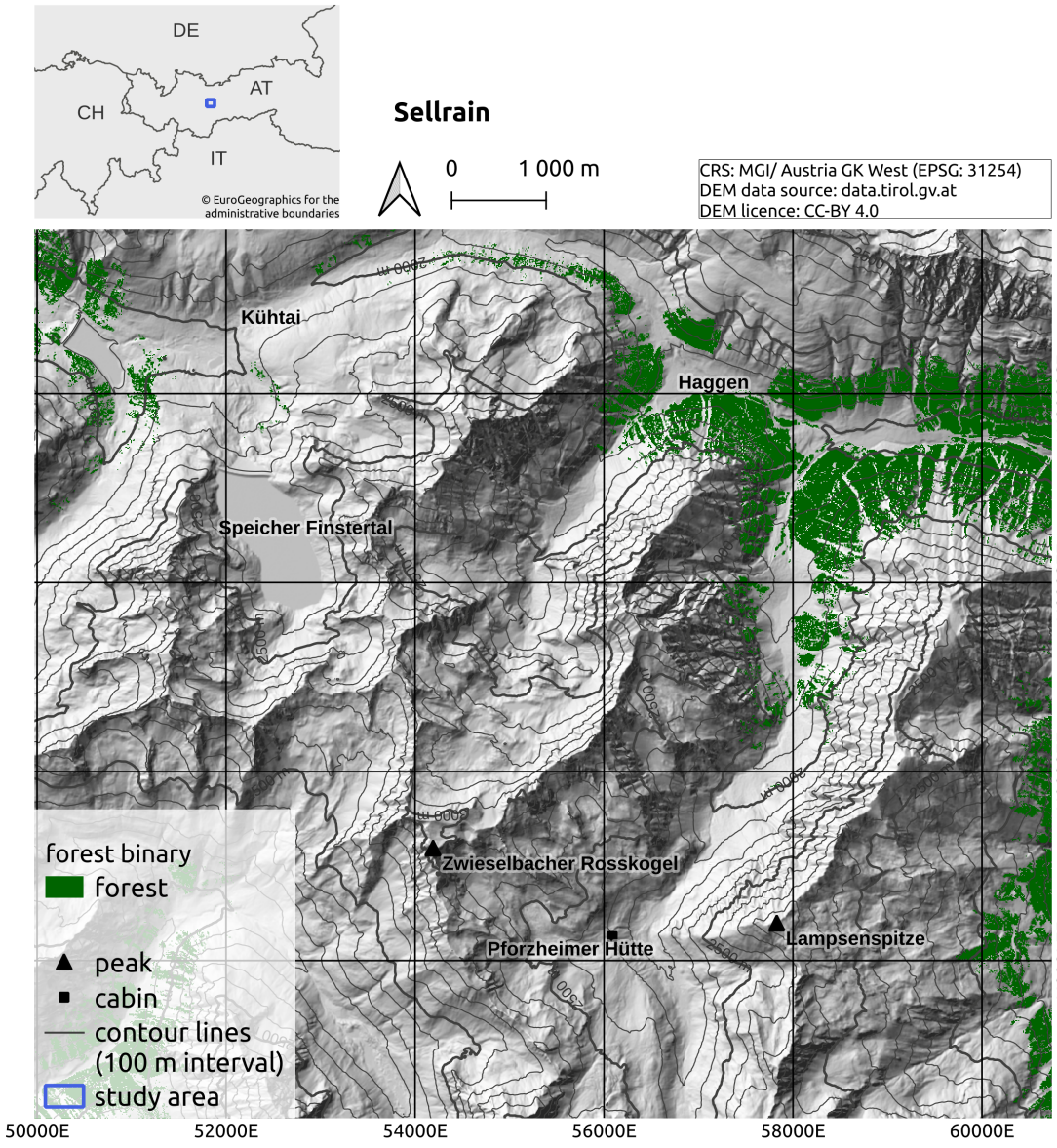

Figure 3.2: The terrain of study area Sellrain, forested areas are illustrated in green according to the binary forest layer.

The CAT and ATH maps have been calculated by the WSL Institute for Snow and Avalanche Research SLF. Generating ATES and CAT maps require a digital terrain model and a layer containing forest information. All data are in raster format.

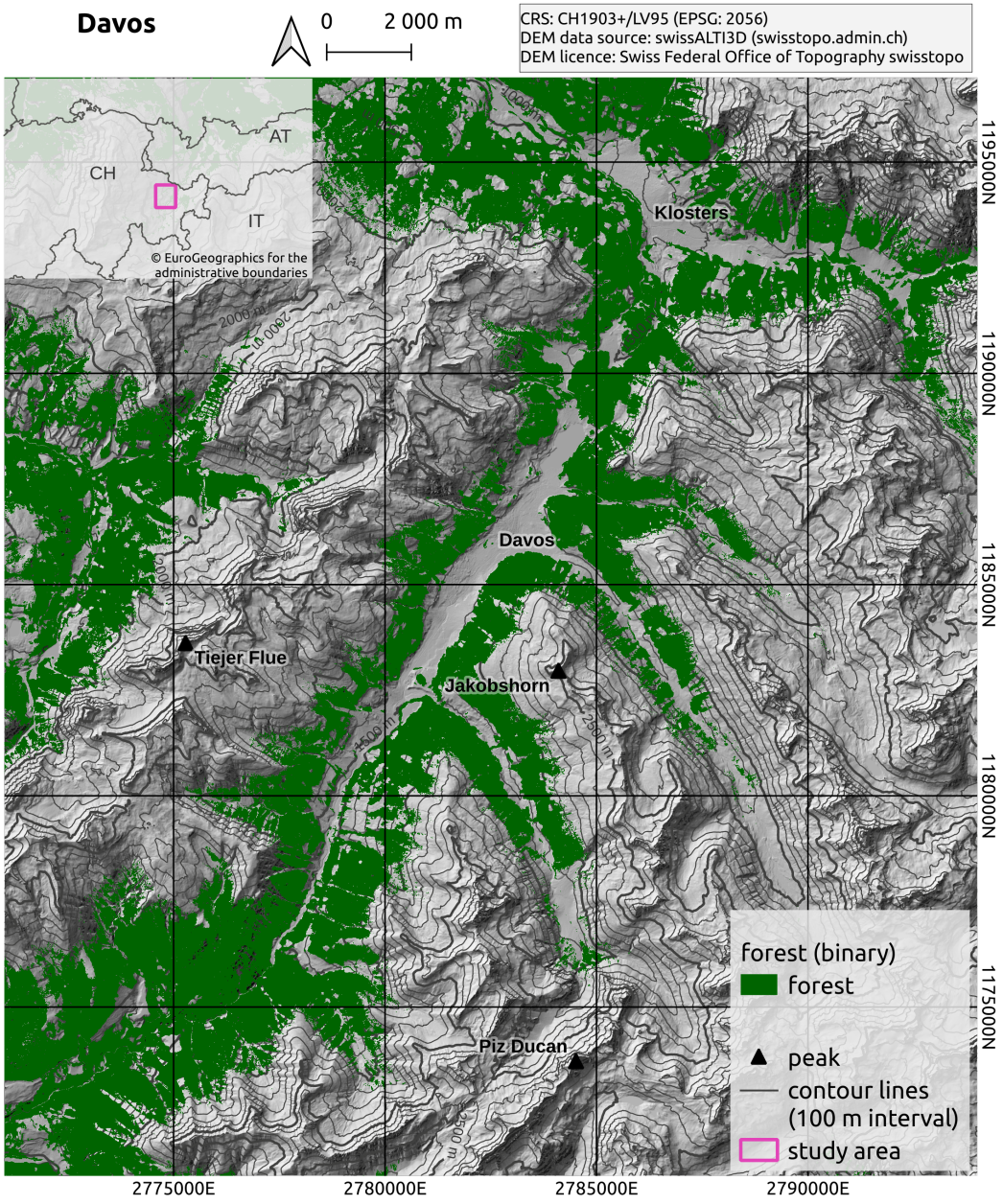

Figure 3.3: The terrain of study area Davos, forested areas are illustrated in green according to the binary forest layer.

3.2.1 Digital Elevation Model

Digital elevation model (DEM) is often used as a generic term for Digital Terrain Model (DTM) and Digital Surface Model (DSM) (Hirt 2014). For each classification method a DTM is used with a resolution of 10 m and for the CAT map a DTM with resolution of 5 m additionally. DEMs for the Tyrolean test region have been acquired from the Open Government Data of the Province of Tyrol through the public web coverage service (WCS). This data is licensed under the Creative

Commons Attribution 4.0 International Public License. The coordinate reference system (CRS) employed in this dataset is the MGI / Austria GK West (EPSG: 31254).

The digital elevation data for the Swiss test region is provided by the swissAlti3D DTM and swissAlti3D DSM, both accessible through the public server of the Federal Office of Topography, swisstopo. The dataset is the LV95 coordinate reference system (EPSG: 2056).

3.2.2 Forest layer

To create the ATES maps, a forest density layer is required in raster format with a 10 m resolution. We derived this percentage of canopy cover layers following Hesselbach (2023). Therefore, we calculated the difference of a DSM and a DTM with 1 m resolution using the QGIS raster calculator receiving the difference between the surface (including trees and buildings) and the terrain. Raster cells with a difference value larger than 5 m are assigned to value 1, indicating the presence of forest, while others are assigned to value 0, indicating no forest. We aggregated the resulting binary raster data using R-software, resampling it from a 1 m to a 10 m grid and summing all values. The output is a raster layer with 10 m resolution, containing values ranging from 0 to 100. To exclude artifacts, we clipped the resulting forest layer with a forest map (Bauerhansl et al. 2007) for the Austrian test region using the QGIS Clip function.

The forest layer for the Swiss region is derived using the same methodology with DSM and DTM in 0.5 m resolution due to availability. The resulting density raster layer with a resolution of 5 m is resampled to 10 m resolution for consistency with the Austrian region. To eliminate artifacts, we clip the resulting canopy density layer with a provided binary forest layer by Swiss Institute for Snow and Avalanche Research SLF (Bebi et al. 2022).

Creating the CAT map requires a binary forest layer. We determine empirically a canopy density threshold of 35% by comparing the forest density layer with a satellite image (Google 2023). Then, we compute a binary forest layer containing value 1 (forest) for canopy density larger than and equal 35% and value 0 (no forest) for canopy density less than 35%.

3.3 Methods

Section 3.3.1 represents the parameter configuration of the autoATES workflow used in this thesis. Section 3.3.2 describes the statistical metrics used for comparing the end products and intermediate steps of autoATES and CAT. Sections 3.3.4 and 3.3.3 mention adaptions and extensions within the open-source avalanche simulation tool Flow-Py. The former delineates the method to receive and store information of each simulated avalanche path. The latter extends these path analyses to compute the interaction between forested areas and avalanche paths, further this new information is integrated into the autoATES classifier.

3.3.1 Parameter configuration of the autoATES workflow

In the following analyses, the same workflow and parameter settings in the chain modules are used as Hesselbach (2023) figured out for the conservative case. In this thesis we use these parameters unless otherwise mentioned.

We calculate PRAs using the algorithm developed by Veitinger et al. (2016) and Sharp (2018) described in section 2.4.1. We employ the binary roughness (binary-rugg) model and set a PRA threshold of 0.3, since this model setup performed best when compared to observed release areas (Hesselbach 2023). Applying the PRA threshold, the continuous output raster file is converted to a binary format. Cells assigned values equal or greater than 0.3 are classified as PRA, cells with lower values as no PRA.

To simulate avalanches of size 3 (EAWS 2023), Hesselbach (2023) figured out the following input parameter for Flow-Py, which are described in more detail in section 2.5.1:

- alpha angle = 26°
- exp = 8 (default)
- R_{stop} = 3 x 10^{-4} (default)
- Z^{δ}_{lim} = 8849 m (height of Mount Everest) (default)

The thresholds for the autoATES classifier (described in 2.6.1) are represented in Table 3.2. $Threshold12$ represents the boundary between ATES classes 1 and 2 for each parameter. This means that ATES class 1 is assigned to areas with values less than or equal to $Threshold12$, while areas are classified as ATES class

2, when values are greater than or equal $Threshold12$ and less than $Threshold23$. Classes 3 and 4 are classified analogously using $Threshold23$ and $Threshold34$. Additional parameters include Isl size 'ISLS' of 1,000 and a sliding window 'WIN' of 1 (Hesselbach 2023).

Table 3.2: Parameterization of the autoATES classifier after Hesselbach (2023). $ThresholdXY$ represents the boundary between classes X and Y.

Input parameter	**Threshold12**	**Threshold23**	**Threshold34**
Slope angle threshold 'SAT'	28°	39°	45°
Alpha angle threshold 'AAT'	26°	32°	
Forest density threshold 'TREE'	10	25	65

3.3.2 Statistical metrics

For the quantitative comparison of the classification methods, we calculate statistical metrics such as accuracy, precision, recall and F-Score to provide an overall assessment. Additionally, we compute confusion matrices for a detailed analysis of classification agreement. Liu et al. (2014) provide a comprehensive overview of these statistical methods.

A confusion matrix is used to evaluate a prediction model by comparing its predictions with the actual classes. In this thesis, we compare two models using a confusion matrix without knowing the ground truth. Table 3.3 presents an illustrative example of a confusion matrix. True positives describe the number of raster cells which are assigned to class A by both models, while true negatives are assigned to not A by both models. False negatives and false positives denote the number of cells that are differently assigned by both models.

Accuracy measures the proportion of truly predicted or matching classes compared to the total number of predictions.

$$\text{accuracy} = \frac{\#\text{ matching classes (TP + TN)}}{\#\text{ raster cells (TP + TN + FP + FN)}} \tag{3.1}$$

Table 3.3: An example for a confusion matrix comparing the outputs of two models classifying class A or not class A. The notifications True Positives, False Positives, False Negatives and True Negatives can be explained by the matrix.

Model 1	**Model 2**	
	class A	**NOT class A**
class A	True Positive (TP)	False Negative (FN)
NOT class A	False Positive (FP)	True Negative (TN)

Recall describes the proportion of the number of cells assigned to class A by both models to the number of cells assigned to class A by model 1, while precision uses the number of cells assigned to class A by model 2 as the reference.

$$\text{recall} = \frac{\text{TP}}{\text{TP} + \text{FP}} \tag{3.2}$$

$$\text{precision} = \frac{\text{TP}}{\text{TP} + \text{FN}} \tag{3.3}$$

The F-Score is a mathematical score combining recall and precision to assess a classification performance.

$$\text{F-Score} = 2 * \frac{\text{precision} * \text{recall}}{\text{precision} + \text{recall}} \tag{3.4}$$

For a multi-class model, the metrics are calculated individually for each class and averaged to obtain a single value to assess the overall performance or agreement of the models.

We compute the metrics using the Python package scikit-learn (Pedregosa et al. 2011) with a weighted averaging mode to consider class imbalance.

3.3.3 Implementation of interaction between avalanches and forest in autoATES

The open-source autoATES model chain allows adaptations to its modules. The classifier accounts for forest by reclassifying forested areas to lower ATES classes. However, the interaction between avalanches and forests, such as braking of an avalanche in a forest, is not considered. Consequently, we implement a feature in Flow-Py resulting in an additional output layer, which represents the number of forested raster cells a path runs through. In this forest interaction layer, locations (raster cells) of paths are assigned to the number of forested cells previously hit.

The output raster layer shows the minimum of forest interaction values of all paths. Figure 3.4 shows schematically the distribution of routing flux from the startcell to childcells including the forest interaction.

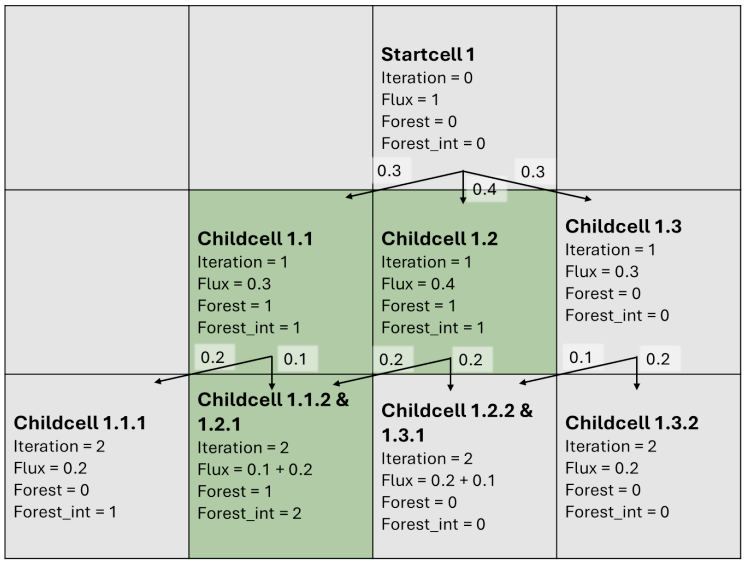

Figure 3.4: As in Figure 2.3. Additionally, the implemented forest interaction is illustrated. Green cells are forested (Forest = 1), the forest interaction value (Forest_int) is given for each cell of the avalanche path.

The autoATES classifier reclassifies cells, which are assigned to forest interaction value 2 or higher (corresponding to an avalanche path through at least 20 m forest), to a lower class. If a cell has a value higher than 8, which means, that the path ran through more than eight forested cells before (avalanche path through 80 m forest), ATES class 3 is reclassified to ATES class 1. The thresholds of forest interaction 2 and 8 are first approaches, in further analyses these thresholds may be adapted.

We implemented the forest interaction in the Flow-Py branch 'PS_flowpy_forestInteraction' in the Avaframe repository (Oesterle et al. 2024) and used this branch to generate the forest interaction layer.

3.3.4 Thalweg and path analyses with Flow-Py

A further extension in Flow-Py provides information about each path simulated for every release cell by Flow-Py. The goal is to compute various parameters along a thalweg for each path, enabling a two-dimensional thalweg representation that is more understandable and verifiable compared to the raster outputs.

The thalweg is determined by the main flow direction (Oesterle et al. 2024), in

this thesis we calculate the position of thalweg for every iteration by the center of energy (coE) or center of routing flux (coF) (see equation 3.6). The path on the other hand includes all cells that received flux.

For the coE flow energy E is used and calculated as:

$$E = \frac{1}{2} F v^2 = F z^{\delta} g, \tag{3.5}$$

analogically to the definition of kinetic energy. Flux F can be interpreted as mass, z^{δ} as the kinetic energy height (Körner 1980; D'Amboise et al. 2022b). Thus, velocity is calculated as $v = \sqrt{2 z^{\delta} g}$ with the gravitational acceleration g (see section 2.5.1). The flow energy values can be interpreted as kinetic energy. However, it is important to note that these values can not be quantitatively equated with kinetic energy, since the interpretation of flux as mass does not imply a direct equivalence.

Any average of variable X can be weighted with variable Y using the following calculation (Tiwari et al. 2022):

$$X_{coY} = \frac{\sum_{i=0}^{n} (Y_i * X_i)}{\sum_{i=0}^{n} Y_i}. \tag{3.6}$$

The index i represents all cells of one iteration step in the avalanche path simulation. The position of the coE - thalweg is computed by the coE of the x and y coordinates of every iteration step:

$$x_{coE} = \frac{\sum_{i=0}^{n} (E_i * x_i)}{\sum_{i=0}^{n} E_i}. \tag{3.7}$$

$$y_{coE} = \frac{\sum_{i=0}^{n} (E_i * y_i)}{\sum_{i=0}^{n} E_i}. \tag{3.8}$$

The position of the coF - thalweg can be computed analogously.

To compute various parameters (e.g., topography elevation z) along the thalweg, we calculate the coE / coF of the parameter replacing X in equation 3.6 with the parameter (e.g., z_{coE}). It is important to note, that this weighted value (e.g., z_{coE}) differs from the value, that is read out at the location (x, y coordinate) of the thalweg (e.g., $z(x_{coE}, y_{coE})$).

To investigate differences in the thalweg between coE and coF computation, first a simple example is examined where an avalanche is simulated on an inclined plane starting from a single release cell. The two-dimensional plots are shown in Figure 3.5. The upper chart represents the terrain including contour lines with the simulated flow energy of the path and the location of the thalweg computed using the coE (in red) and coF (in blue). As expected, the path follows a downward trajectory with lateral spreading, the thalweg using coE and coF align closely along the path's centerline. coE and coF share the same locations.

The left panels in the middle of Figure 3.5 display the elevation profile of the topography (z_{coE} and z_{coF}) and the energy height z^{δ} along both thalwegs, resulting in nearly-identical outputs computed with coE and coF. The topography shows the constant descending terrain, z^{δ}_{coE} and z^{δ}_{coF} increase with the descending terrain indicating increasing velocity.

In Figure 3.5, the plots on the right side show the sum of flux and the travel length s_{coE} and s_{coF} in each iteration step. The travel length increases proportional with iteration steps. The sum of flux exhibits a decreasing trend with iteration, indicating flux loss. Due to the R_{stop} criterion, the routing stops if the flux reaches a minimal threshold (see section 2.5.1). The precipitous decline at iteration 420 is attributable to the end of the domain.

Figure 3.6 presents analogous plots to those in Figure 3.5, showing an example in real topography. Despite the shift to real terrain, the positions of coE and coF remain similar because Flow-Py iterates spatially. The cells calculated in each iteration step are in spatial proximity, leading to similar locations (and values) centered according to flux and energy. Additionally, the routing flux considers the cells that move in the respective step meaning that the flux can be interpreted as moving mass rather than total mass. Due to the similarity of coE and coF, the further thesis employs the coE to define the thalweg. The coE considers flux and velocity, ensuring that cells with either a small flux and large velocity or cells with a large flux and small velocity are appropriately accounted. When using coF or even center of velocity, one of these described cells becomes less significant. Furthermore, the interpretation of flux as mass lacks since the release area is represented by a single raster cell. Additionally, the flux is not conserved, as the sum of flux is not constant in each iteration step.

Compared to the example on the inclined plane (Figure 3.5), in this scenario in real topography, z^{δ} reaches the value 0 indicating that the flow is stopped due to

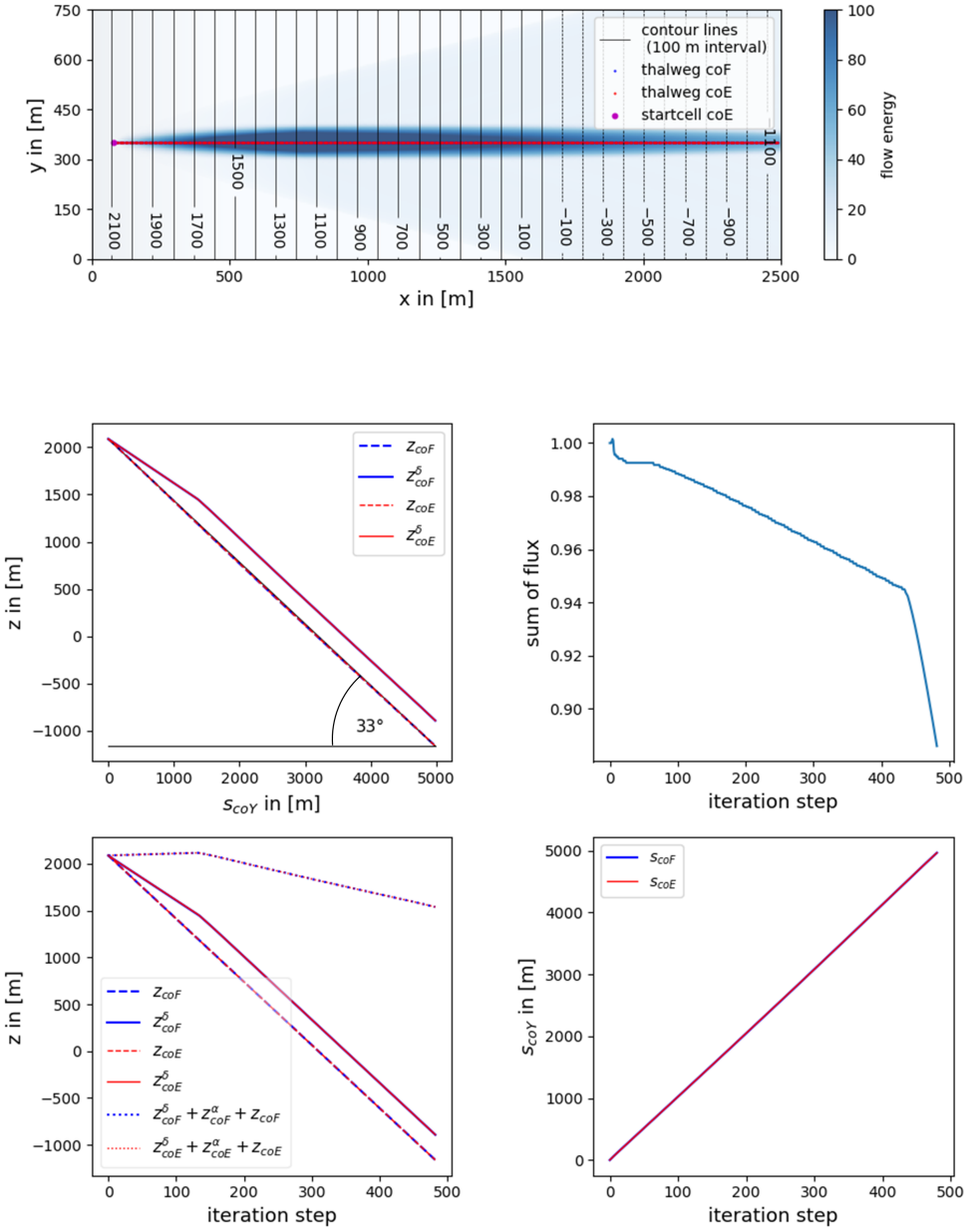

Figure 3.5: The simulation of an avalanche starting in one release cell at an inclined plane is represented. In the top panel the flow energy of the path and two corresponding thalwegs are shown, calculated as center of energy (coE in red) and center of flux (coF in blue) applied to the x- and y-coordinate. The terrain is demonstrated using contour lines. At the lower left side, both plots show the elevation of the topography (z_{coE} and z_{coF}) and z delta (z^{δ}_{coE} and z^{δ}_{coF}) along the thalweg computed by coE and coF. The lines indicating $z + z^{\delta} + z^{\alpha}$ represent the total energy along the respective thalweg, with the dissipative energy z^{α} (see section 2.5.1). At the upper plot, the elevation is demonstrated depending on the distance travelled (s_{coE} and s_{coF} computed via coE in red and coF in blue, respectively), the lower plot depends on the iteration step. The angle represents the runout angle between the horizontal and the line through the release and deposition points. The right panels show the sum of flux (top) and the travel lengths s_{coE} and s_{coF} (bottom) for every iteration step along the thalweg.

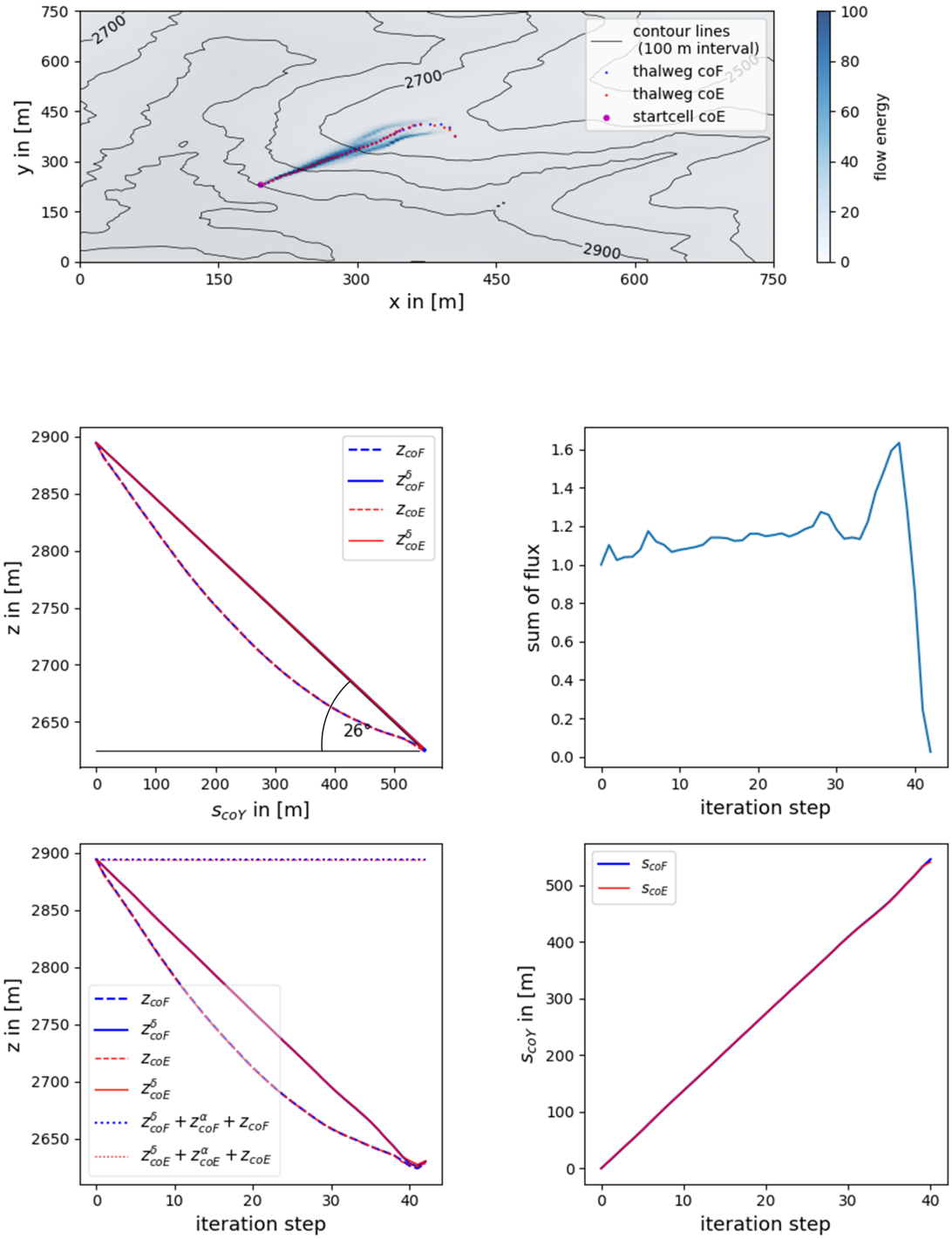

Figure 3.6: As in Figure 3.5 for a simulation in real terrain in the Sellrain test region.

the alpha angle (26°). A further sign is the calculated runout angle between the horizontal and the line through release in deposition points of 26°. Furthermore we investigate that the energy is conserved, since the sum of z, z^{δ} and the dissipative energy z^{α} is constant according to the energy line model (Körner 1980; D'Amboise et al. 2022b).

The sum of routing flux increases with iteration steps exceeding the value of 1. However, this contradicts the expected behavior, since the flux starts with a value of 1 in the initial step, further dividing to child cells in subsequent iterations. Thus, there are evident discrepancies in the computation of these iteration steps, which leads to the conclusion that the flux is not conserved.

We implement a method to investigate the results Flow-Py simulation in a two-dimensional thalweg representation, which leads to the conclusion that flux is not conserved in each iteration step. For instance, further research could be conducted to examine the flux conservation.

We implement the path analyses in the Flow-Py branch 'PS_flowpy_path' in the Avaframe repository (Oesterle et al. 2024) and used this branch for the following path analyses.

Chapter 4

Results and Discussion

The autoATES and CAT workflows are applied to the two test regions Sellrain and Davos. The ATES and CAT maps are compared qualitatively and quantitatively. Both workflows contain avalanche runout computed with two different avalanche simulation tools. The results of the model chain modules, primarily the runout results are compared between both methods. Further, an adaptation of the autoATES workflow is presented by including the interaction between avalanches and forest in Flow-Py and the autoATES classifier. Furthermore, the avalanche mobility results of the autoATES workflow are analysed according to the avalanche size classification of each path. Additionally, the terrain of the test regions are compared in order to the destructive potential of avalanches. In each section, the results are described and discussed. Sections 4.2.4 and 4.4.1 delineate separate discussions for a comprehensible structure.

4.1 Application of ATES and CAT in study areas Sellrain and Davos

Figure 4.1 shows the ATES and CAT maps in Sellrain. We create the ATES map using the autoATES workflow and parameter configuration as in Hesselbach (2023); see section 3.3.1, while the CAT layer is provided by the SLF. ATES and CAT applied to the study area Davos are shown in Figures A.1 and A.2.

Figure 4.2 shows the distribution of ATES and CAT classes in both test regions. The distribution of the classes differs in the regions. In Sellrain a larger area is assigned to ATES classes 3 and 4 compared to Davos, while a larger part is assigned to ATES class 1 in Davos. The majority of the Sellrain region is covered by ATES class 'complex' (56.4%), of Davos by class 'simple' (42.2%) (Figure 4.2a). Figure 4.2b shows that CAT does not classify 29.6% of the area in Sellrain and in Davos

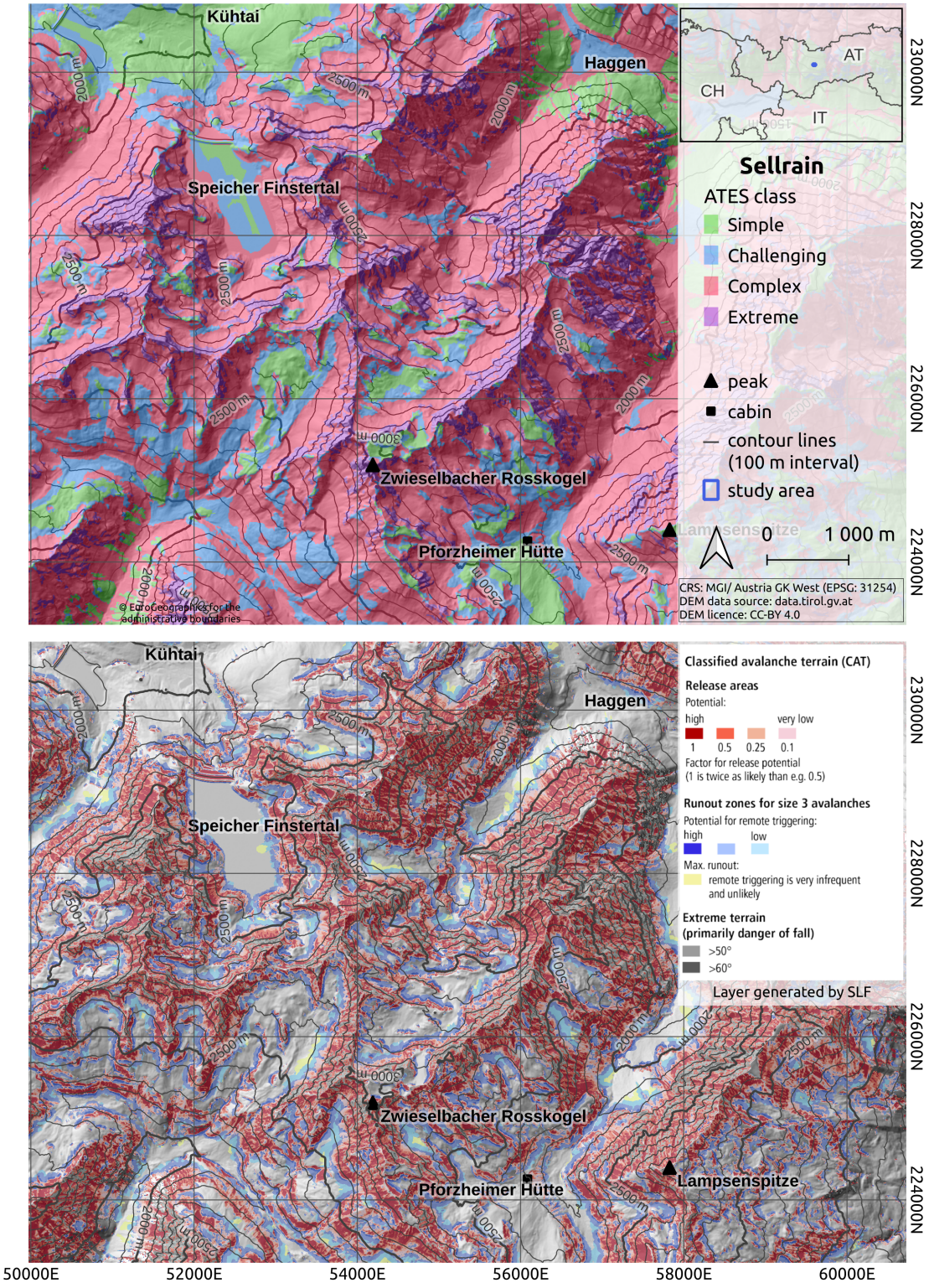

Figure 4.1: Classification maps ATES (top) and CAT (bottom) in the study area Sellrain. The ATES map classifies the terrain into the four ATES classes 'simple' (green), 'challenging' (blue), 'complex' (red) and 'extreme' (purple). The CAT map shows the potential of release areas (red), remote triggering zones (blue), maximal avalanche runout (yellow) and areas with slopes steeper than 50° (grey) in respective colour schemes.

50.7% of the area. In Sellrain, the part of the area assigned to PRAs (44.7%) is almost twice as in Davos (26.6%).

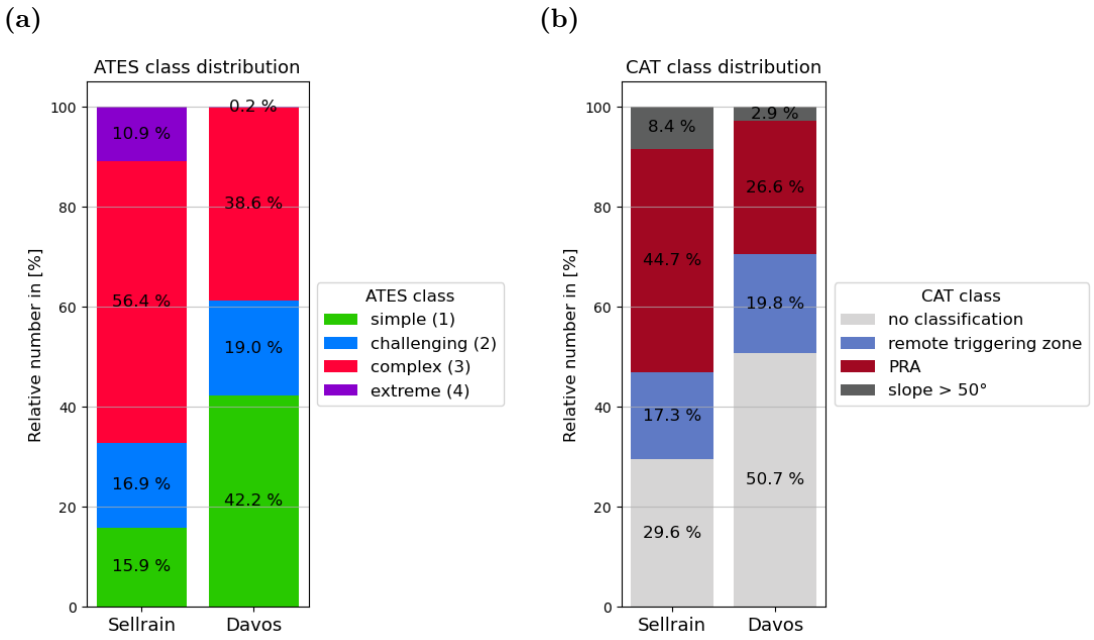

Figure 4.2: The distributions of parts of area of (a) the four ATES classes 'simple' (green), 'challenging' (blue), 'complex' (red), 'extreme' (purple) and (b) CAT categories 'no classification' (light grey), 'remote triggering zone' (blue), 'potential release area' (red) and 'slope stepper than 50°' (dark grey) are shown for each test region.

4.2 Comparison of ATES and CAT results

For a comparison of the end products and the intermediary results of autoATES and CAT classification, the raster layers need the same extent and resolution. The extent of study area Sellrain is reduced to 100 km^2 for the comparison between ATES and CAT since the CAT maps are smaller in this region. The CAT map has a resolution of 5 m, the ATES map and the layers with intermediary products of 10 m. For the comparison the CAT map is resampled to a resolution of 10 m using QGIS.

4.2.1 Qualitative comparison in a small excerpt

In Figure 4.3 ATES and CAT are represented in an excerpt of the Sellrain test region. The popular skitouring area includes Pforzheimer Hütte, located 2 308 m above sea level and Zwieselbacher Rosskogel 3 081 m above sea level. This area is

not covered by forest.

The locations assigned to class 4 (extreme, in purple) in ATES map is similar to areas with slopes steeper than 50° (light and dark grey) in the CAT map, for example in the south-east of Zwieselbacher Rosskogel.

The area in the north-east of Zwieselbacher Rosskogel is mostly assigned to ATES class 1 (simple, in green) with parts of class 2 (challenging, in blue). This area is mostly not classified as avalanche prone in the CAT layer, except the 'challenging' area in the ATES map corresponds to release areas and zones of remote triggering with low potential in the CAT map. A similar pattern occurs in the south of Pforzheimer Hütte, the area is assigned to class 1 in the ATES map, while it is not classified in the CAT map.

The south-eastern face of Zwieselbacher Rosskogel is mostly assigned to ATES class 3 (apart from class 4 in the upper part). In the CAT layer the terrain consists mainly of PRAs and runout, including parts that are not classified.

Figure 4.4 shows the two classification layers for the area around Jakobshorn close to Davos. This region is at a lower elevation than the area around Pforzheimer Hütte (cf. Figure 4.3), with Davos at 1 560 m above sea level and Jakobshorn at 2 590 m.

The eastern face of Jakobshorn is mostly classified as ATES classes 2 and 3. The same area is classified as PRAs and runout zones in the CAT map. In the lower part of the slope, just a few separated avalanche runout zones are visible in the CAT layer. These zones correspond well to ATES class 3. Between those the CAT layer is not classified, ATES class 1 is assigned due to forested terrain (cf. Figure 3.3).

On the western face of Jakobshorn, ATES class 3 is assigned approximately in the same area as PRAs and remote triggering zones in the CAT map. ATES class 2 corresponds to the zones of maximal runout, where remote triggering is very unlikely (yellow). Below these zones and at the ridges the areas of ATES class 1 and no CAT category are similar.

In the valley bottom, many areas assigned to ATES class 2 are not classified in the CAT map.

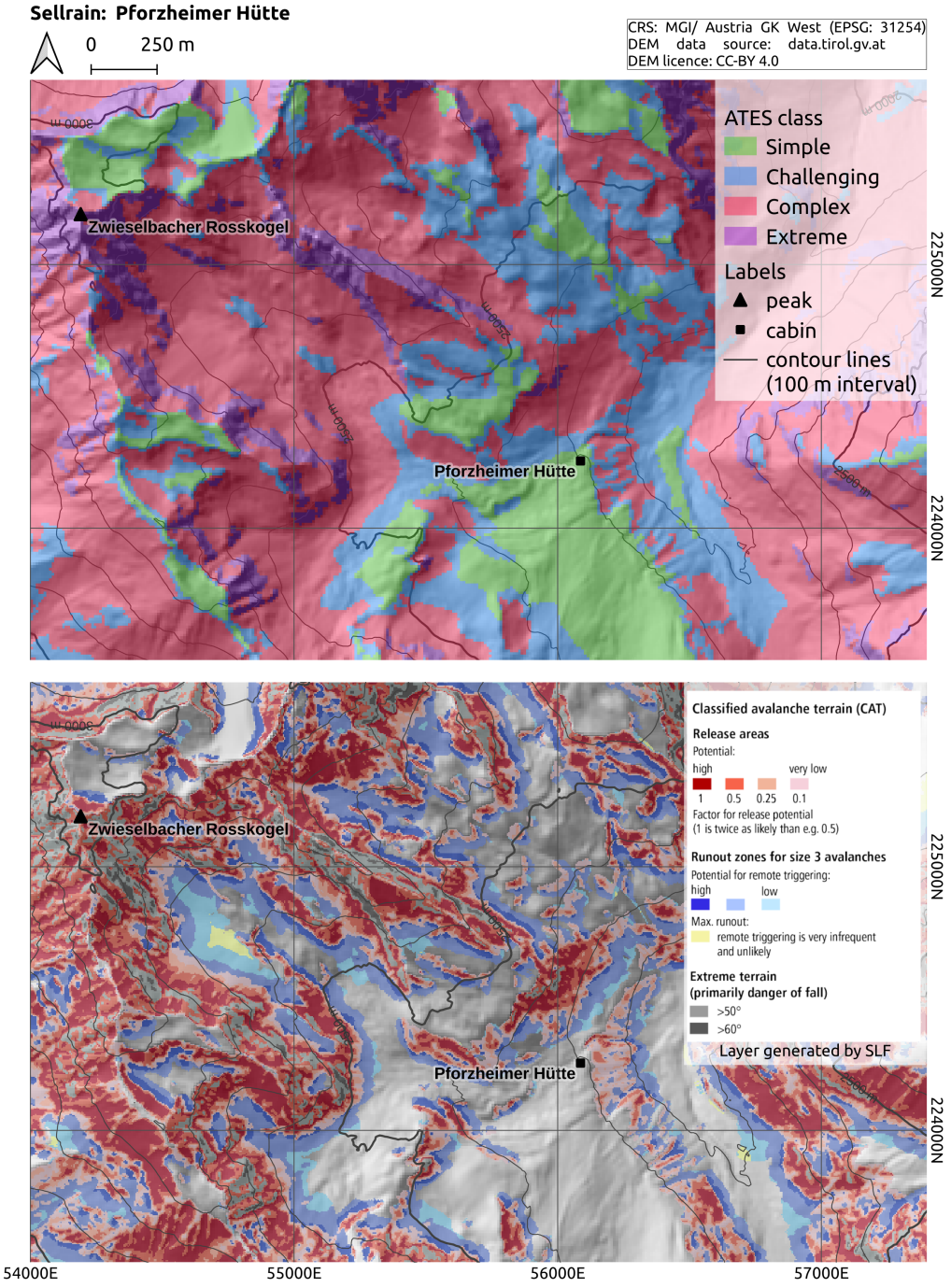

Figure 4.3: Classification maps ATES (top) and CAT (bottom) in an area around Pforzheimer Hütte in Sellrain. The ATES map classifies the terrain into the four ATES classes 'simple' (green), 'challenging' (blue), 'complex' (red) and 'extreme' (purple). The CAT map shows the potential of release areas (red), remote triggering zones (blue), maximal avalanche runout (yellow) and areas with slopes steeper than 50° (grey) in respective colour schemes.

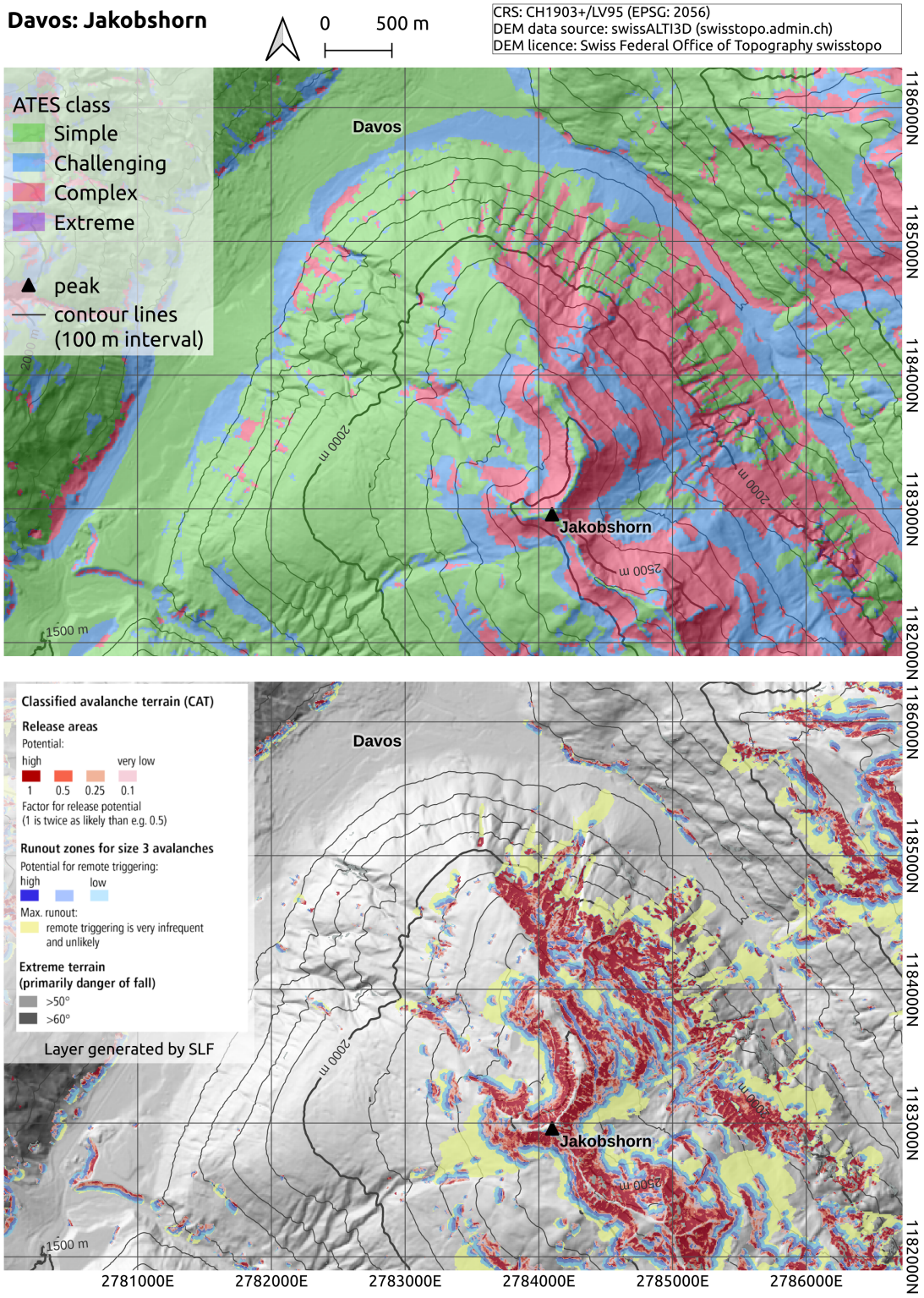

Figure 4.4: As in Figure 4.3 in an area around Jakobshorn in the Davos test region.

4.2.2 Quantitative comparison in whole test regions

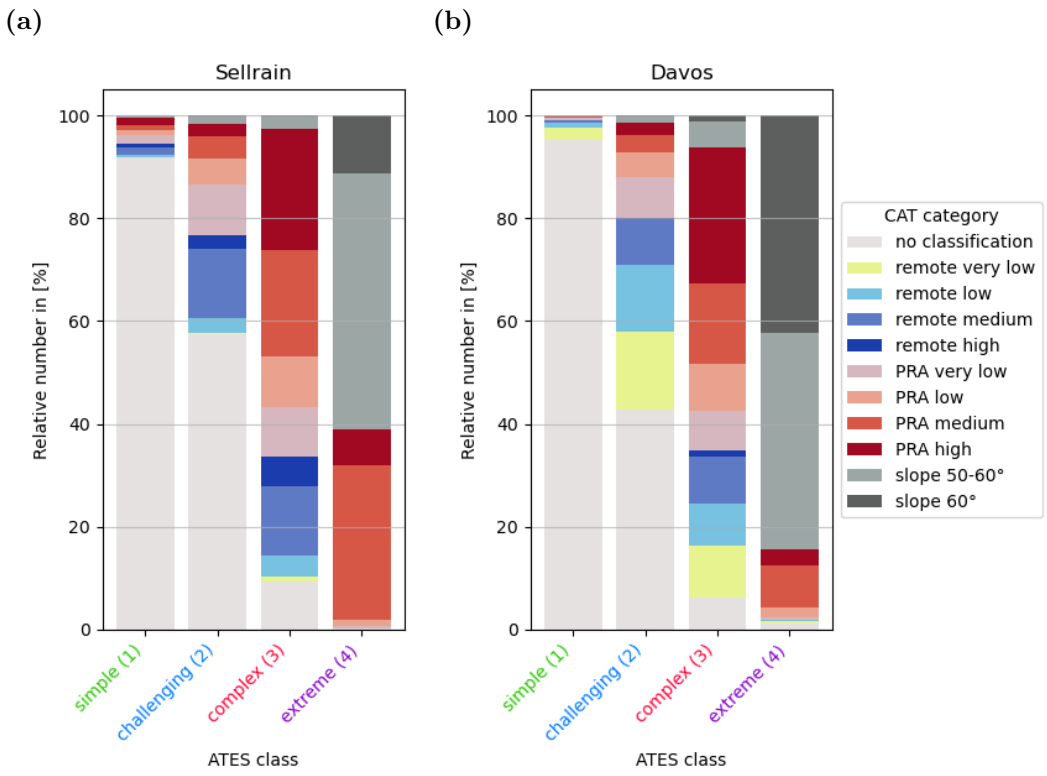

Figure 4.5: The barplots show the distribution of the CAT categories depending on the ATES classes 'simple', 'challenging', 'complex' and 'extreme'. The CAT categories are potential of release areas (red), remote triggering zones (blue), maximal avalanche runout (yellow) and areas with slopes steeper than 50° (grey), with potential represented in respective colour schemes. The amount of raster cells assigned to CAT and ATES classes are considered. The analysis is represented for each study region: (a) Sellrain, (b) Davos.

Figure 4.5 shows the distribution of CAT categories depending on the ATES classes. In both test regions, CAT does not classify at least 90% of the terrain, which is assigned as 'simple' (ATES class 1).

More than 60% (Sellrain) and 80% (Davos) of the area classified as ATES class 4 (extreme) is assigned to very steep terrain (steeper than 50°) by CAT. The other parts are classified as release areas with medium and high potential. It is worth to note that in Davos, only 0.2% of the test area is assigned to ATES class 4 (see Figure 4.2a).

Areas assigned to ATES class 2 (challenging) are not classified in CAT maps in almost 60% (Sellrain) and 40% (Davos). The other 40% and 60% are divided into

potential remote triggering zones and PRAs.

The distribution of CAT categories in areas, where ATES assigns the terrain as 'complex' (class 3), is similar in Sellrain and Davos. The areas are assigned to all different CAT categories, mostly to PRAs (approximately 60% in both study areas).

4.2.3 Statistical comparison of ATES and CAT

In the following, we try to merge the eleven CAT categories into four classes that correspond to the four ATES classes. When focusing on ATES public and technical model (Tables 2.5 and 2.4), ATES classes are computed considering more factors than the CAT categories slope angle, PRA and avalanche runout. This complexity makes it challenging to establish direct correspondences between CAT and ATES classes. In previous sections 4.2.1 and 4.2.2 some corresponding patterns emphasize between ATES and CAT maps. Thus, the CAT categories are merged to four classes:

- class 1: no classification
- class 2: remote triggering with very low, low, medium potential
- class 3: remote triggering with high potential; PRA with very low, low, medium, high potential
- class 4: slope steeper than 50°

The distribution of ATES classes dependent on the merged CAT classes is depicted in Figure 4.6. Within the first CAT class (no classification), ATES class 1 dominates as expected. However, ATES classes 2 and 3 also appear here. The second CAT class (remote triggering zone with very low, low and medium potential) is mostly covered by ATES class 3, in Sellrain region a small part by ATES class 4. In the third CAT class (high potentially remote triggering zone and release areas with very low, low, medium and high potential) ATES class 3 appears mostly, and small areas of ATES classes 2 and 4, additionally. In the fourth CAT class (slope is steeper than 50°), ATES class 4 dominates in Sellrain, and ATES class 3 in Davos. Notably, the coverage of ATES class 4 is minimal in Davos.

The barplots in Figure 4.7 show the total distribution of the four merged CAT classes in each test area. In Sellrain, CAT class 3 covers the largest area, while in Davos, CAT class 1 predominates, followed by class 3. ATES class 3 covers approximately 10% more of the area than CAT class 3 in both regions, while CAT class 1 spans a larger area as the same ATES class. Generally, the overall

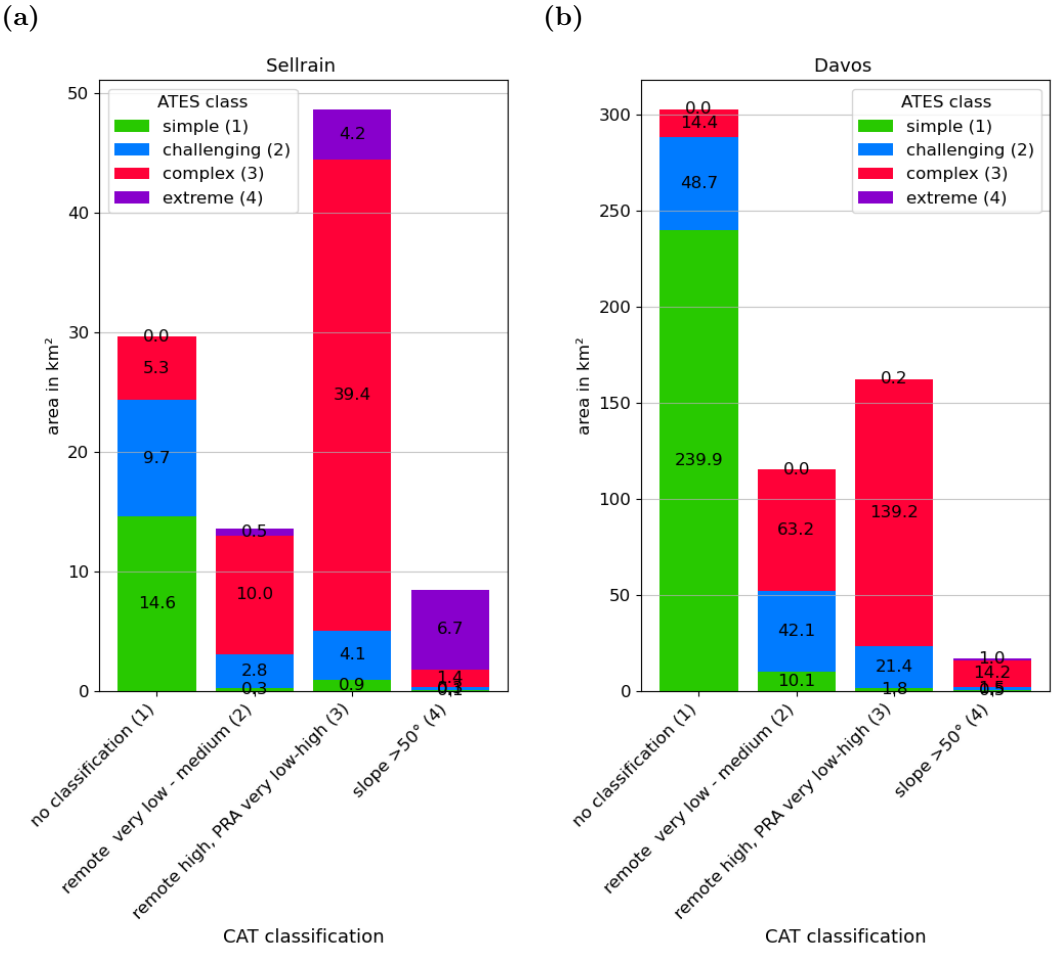

Figure 4.6: The CAT categories are merged into four categories: 1) no classification, 2) potential of remote triggering: very low, low, medium, 3) potential of remote triggering: high, potential of release area: very low, low, medium, high, 4) slope steeper than 50°. The spatial distribution of the ATES classes ('simple' in green, 'challenging' in blue, 'complex' in red, 'extreme' in violet) is shown dependent on these merged CAT classifications for (a) Sellrain and (b) Davos. The numbers in the bars describe the area in km² assigned to the ATES and CAT class, respectively.

distribution of the four classes of both methods ATES (Figure 4.2a) and CAT (Figure 4.7) are similar.

Table 4.1 shows the agreement between the four CAT and ATES classes. Considering class 1, CAT classifies 92% (Sellrain) and 95% (Davos) of the terrain same as ATES. The agreement diminishes for class 2. In 17% (Sellrain) and 37% (Davos) of the terrain, where ATES assigns class 2, the CAT class is also 2. The agreement for classes 3 and 4 are at least 60%.

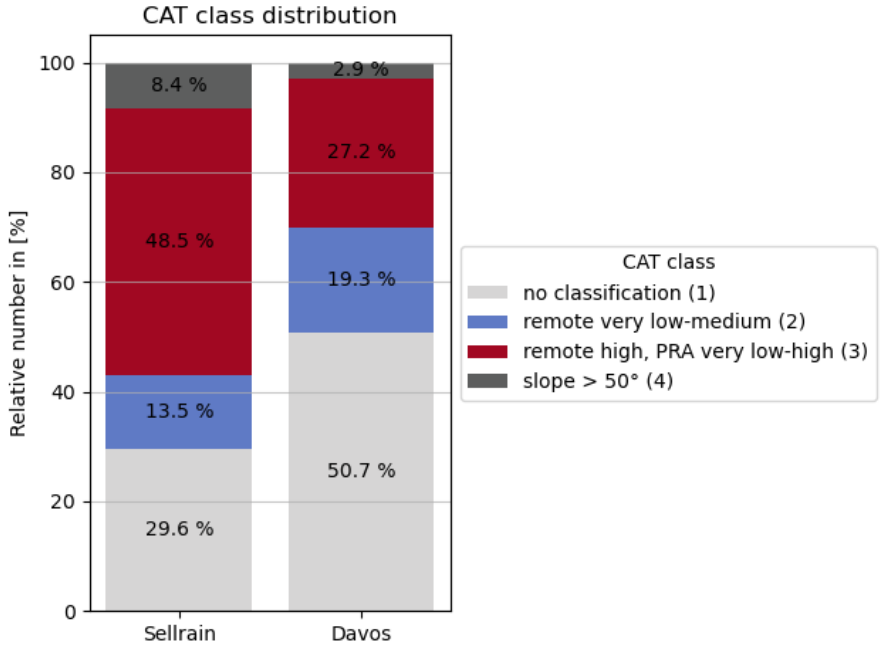

Figure 4.7: The distribution of the four defined CAT classes are shown for each study area. The CAT classes should correspond to the four ATES classes, they are merged from the following CAT categories: class 1 (light grey): no classification, class 2 (blue): remote triggering zones with very low + low + medium potential, class 3 (red): remote triggering zones with high potential + release area with very low + low + medium + high potential, class 4 (dark grey): slope steeper than 50°.

Different variants of merged CAT classes

Since CAT classes are merged subjectively, alternative combinations are identified to merge CAT categories into four classes, corresponding to the four ATES classes. In Table 4.2, different combinations for merged CAT classes are shown. In the first variant (analysed previously), CAT and ATES classes 1 and 4 agree well (Table 4.1), so they are not modified in variant 2 and 3 of CAT classes.

For the three variants of merged CAT classes, statistical metrics, such as accuracy, precision, recall and F-Score are calculated in order to compare the performance (Table 4.3). The metrics have highest values for the second variant and lowest for the third, resulting in the highest agreement of the second variant of merged CAT classes with the four ATES classes.

For a detailed analysis, Table 4.4 represents the confusion matrix for variant 2. The confusion matrix for variant 3 is in Table A.1. Since the classification variants do not alter concerning classes 1 and 4, the agreement remains as in variant 1. However, the agreement for class 2 is reduced compared to variant 1. In Sellrain

Table 4.1: Area and percentage agreement (of pixel cells) comparing the ATES classes with the four merged CAT classes. The results are shown for each test area. The values that show the matching classes (similar as True Positives) are highlighted in bold.

	Sellrain				**Davos**			
CAT	**class** 1	**class 2**	**class 3**	**class 4**	**class 1**	**class 2**	**class 3**	**class 4**
ATES								
class 1 [km²]	**15**	0.3	0.93	0.08	**240**	10	1.8	0.5
	92%	1.9%	5.8%	0.5%	**95%**	4%	0.7%	0.2%
class 2 [km²]	9.7	**2.8**	4.1	0.27	49	**42**	21	1.5
	57%	**17%**	24%	1.6%	43%	**37%**	19%	1.3%
class 3 [km²]	5.3	10	**39**	1.4	14	63	**140**	14
	9.4%	18%	**70%**	2.5%	6.2%	27%	**60%**	6.1%
class 4 [km²]	0.02	0.007	4.2	**6.7**	0.01	0.01	0.16	**0.96**
	0.21%	0.06%	39%	**61%**	1.1%	0.94%	14%	**84%**

Table 4.2: The merged CAT categories in four classes that correspond to the four ATES classes. The differences in categories in the variants are highlighted in bold.

CAT categories	**variant 1 (see above)**	**variant 2**	**variant 3**
ATES class			
class 1 (simple)	no classification	no classif.	no classif.
class 2 (challenging)	potential for **remote triggering**:		
	very low,low, **medium**	very low, low	very low, low, **medium, high**
class 3 (complex)	potential for **remote triggering**:		
	high	**medium, high**	
	PRA very low, low, medium, high potential		
class 4 (extreme)	slope $> 50°$	slope $> 50°$	slope $> 50°$

Table 4.3: Statistical metrics for the three variants of merged CAT classes in % to assess the agreement of the four merged CAT classes and the four ATES classes. Accuracy, precision, recall and F-score are shown for test regions Sellrain and Davos.

	Sellrain				**Davos**			
	accuracy	**precision**	**recall**	**F-score**	**accuracy**	**precision**	**recall**	**F-score**
variant 1	63	66	63	64	71	73	71	72
variant 2	69	64	69	66	72	72	72	72
variant 3	61	65	61	63	70	73	70	72

Table 4.4: Area and percentage agreement (of pixel cells) comparing the ATES classes with the four merged CAT classes (variant 2). The results are shown for each test area. The values that show the matching classes (similar as True Positives) are highlighted in bold.

	Sellrain				**Davos**			
CAT	**class 1**	**class 2**	**class 3**	**class 4**	**class 1**	**class 2**	**class 3**	**class 4**
ATES								
class 1 [km²]	**15**	0.09	1.1	0.08	**240**	9	2.9	0.5
	92%	0.6%	7.1%	0.5%	**95%**	3.6%	1.1%	0.2%
class 2 [km²]	9.7	**0.56**	6.4	0.27	49	**32**	31	1.5
	57%	**3.3%**	38%	1.6%	43%	**28%**	28%	1.3%
class 3 [km²]	5.3	2.9	**47**	1.4	14	42	**160**	14
	9.4%	5.2%	**83%**	2.5%	6.2%	18%	**69%**	6.1%
class 4 [km²]	0.02	0.0003	4.2	**6.7**	0.01	0.01	0.16	**0.96**
	0.21%	0.003%	39%	**61%**	1.1%	0.8%	14%	**84%**

CAT class 2 is classified in 3.3% of the terrain designated as class 2 by ATES. Similarly, in Davos this value decreased to 28%. Conversely, the values for class 3 have improved: in Sellrain, 83% of the terrain assigned to ATES class 3 is also classified as CAT class 3, in Davos 69%. This improvement contributes to a better overall performance.

When attempting to match ATES and CAT classes, variant 1 exhibits slightly worse

performance compared to variant 3, but the agreement is more evenly distributed.

4.2.4 Discussion of the differences between ATES and CAT

In general, autoATES and CAT end products as well as the results of their intermediate steps represent specific scenarios characterized by the chosen parameter setups. Modifying the parameters would lead to different ATES and CAT maps, consequently affecting the results of the comparison. CAT maps offer a more detailed representation compared to ATES. Firstly, CAT maps have a higher resolution with both input data and end products of 5 m grid size compared to ATES maps with 10 m resolution. Secondly, CAT classifies terrain into eleven distinct classes including release areas and remote triggering zones with differentiated potential, while ATES classifies the terrain into four classes. It is important to mention that the distribution of these classes represented in CAT and ATES maps is specific to one scenario. The more detailed the map, the greater the shift in distribution for various scenarios.

Furthermore, the classification maps are neither true or wrong, nor better or worse, especially as they show entirely different outputs. However, Toft et al. (2023) and Sykes et al. (2024) validated autoATES maps by using benchmark maps, which combine three individual ATES maps created by experts.

Refering to the first research question *'How do ATES and CAT maps compare in these two Alpine test regions? '*: In the qualitative and quantitative comparisons, ATES class 'simple' and no classification in the CAT map correspond well. Toft et al. (2023) and Sykes et al. (2024) also figured out a high accuracy of class 1 between autoATES maps and ATES benchmark maps. Sykes et al. (2024) criticise the underprediction of autoATES class 4. However, areas assigned to ATES class 'extreme' match with CAT categories very steep terrain and release areas with at least high potential, indicating extreme terrain.

ATES classes 2 and 3 contain a wide range of CAT categories, posing challenges finding corresponding CAT classes. On the other hand, the ATES communication model (Table 2.5) defines ATES class 3 areas as being exposed to multiple avalanche paths and starting zones. The description already includes all CAT categories.

Sykes et al. (2024) computed the lowest accuracy for ATES class 2, similar to this analysis. They attributed the underprediction to autoATES classifying more forested areas as class 1, while the benchmark maps indicated class 2. Comparing autoATES with CAT, ATES class 2 is assigned to large areas not classified as

avalanche prone in the CAT map indicating overprediction. Particularly in valley bottoms, areas are classified as ATES class 2, although the area above is mostly assigned to class 1. CAT does not classify these areas (see section 4.2.1). The avalanche simulation tool Flow-Py does not consider forest, in the final step the autoATES classifier reclassifies forested raster cells to a lower class. Only forested areas are classified as less exposed. Not forested areas, which should be classified as less exposed due to the influence of forested areas, are still classified as higher classes. Areas below forests are often assigned to a higher class, indicating higher exposure to avalanches, than areas in the forest, although avalanches below the forest are unlikely (Hesselbach 2023).

4.3 Comparison of the model chain modules

Despite differing outputs, autoATES and CAT share similar intermediate steps, computing potential release areas and simulating avalanche runout using different tools. To estimate avalanche runout, autoATES relies on Avaframe's conceptual simulation tool com4FlowPy (see section 2.5.1), physically-based RAMMS::EXTENDED is used for CAT (see 2.5.2). The results of each simulation tool depend on the parameterisation. For the autoATES and the CAT workflow, parameterisations are used aiming at simulating avalanches of size class 3. In the following, we only compare the simulation results with these paramaterisations. Modified parameters would lead in different comparison results.

4.3.1 Comparison of Potential Release Area results

Before comparing the runout results, we first assess the potential release area (PRA) outputs. These from the basis for the runout simulation and are included in the runout results.

For autoATES, PRAs are generated using the algorithm developed by Veitinger et al. (2016) and Sharp (2018). These PRA results serve as input data for the Flow-Py runout simulation and are included in the autoATES classifier.

The CAT PRA data is extracted from the CAT map. The PRAs represented in the CAT map are not the input for the avalanche simulation (Harvey et al. 2018), as the input consists of polygons derived using the algorithm of Bühler et al. (2018). Nevertheless, we analyse the PRAs extracted from CAT layer. The format of both analysed PRA data is a raster layer with raster cells indicated as PRA.

Table 4.5: Area and percentage agreement (of pixel cells) comparing the binary PRA data resulting from the autoATES model chain and from the CAT map. The results are displayed for each test area. Values indicating agreement between categories are highlighted in bold.

	Sellrain		**Davos**	
CAT	**no PRA**	**PRA**	**no PRA**	**PRA**
ATES				
no PRA [km²]	**51**	10	**413**	26
	83%	17%	**94%**	6%
PRA [km²]	5	**35**	26	**133**
	13%	**87%**	16%	**84%**

Table 4.5 shows the agreement between the PRA results obtained from the autoATES model chain and the CAT layer. In Sellrain, 83% of the area designated as ATES-PRA is covered by PRAs in CAT. In Davos, the agreement increases to 94%, indicating that CAT identifies PRAs in 94% of the areas classified as by autoATES.

4.3.2 Comparison of runout results

Avalanche mobility is a key component of both the autoATES and CAT model chains. The results of these mobility simulations influence the ATES classification (see section 2.6.1) and are directly represented in CAT maps (see section 2.3.2).

In the subsequent analysis, we compare runout results from each method. As introduced in section 4.3, we compare the simulation results with the parameterisations used for the autoATES and CAT workflow. In the following, 'ATES or Flow-Py runout' refers to the avalanche path simulated by Flow-Py with the parameterisation employed in the autoATES workflow and 'CAT or RAMMS runout' means the avalanche simulated by RAMMS::EXTENDED with the parameterisation used for the CAT workflow. The runout is treated binary: Each grid cell is either considered to belong to the runout zone or not. We do not distinguish between transition zone and runout zone here. If not otherwise mentioned, 'runout' refers to the entire avalanche path in the following. The ATES runout is generated by Flow-Py simulation. All cells with non-zero values of flux in the simulation results are considered as part of the runout, including PRAs. The CAT runout is derived from the provided CAT maps, where cells, assigned to potential release areas, remote triggering zones or the maximal runout, are counted as runout cells. In a

further analysis, we extract cells classified as PRAs from the runout data.

Table 4.6: Comparison of Flow-Py (autoATES) and RAMMS::EXTENDED (CAT) runout data. The area and percentage agreement of runout area is shown when including and excluding PRA. The bold values represent the agreeing values of the runout results.

		Sellrain		**Davos**
CAT	**no runout**	**runout**	**no runout**	**runout**
ATES				
runout data including PRA				
no runout [km²]	**11**	4	**176**	21
	74%	26%	**89%**	11%
runout [km²]	28	**58**	144	**257**
	32%	**68%**	36%	**64%**
runout data excluding PRA				
no runout [km²]	**52**	1	**335**	13
	97%	3%	**96%**	4%
runout [km²]	32	**16**	145	**106**
	66%	**34%**	58%	**42%**

Table 4.6 demonstrates the agreement between the runout results of the autoATES and CAT model chains. There is a high agreement in non-runout cells between ATES and CAT. When including PRAs in the runout assessment, 74% of the area assigned as non-runout in ATES matches the non-runout cells by CAT in Sellrain. In Davos this agreement is even higher with 89%. Excluding PRAs, these agreement values increase to 97% in Sellrain and 96% in Davos.

Contrarily, the agreement between ATES and CAT is low for cells indicated as avalanche runout. When excluding PRAs, less than 50% of the ATES runout area is assigned to CAT runout area. Including PRAs, these agreement values are 68% in Sellrain and 64% in Davos. For this interpretation the ATES runout serves as the reference data.

Alternatively, when using CAT runout as reference data, the agreement for runout cells improves. Both algorithms agree in 16 km² considering runout areas in Sellrain, only 1 km² is classified as non-runout by ATES but as runout by CAT.

In total, Flow-Py identifies 48 km² as runout area (excluding PRA) in Sellrain and 251 km² in Davos. The CAT map indicates 17 km² and 119 km² as runout zones,

respectively. Of these runout areas, 16 km² and 106 km² align spatially between the two methods. The runout area assigned by ATES is larger compared to CAT.

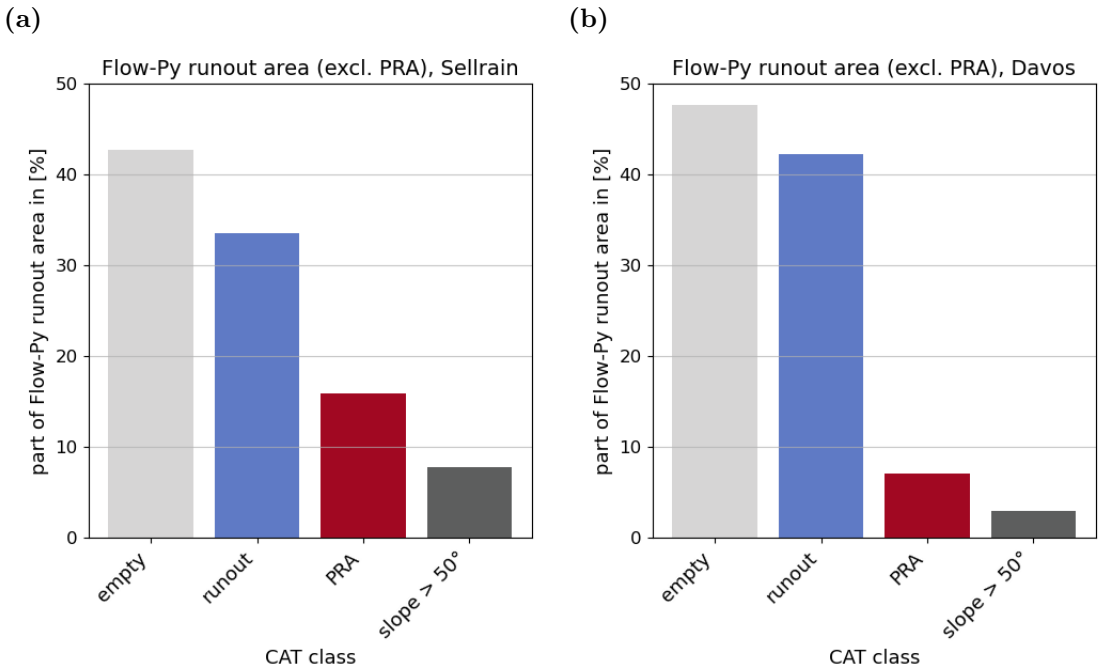

Figure 4.8: The percentage distribution of CAT classes in areas, where Flow-Py assigns avalanche runout (excluding PRAs), is shown for (a) Sellrain and (b) Davos. The CAT classes are 'no classification', runout (max. runout, runout zones with very low, low, medium, high potential), PRA (Release areas with very low, low, medium and high potential) and 'slope steeper than 50°'.

To investigate differences between the two runout results, we analyse the CAT categories in cells, where Flow-Py assigns runout areas (Figure 4.8). In more than 40% of these runout areas, CAT does not classify to any category (no PRA, no runout or slope steeper than 50°). Given the high correspondence of PRAs between both algorithms, it is evident that Flow-Py tends to simulate avalanches with longer runout lengths than RAMMS.

Refering to the second research question: '*How do the model chain modules of autoATES and CAT compare: potential release areas and avalanche runout?*' we figured out that the PRA results of the workflows agree well, while the runout results differ according to runout lengths. Tendency, Flow-Py simulations result in longer avalanches than RAMMS::EXTENDED.

One possible explanation could be the different treatment of forest by each

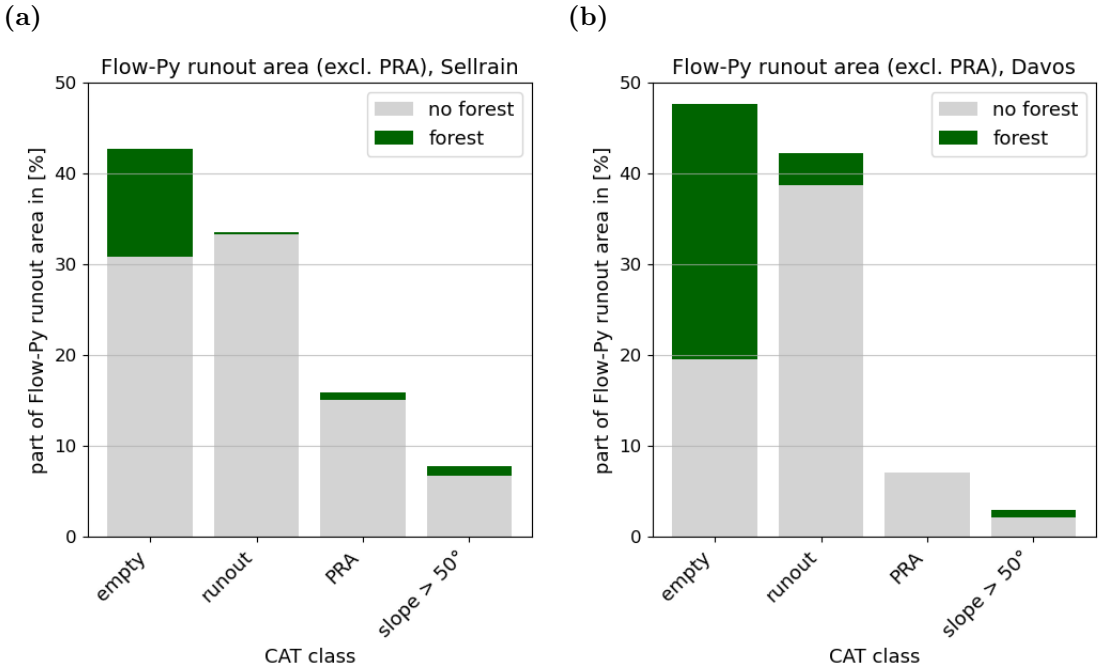

Figure 4.9: as Figure 4.8 including forest information: the colour of the bar marks the part, which is in covered by forest (green) and no forest (grey).

avalanche simulation model. Figure 4.9 shows the proportion of forest within the CAT classes. The forest data is derived from the binary forest layer used to generate the CAT map (see section 3.2.2). 28% (Davos) and 12% (Sellrain) of the area, which is assigned as ATES runout, is not classified in CAT maps and covered by forest. Flow-Py does not consider forestation. RAMMS::EXTENDED on the other side considers forest by increased friction parameters, resulting in an earlier stop of the avalanche in forests (Feistl et al. 2014). So, these forested regions are likely simulated as runout by Flow-Py due to missing consideration of forest effects. However, 31% (Sellrain) and 19% (Davos) of the Flow-Py runout area is not classified as avalanche prone in the CAT map and can not be explained by the presence of forest.

Flow-Py simulates avalanches using the Coulomb friction model (D'Amboise et al. 2022b), meaning that the friction force F_{fric} is expressed by

$$F_{fric} = \mu * \boldsymbol{N} = \tan(\alpha) * \boldsymbol{N}, \tag{4.1}$$

with runout angle α, and the normal component of the gravity force $\boldsymbol{N}$ (Bartelt et al. 1999; Salm 2004).

In contrast, RAMMS is based on Voellmy friction model (Christen et al. 2010) adding a turbulent term to the Coulomb dry-friction term:

$$F_{fric} = \mu * \boldsymbol{N} + \frac{g}{\xi} * \rho * u^2, \tag{4.2}$$

the turbulent term is computed with the gravitational acceleration g, density ρ, average velocity u and a turbulent friction parameter ξ (Voellmy 1955; Salm 2004). The friction parameters μ and ξ are dependent on snow properties. The addition of the turbulent term to the Coulomb friction term in the Voellmy model increases the friction force compared to the Coulomb model. Consequently, velocities and runout lengths are reduced in the Voellmy model. This could lead to the longer runout lengths simulated by Flow-Py compared to RAMMS::EXTENDED results.

The longer runout lengths simulated by Flow-Py in comparison to RAMMS::EXTENDED can result in higher ATES classes compared to CAT classes (cf. section 4.2.2).

Furthermore, the avalanche simulation results are based on parameter configurations. Even slight modifications to the input parameter can lead to different simulation results, thereby affecting the comparison results.

4.4 Adaptation and extension of the autoATES model chain

The open-source autoATES model chain allows extensions and adaptations. Motivated by the results of the qualitative analysis and comparison of ATES maps, in particular the unexpected high classes in the valley bottom, we implement forest interaction in the autoATES workflow. For a more detailed analysis of the mobility results of Flow-Py, we extended the simulation tool to classify the size of each simulated avalanche path according to various international avalanche size classification schemes. Additionally, we use the statistical analyses of the size of all avalanche paths within a region to compare the terrain of the two study areas regarding the destructive potential of avalanches.

4.4.1 Implementation of forest interaction in autoATES

In the previous sections we generated the ATES map using the methodology described by Hesselbach (2023), who adapted the parameters of the autoATES workflow to a test region in Sellrain. Hesselbach (2023) figured out a problem in the treatment of forest. The avalanche simulation tool Flow-Py does not consider forested terrain. In the final step of the workflow, the autoATES classifier

reclassifies forested raster cells to a lower class despite present avalanche runout (see section 2.6.1). However, only forested areas are classified as less exposed, not-forested areas that should logically be classified as less exposed due to the protective influence of forested terrain remain assigned to higher classes. As a result, areas below forests are often assigned to a higher class, as more exposed to avalanches, than areas above, although the probability of avalanches in the former is lower (Hesselbach 2023; Huber et al. 2023).

To fix this overrepresentation, a layer containing the interaction of avalanches with forest is computed with Flow-Py and implemented in the autoATES classifier as described in section 3.3.3. The following section assesses the modified ATES maps that include this forest interaction layer.

Qualitative assessment of ATES

The current ATES map shows unexpected ATES classes in areas at the valley bottom, particularly below the tree line (cf. Figure 4.11, top). Haggen (a village in the Sellrain valley) is assigned to ATES classes 2 (blue) and 3 (red), although areas above are classified as 'simple' (class 1, green) due to forested area (see Figure 4.10). The forest interaction layer is represented in Figure 4.10 in blue, the resulting ATES map after implementing forest interaction in Figure 4.11 (bottom). The ATES map including the forest interaction layer classifies the areas below the 'simple' forested regions as 'simple' (green) instead of 'challenging' (blue) and a small part as 'challenging' (blue) instead of 'complex' (red), compared to the ATES map without the forest interaction layer (Figure 4.11, top).

In section 4.2.1 we figure out that around Jakobshorn, particularly in the valley bottom, the terrain is assigned to ATES classes 2 and 3, although the areas above are classified as class 1. In the top panel of Figure 4.13 the current ATES map is represented. Figure 4.12 illustrates forested areas and the computed forest interaction layer. It illustrates that most areas classified as ATES class 1 are forested and reclassified to a lower class by the autoATES classifier. The classifier does not consider the forest in areas below the avalanche decelerates due to forest interaction resulting in ATES classes 2 and 3 in the valley bottom.

In the ATES map at the bottom in Figure 4.13 the autoATES workflow includes forest interaction. The ATES classification changed to ATES classes 1 and 2 in the described areas in the valley bottom. The autoATES classifier also reclassifies areas where avalanches interacted with forest to lower classes.

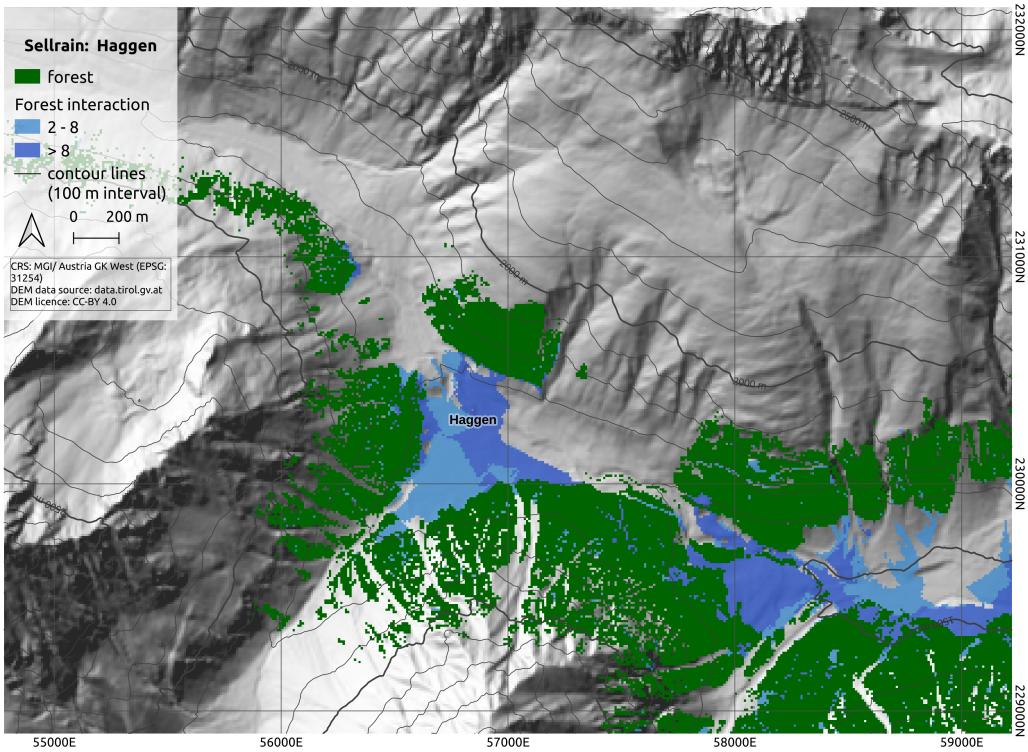

Figure 4.10: The binary forest layer (green) as overlay above the forest interaction layer (blue), resulting from Flow-Py simulation in a small extent around Haggen in Sellrain. Forested areas are indicated in green. The forest interaction layer represents the minimum amount of forested raster cells an avalanche passed previously. In light blue areas (forest interaction is between 2 and 8), avalanches ran through at least 20 – 80 m forest. In dark blue areas (forest interaction is higher than 8), avalanches ran through more than 80 m forest.

Quantitative assessment of ATES

Figures 4.14 and 4.15 show the distribution of ATES classes dependent on the four merged CAT classes as delineated in variant 1 (see section 4.2.3). The histograms contain the autoATES results, both without including the interaction between avalanches and forest and with including forest interaction.

The four ATES classes should correspond to the four CAT classes, respectively. Raster cells assigned to CAT class 1 (no classification) should be classified as ATES class 1. Without including forest interaction in the autoATES workflow, 14.6 km^2 of unclassified areas in CAT maps are classified as ATES class 1 (simple) in Sellrain. This area increases by 1.9 km^2 (13%) when including forest interaction in autoATES. In Davos, the area, which is not classified as avalanche prone in the CAT map and assigned to class 1 in ATES map increases by 7% from

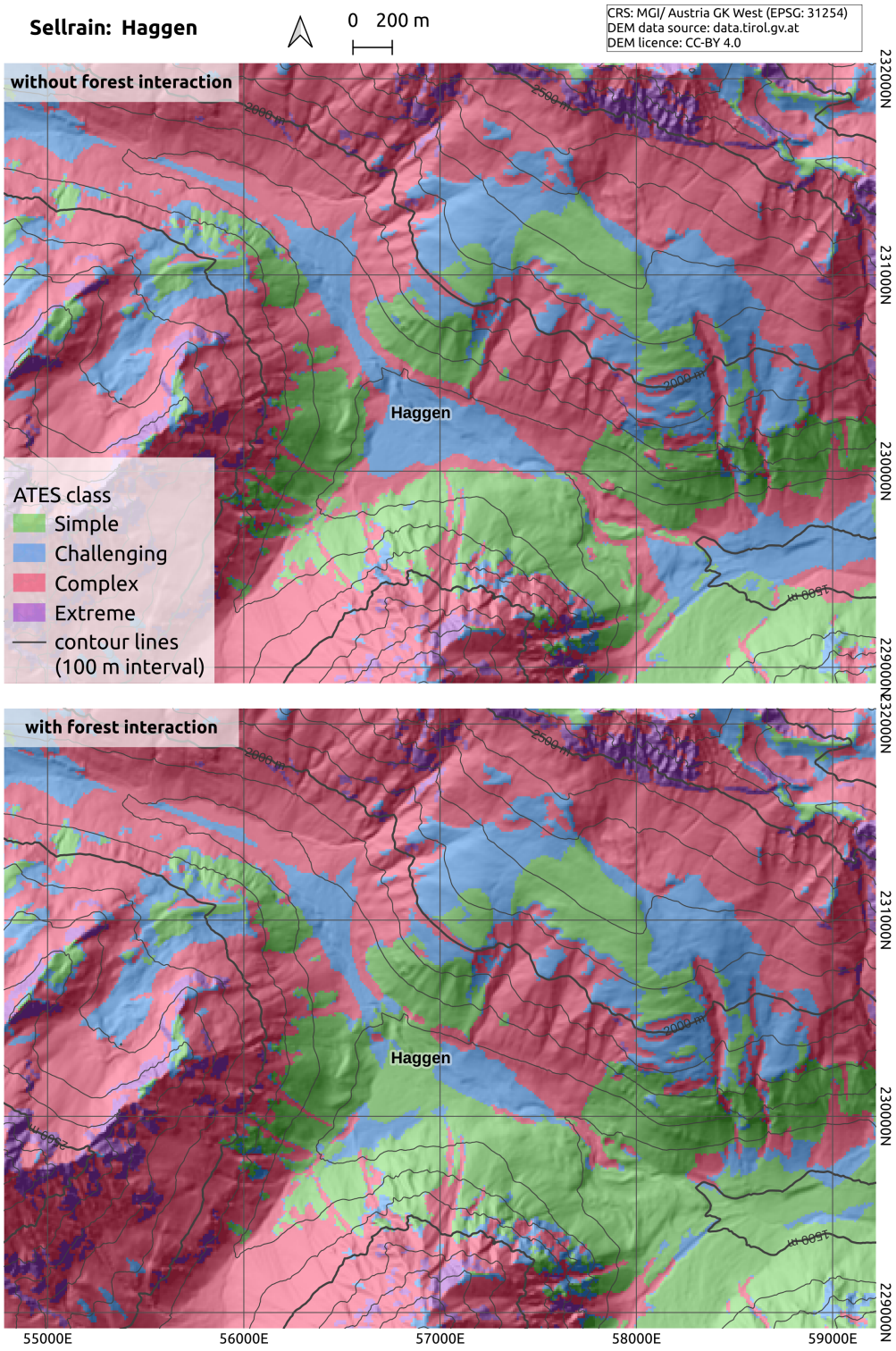

Figure 4.11: ATES maps computed without (top) and with (bottom) a forest interaction layer, applied to a small extent around Haggen in Sellrain. The maps classify the terrain into the four ATES classes 'simple' (green), 'challenging' (blue), 'complex' (red) and 'extreme' (purple).

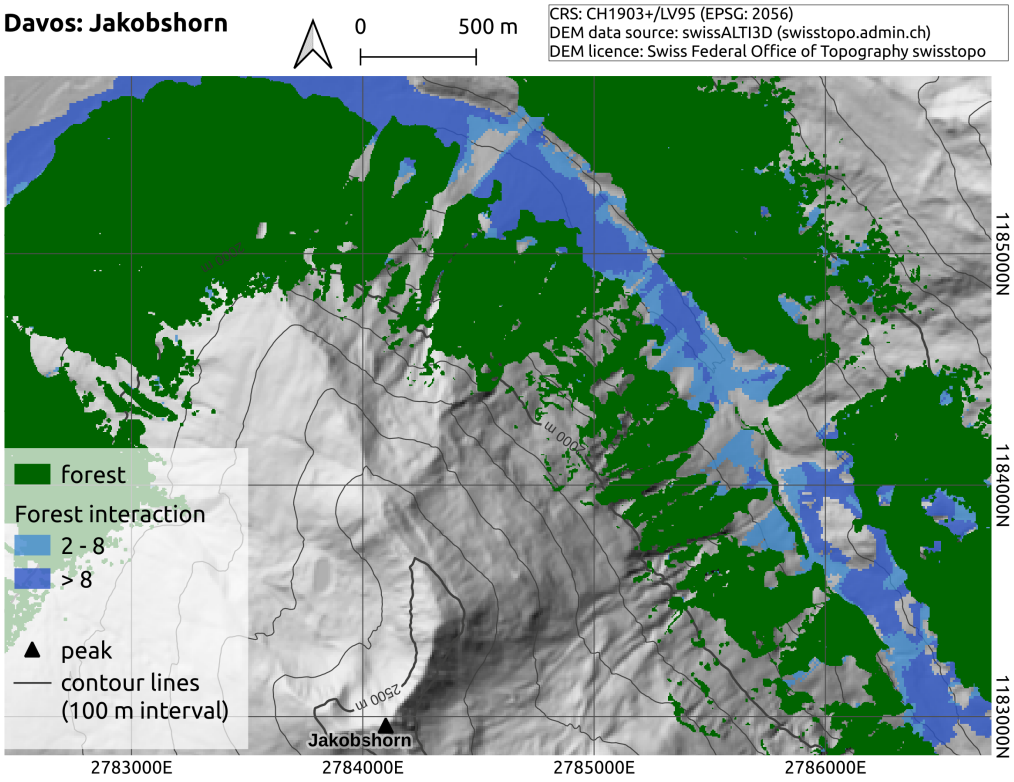

Figure 4.12: As in Figure 4.10 for an extent around Jakobshorn in Davos

239.9 km² (without forest interaction) to 258.4 km² by implementing forest interaction. Areas assigned to ATES classes 2 (challenging) and 3 (complex) decrease.

In Davos, the ATES class distribution for CAT class 2 also changed. In areas, where CAT classifies a very low, low and medium remote triggering potential, the area assigned to ATES class 2 increases by 1% from 42.1 km² to 42.6 km² when including forest interaction. Areas classified as ATES class 1 also increase from 10.1 km² to 11.8 km². This shows a slight improvement of the ATES class distribution, especially in Davos, where a larger area is forested (cf. section 3.1).

Table 4.7 shows the statistical metrics - accuracy, precision, recall and F-score - calculated between the ATES results and the merged CAT classes for the three variants (see section 4.2.3), considering the implementation of forest interaction in the autoATES workflow. The values of all metrics are higher when forest interaction is implemented, indicating an improved agreement between autoATES and CAT with forest interaction regarding the four classes. The improvement is more pronounced in Davos than in Sellrain.

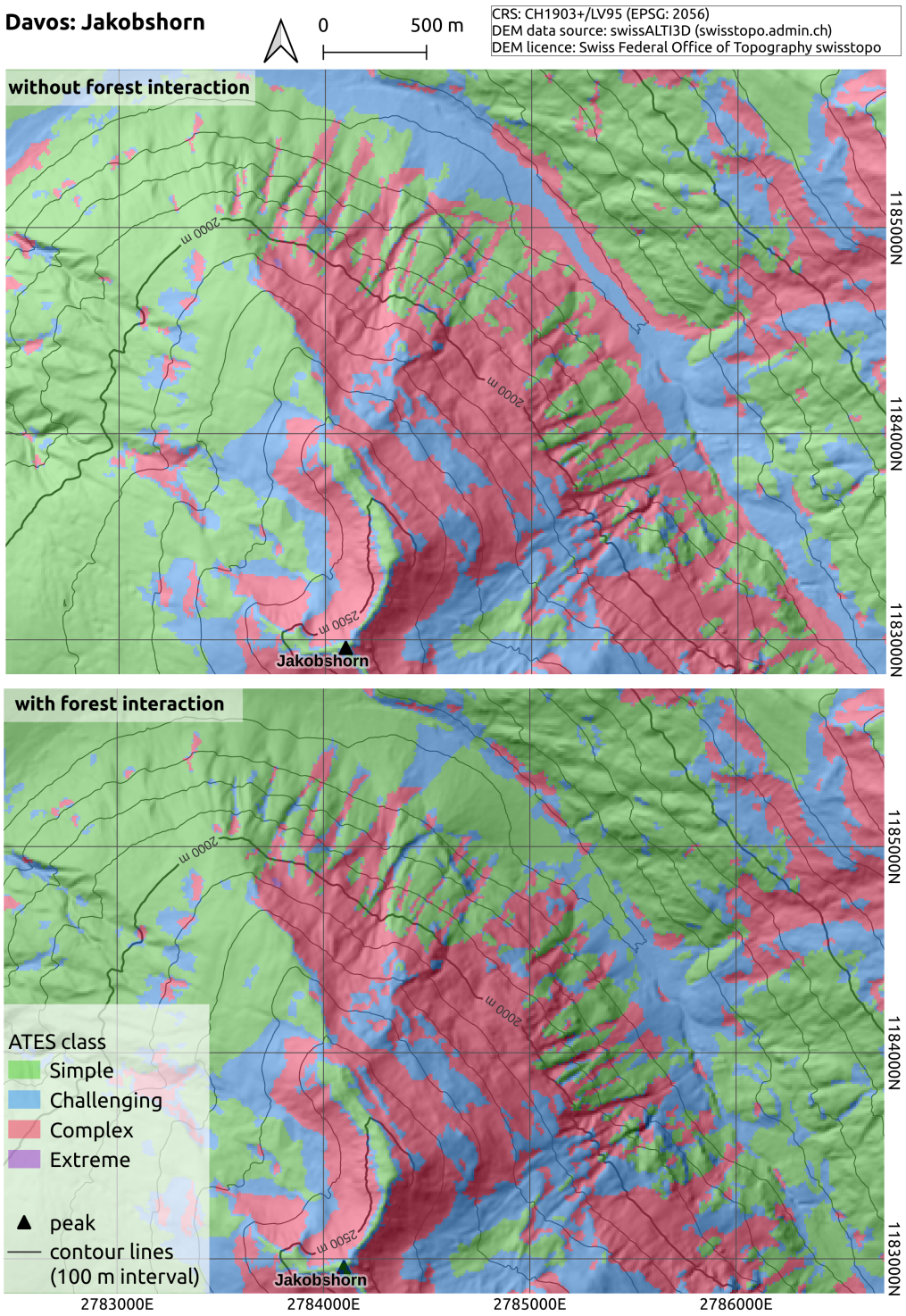

Figure 4.13: ATES maps computed without (top) and with (bottom) a forest interaction layer, applied to a small extent around Jakobshorn in Davos. The maps classify the terrain into the four ATES classes 'simple' (green), 'challenging' (blue), 'complex' (red) and 'extreme' (purple).

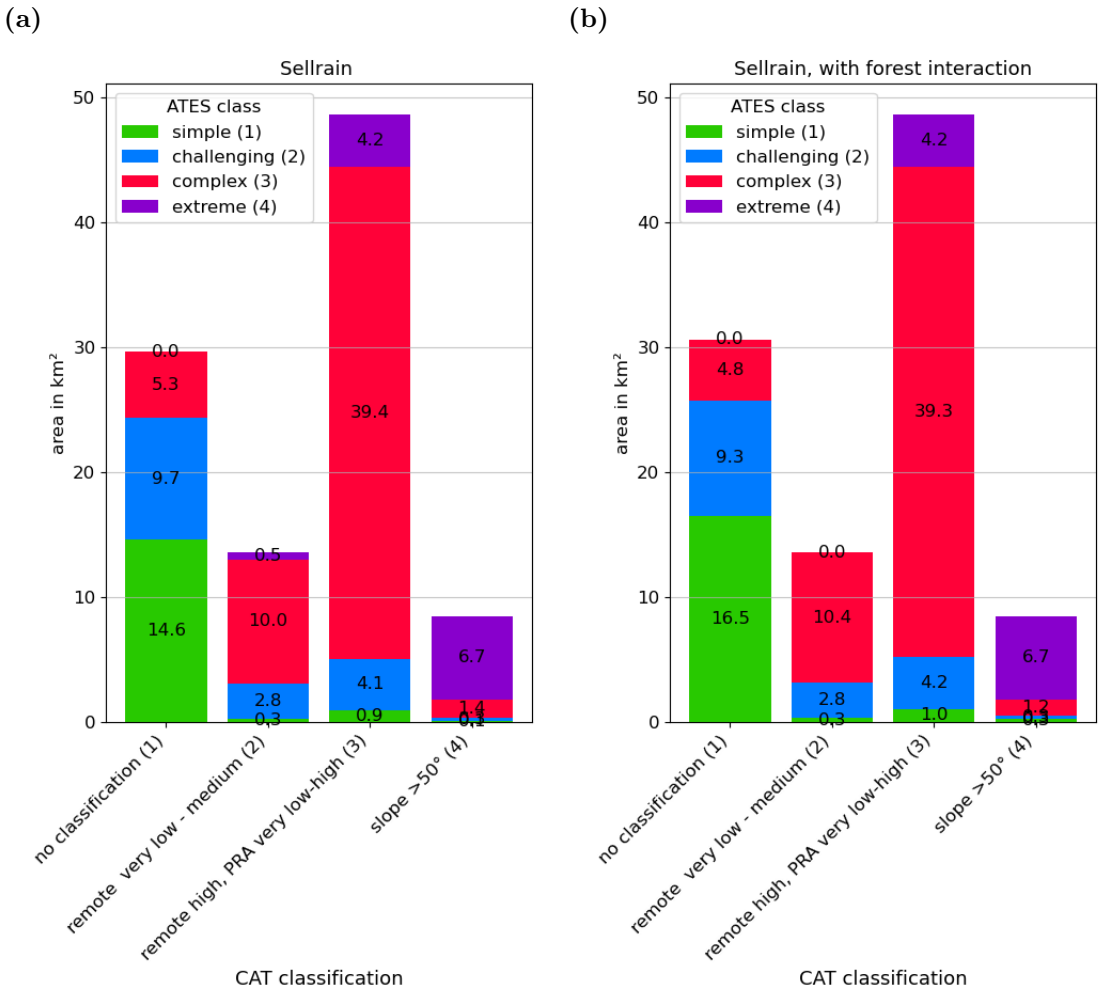

Figure 4.14: The CAT categories are merged into four categories: 1) no classification, 2) potential of remote triggering: very low, low, medium, 3) potential of remote triggering: high, potential of release area: very low, low, medium, high, 4) slope steeper than 50°. The spatial distribution of the ATES classes ('simple' in green, 'challenging' in blue, 'complex' in red, 'extreme' in violet) is shown dependent on these merged CAT classifications for Sellrain in (a) excluding forest interaction, and in (b) including forest interaction. The numbers in the bars describe the area in km² assigned to the ATES and CAT class, respectively.

Improvement of autoATES

Refering to the third research question '*Can we improve ATES maps with an adapted autoATES workflow including forest interaction?*': In ATES maps, that include the interaction between avalanches and forest, a qualitative improvement is visible. Particularly in valley bottoms, areas below forested regions are classified as lower classes reflecting reduced exposure to avalanches due to the protective effects of the overlying forest.

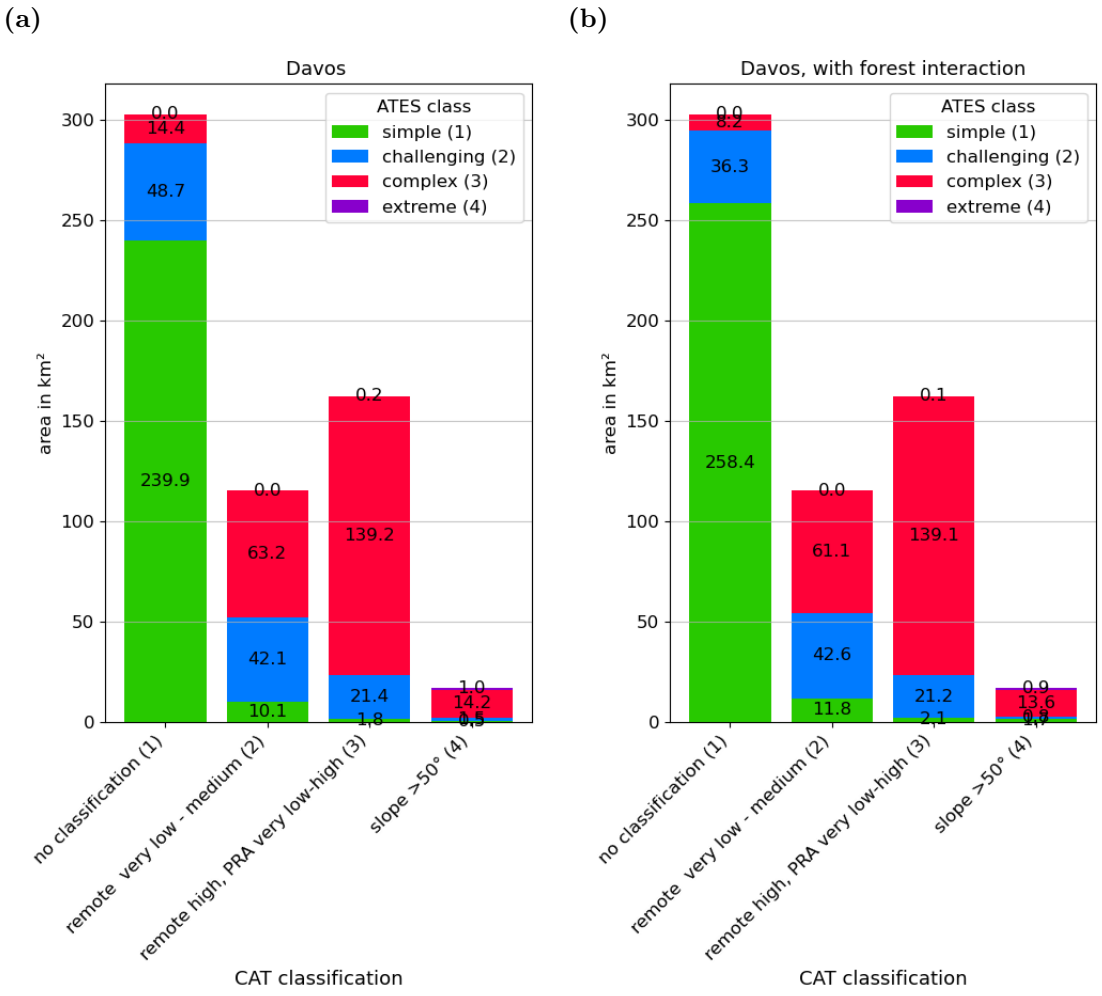

Figure 4.15: As in Figure 4.14 for the test region Davos.

The implementation of forest interaction into autoATES affects the comparison between ATES and CAT. Since CAT considers this protective effect of forests due to inclusion of forest in the avalanche simulation tool RAMMS:EXTENDED, the agreement of ATES and CAT slightly improves, leading to higher accuracy and F-score metrics. Especially, ATES classes 1 and 2 align more closely with corresponding merged CAT classes.

This implementation method in autoATES does not directly affect the avalanche path. Each path tracks and stores the number of cells intersecting with forest as an additional variable. The autoATES classifier adjusts ATES classes according to this new forest interaction layer. This is a first approach to compute the forest interaction with Flow-Py and implement this into the autoATES classifier. Further analyses are necessary, especially to determine thresholds for the reclassification.

Table 4.7: Statistical metrics for the three variants of merged CAT classes mentioned in section 4.2.3 to assess the agreement of the four merged CAT classes and the four ATES classes. Accuracy, precision, recall and F-score are given in % for test regions Sellrain and Davos when including (incl) and excluding (excl) forest interaction.

		Sellrain				Davos			
variant	**forest**	**accuracy**	**precision**	**recall**	**F-score**	**accuracy**	**precision**	**recall**	**F-score**
1	**excl**	63	66	63	64	71	73	71	72
	incl	64	66	64	65	74	77	74	75
2	**excl**	69	64	69	66	72	72	72	72
	incl	70	65	70	67	76	76	76	76
3	**excl**	61	65	61	63	70	73	70	72
	incl	62	65	62	63	73	77	73	75

Furthermore, a more realistic implementation of avalanche deceleration in forested terrain could involve a categorized forest layer instead of a binary forest layer, since forest structure characterized by stem density, canopy cover, species and forest gaps affect avalanche dynamics (D'Amboise et al. 2022a).

Toft et al. (2023) and Sykes et al. (2024) used the 'forest_detrainment'-branch of the Flow-Py repository (Neuhauser et al. 2021) to consider snow detrainment and adjusted friction in forested areas. There are various methods including effects of forests in avalanche simulation models, for example provided by Teich et al. (2012), Feistl et al. (2014) and D'Amboise et al. (2022a). An important factor for including the forest interaction into avalanche simulation models is the quality of forest data. In the Sellrain test region the binary forest layer is derived by an empirically determined threshold. Enhancing the data quality entails further analyses to determine the optimal threshold. The forest density data obtained with the method used in this thesis (see section 3.2.2) may include artifacts in addition to actual forested areas. However, utilizing DSM and DTM data, which are typically available for most regions, enables the computation of forest density over a large geographical area.

4.4.2 Size classification of simulated avalanche paths with Flow-Py

Motivated by the divergence of runout results within the autoATES and CAT model chains, we extended the autoATES module Flow-Py to assess the simulated avalanche paths in more detail. Although we select Flow-Py input parameters to simulate medium to large avalanches (Hesselbach 2023), the size of the simulated avalanches can vary considerably.

In this section, we analyse all simulated avalanche paths (with the parameterisation used for the autoATES workflow; see section 3.3.1) according to different avalanche size classification schemes after EAWS (2023), CAA (2016) and Bühler et al. (2019). Specifically, we examine the parameters runout length (E_{rl}), impact pressure (C_{ip}) and affected area (B_{aa}). Bühler et al. (2019) and EAWS (2023) indicate ranges of values for categorising the size of simulated paths, while CAA (2016) provide single values. To define a range for classification, the provided values are considered as the midpoint of each class range, similar as Hesselbach (2023) classified the avalanche size based on impact pressure C_{ip}.

Figure 4.16a shows the distribution of runout lengths of all paths in both test regions, with the background colours representing the avalanche size classes classified by EAWS (2023) using runout length. Red colours (classes 4 and 5) delineate the range, where paths exhibit longer runouts than intended, while blue indicates the aimed sizes 2 and 3 and green the size 1. In Sellrain and Davos, the quartiles fall within the range of avalanche size 2 and 3; however, more than 10% of paths extend into classes 4 and 5 due to their runout lengths (E_{rl}). Some runout lengths exceed 2 000 m, classified as very large avalanches.

Since Flow-Py is based on the alpha-angle-concept (see section 2.5.1) and simulates avalanches for an alpha angle of 26° within the chosen parameterisation, the runout length depends on terrain characteristics. Due to the fixed alpha angle of 26°, the runout angle calculated between the horizontal and the line through the release and deposition points remains 26° for all simulated paths. However, this calculated runout angle may exceed the alpha angle, if the flow stopped through the R_{Stop} criterion. Figure 4.17 illustrates that the majority of the runout angles are 26°. The outliers, characterised by large runout angles, belong to avalanche paths that would extend beyond the boundaries of the test regions resulting in the paths being cut off at the edge of the region. These runout angles and the corresponding runouts are not representative.

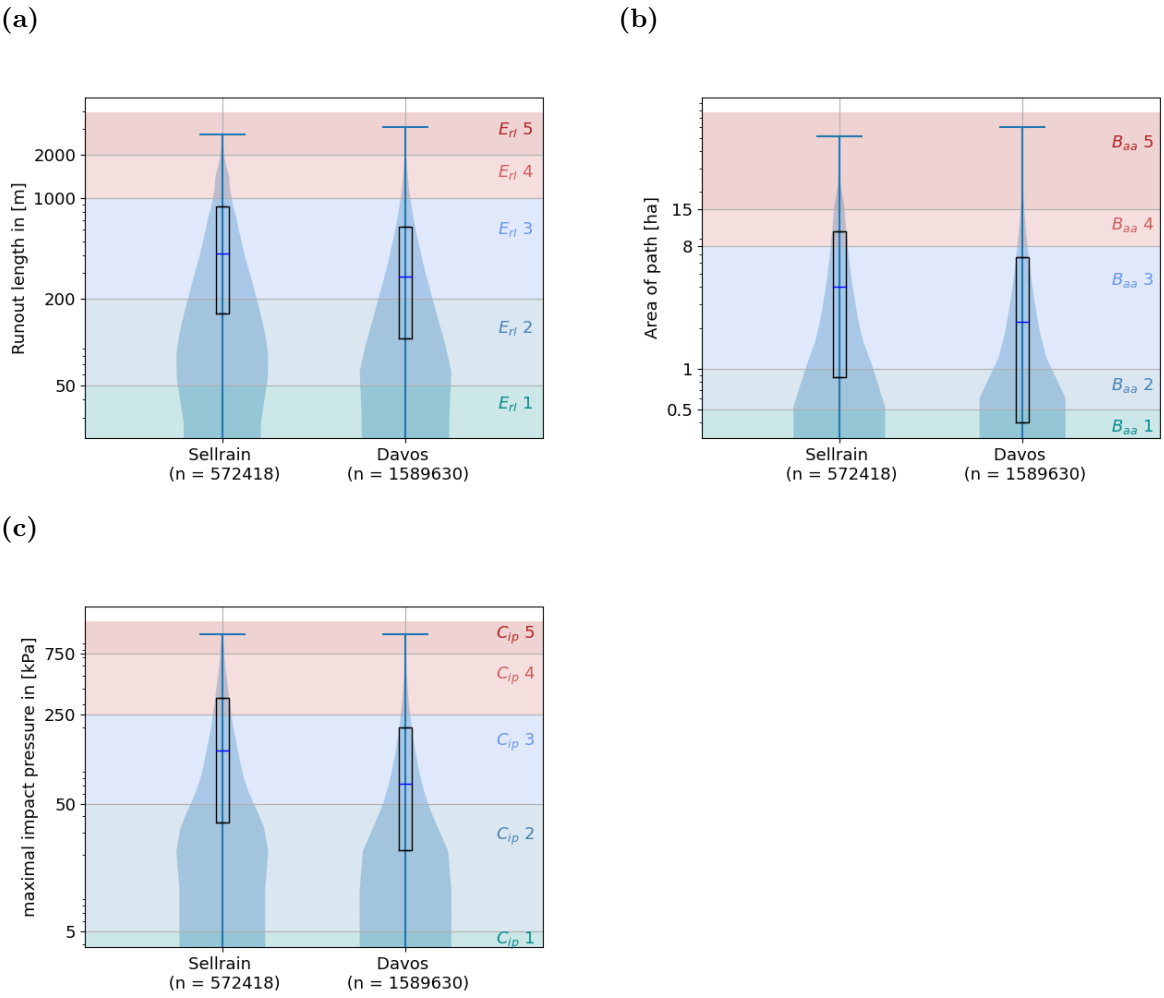

Figure 4.16: Violinplots show the distribution and density of (a) runout length, (b) affected area and (c) maximal impact pressure of all simulated paths with Flow-Py in Sellrain and Davos. The boxplot inside the violinplot marks the median with the blue horizontal line and the quartiles with the box. The underlying data contains 572 418 paths in Sellrain, 1 589 630 paths in Davos. The background is coloured based on the corresponding avalanche size classes according to classification method using the runout length (runout length) after EAWS (2023) (E_{rl}), affected area after Bühler et al. (2019) (B_{aa}) and the impact pressure after CAA (2016) (C_{ip}), respectively. A red background overestimates the avalanche size class (class 4 and 5), blue background marks the range for classes 2 and 3 and green class 1. Note the logarithmic scales.

Figure 4.18 shows an example of an avalanche thalweg with a runout length of 2 000 m. Dependent on the continuous falling terrain along more than 900 m vertically, the avalanche can reach a runout corresponding to avalanches classified as very large (EAWS 2023). Another example (Figure 4.19) shows a Flow-Py simulation with the same input parameters resulting in an avalanche runout length

(a) **(b)**

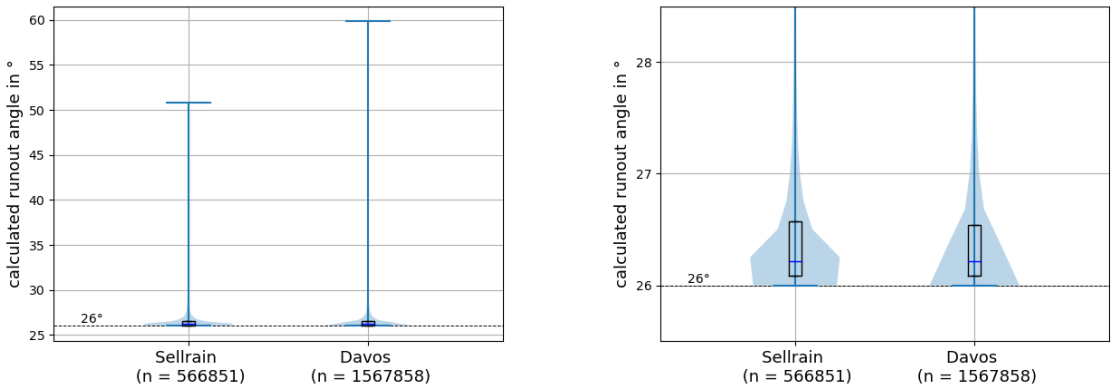

Figure 4.17: Violinplots show the density and distribution of the calculated runout angle between the horizontal and the line through release and deposition points of all paths simulated with Flow-Py in Sellrain (left) and Davos (right). The boxplot inside the violinplot marks the median with the blue horizontal line and the quartiles with the box. The dashed horizontal line represents the 26° level, the value of the alpha angle serving as input parameter in Flow-Py. The underlying data contains 566 851 paths in Sellrain, 1 567 858 paths in Davos. Panel (b) is a zoomed-in representation of angles between 26° and 28°. It differs from panel (a) only in terms of the scale used.

of approximately 450 m, corresponding to a large avalanche size (EAWS 2023). Both examples show a runout angle of approximately 26° between the horizontal and the line through the starting and deposition points, as defined in the Flow-Py input settings. The runout lengths vary due to the different terrain characteristics along the avalanche path.

Figure 4.16b shows the distribution of the affected area, with avalanche size classified using B_{aa} (Bühler et al. 2019). The data contains the area of the individual paths simulated for single PRA raster cells. Affected areas of contiguous PRAs would result in larger path areas. However, in Sellrain, the upper quartile of affected area falls within the range of size 4, signifying that more than 25% of the avalanche paths are classified as very large or extremely large. Similarly, in Davos, approximately 20% of the paths are classified as classes 4 and 5 based on affected area.

The distribution of maximal impact pressure shows a similar behaviour (Figure 4.16c). In Sellrain, the upper quartile (340 kPa) falls in the range of size 4, 25% of the paths are classified as class 4 or 5, in Davos 20%.

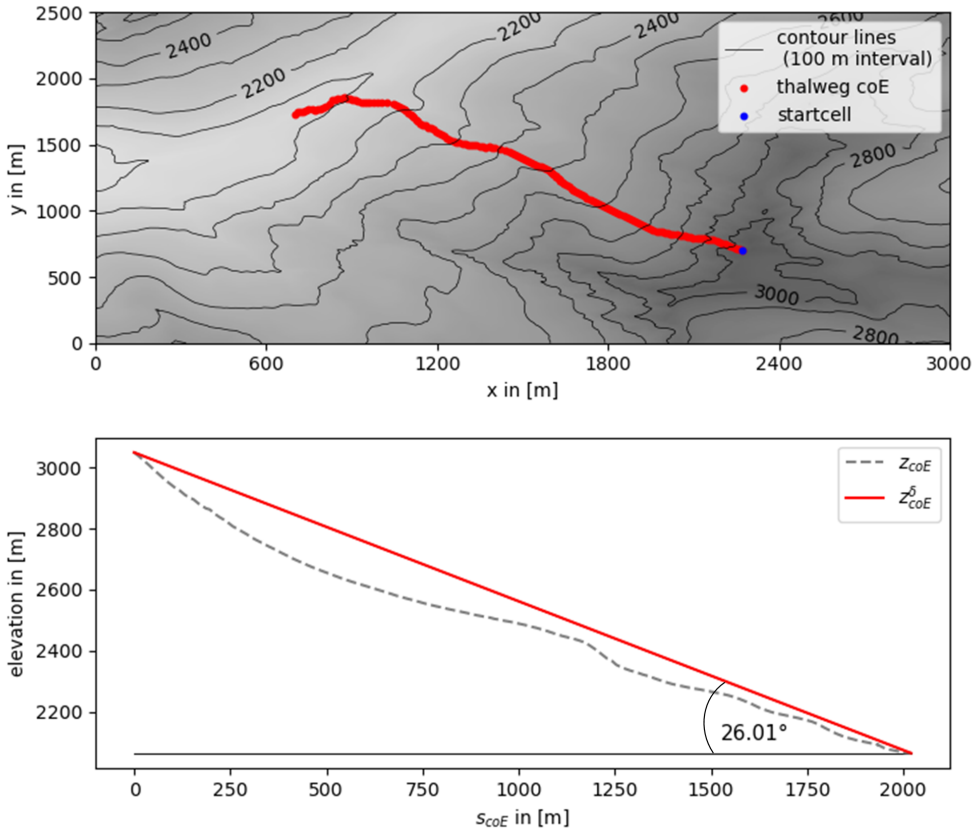

Figure 4.18: The thalweg of a path simulated by Flow-Py with alpha angle 26°. The location of the startcell is represented as blue dot, the thalweg calculated as center of energy (coE) in red dots (top). The background shading and contour lines represent the topography of the surrounding terrain. In the lower panel a two-dimensional representation of the thalweg is shown. The grey dashed line represents the elevation of the topography along the thalweg (z_{coE}). The red line represents z delta along the thalweg (z^{δ}_{coE}). The line through the starting and deposition points (in this case z^{δ}_{coE} in red) and includes an angle of 26° with the horizontal (black). The example is taken from the study area Sellrain.

Small avalanches (size 1) are classified according to all three classification schemes. Depending on terrain conditions, Flow-Py also simulates some small avalanches due to the runout-angle concept.

Following Hesselbach (2023), the Flow-Py input parameter alpha angle is set to 26°. He simulated 100 avalanches with contiguous PRAs corresponding to avalanche size 3 varying the alpha angle. He selected the parameter based on analysing the avalanche size of simulation results using the same avalanche size classification schemes outlined in section 2.2 and applied in Figure 4.16. In his analysis, the results also included avalanches larger than size 3 for the finally used alpha angle of 26°.

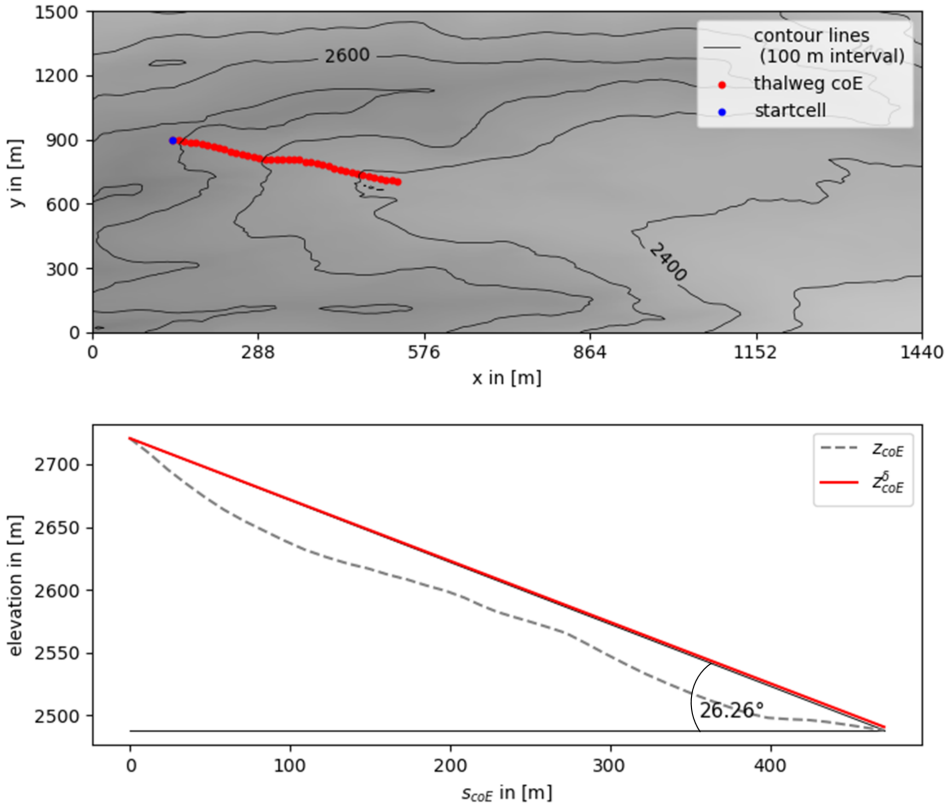

Figure 4.19: As in Figure 4.18 for a different example with a shorter runout length.

To analyse simulated paths larger than size 3, Figure 4.20 represents a subset containing paths classified as avalanche size 4 and 5 based on affected area according to Bühler et al. (2019) (B_{aa}), runout length according to EAWS (2023) (E_{rl}) and impact pressure according to CAA (2016) (C_{ip}), respectively. For paths with a path area larger than 8 ha, consequently classified as size 4 and 5 (B_{aa}), the lower quartiles of the impact pressure fall into avalanche size 4 (C_{ip}). About 75% of the paths classified as size 4 and 5 using affected area are also classified as size 4 and 5 using impact pressure (see Figure 4.20a). Approximately 50% of the same paths fall into avalanche size class 4 and 5 according to runout length (E_{rl}), while the other 50% fall into avalanche size 3 or smaller (Figure 4.20b).

The behaviour is similar for paths classified as size 4 and 5 according to impact pressure (C_{ip}), as shown in Figures 4.20c and 4.20d. Approximately 75% of the paths are also classified as size 4 and 5 using the affected area. About 50% of the paths fall into avalanche size class 4 and 5 using runout length (E_{rl}) and the remaining 50% fall into avalanche size 3 or smaller.

More than 75% of paths classified as avalanche size 4 and 5 based on runout length (E_{rl}) are similarly classified as size 4 and 5 paths according to impact pressure

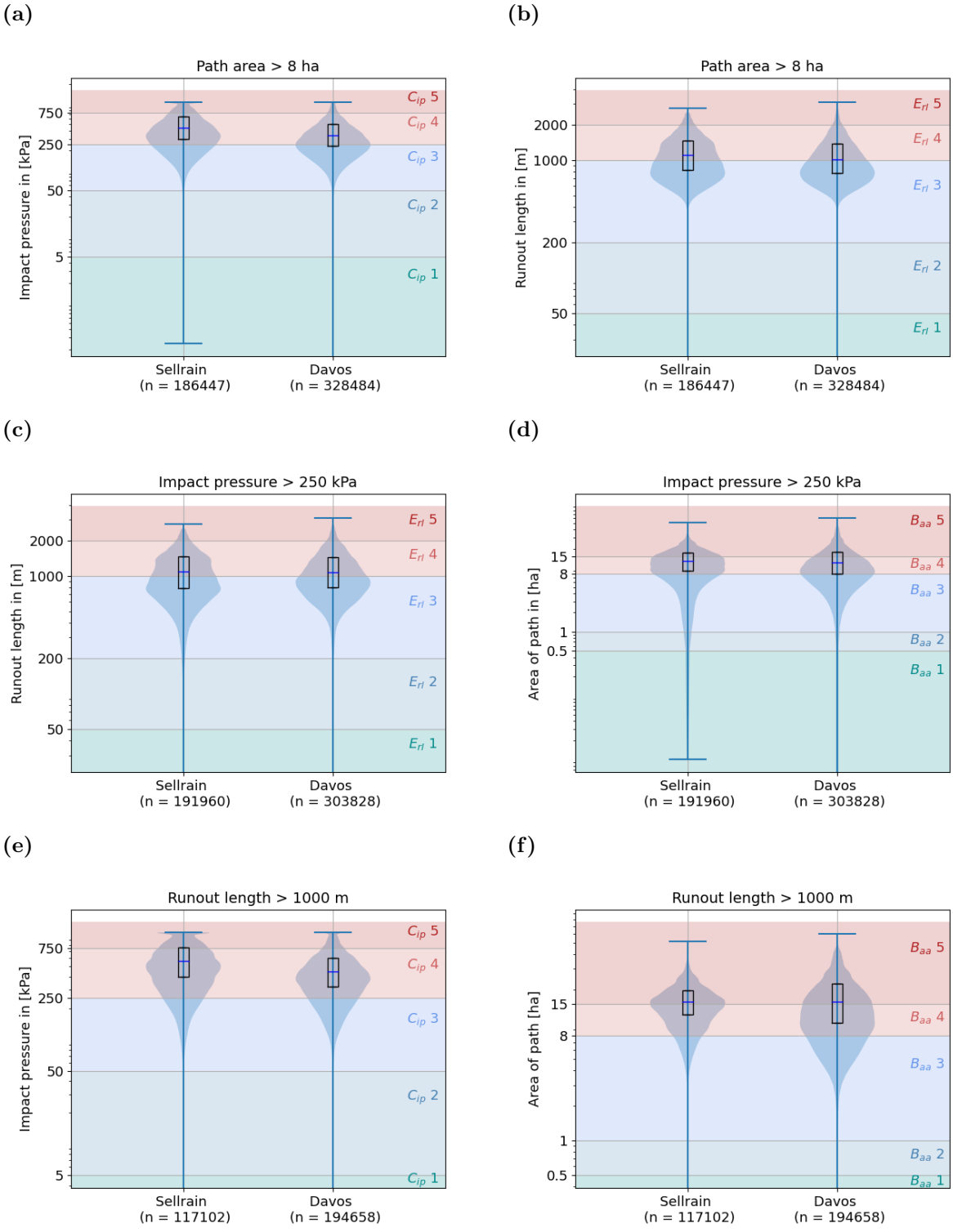

Figure 4.20: As in Figure 4.16. The represented data is a subset of avalanches classified as size 4 and 5 using affected area after Bühler et al. (2019) (B_{aa}) in the top row, by impact pressure after CAA (2016) (C_{ip}) in the mid row and by runout length after EAWS (2023) (E_{rl}) at bottom.

(C_{ip}) and affected area (B_{aa}), as illustrated in Figures 4.20e and 4.20f.

Refering to the fourth research question *'How can we quantify and classify avalanche paths on a regional scale?'*: we extend Flow-Py to receive information about each simulated avalanche path in each study area. We use these results to classify the size of the paths according to various international used avalanche size classification schemes (CAA 2016; Bühler et al. 2019; EAWS 2023).

Figure 4.20 shows that single size classification is insufficient. Avalanches classified as size 4 or 5 based on impact pressure after CAA (2016) can be classified as size 2 or 3 according to runout length after EAWS (2023). Nevertheless, Flow-Py simulates avalanches that are classified as size 4 and 5 considering at least two of the classification methods.

When comparing the classification schemes, more avalanches are classified as size class 2 and 3 according to E_{rl} compared to C_{ip} and B_{aa} that result in more avalanche paths of size 4 and 5.

We analyse paths and thalwegs for each raster cell assigned as a PRA, and not for a maximum avalanche event. This results in the identification of multiple thalwegs, representing trajectories of all possible events. Thalwegs of a larger release area are more frequently observed in these statistical analyses.

4.4.3 Comparison of the study areas according to simulated avalanche paths with Flow-Py

In section 4.1 we figured out a divergent distribution of ATES and CAT classes in the two test regions. We use the size classifications of the simulated avalanche paths (see section 4.4.2) to compare the test regions according to the destructive potential of possible avalanches.

Table 4.8: Area and amount of PRA cells in each test region Sellrain and Davos. PRAs are computed using the algorithm by Veitinger et al. (2016). Each cell has dimensions of 10 m x 10 m.

	Sellrain	**Davos**
Area	150 km²	600 km²
PRA cell amount	572 418	1 589 630
PRA cells per km²	3 844	2 658

Test region Sellrain has an area of approximately 150 km², Davos of 600 km². In Sellrain there are 572 418 cells (10 m x 10 m), that are assigned as PRA, in Davos there are 1 589 630 PRA cells that are computed using the algorithm by Veitinger et al. (2016) (see 2.4.1). In Sellrain the density of PRAs and therefore of avalanche paths is 1.5 times as high as in Davos, but in total the amount of avalanche paths is three times higher in Davos than in Sellrain due to the different area size (see Table 4.8).

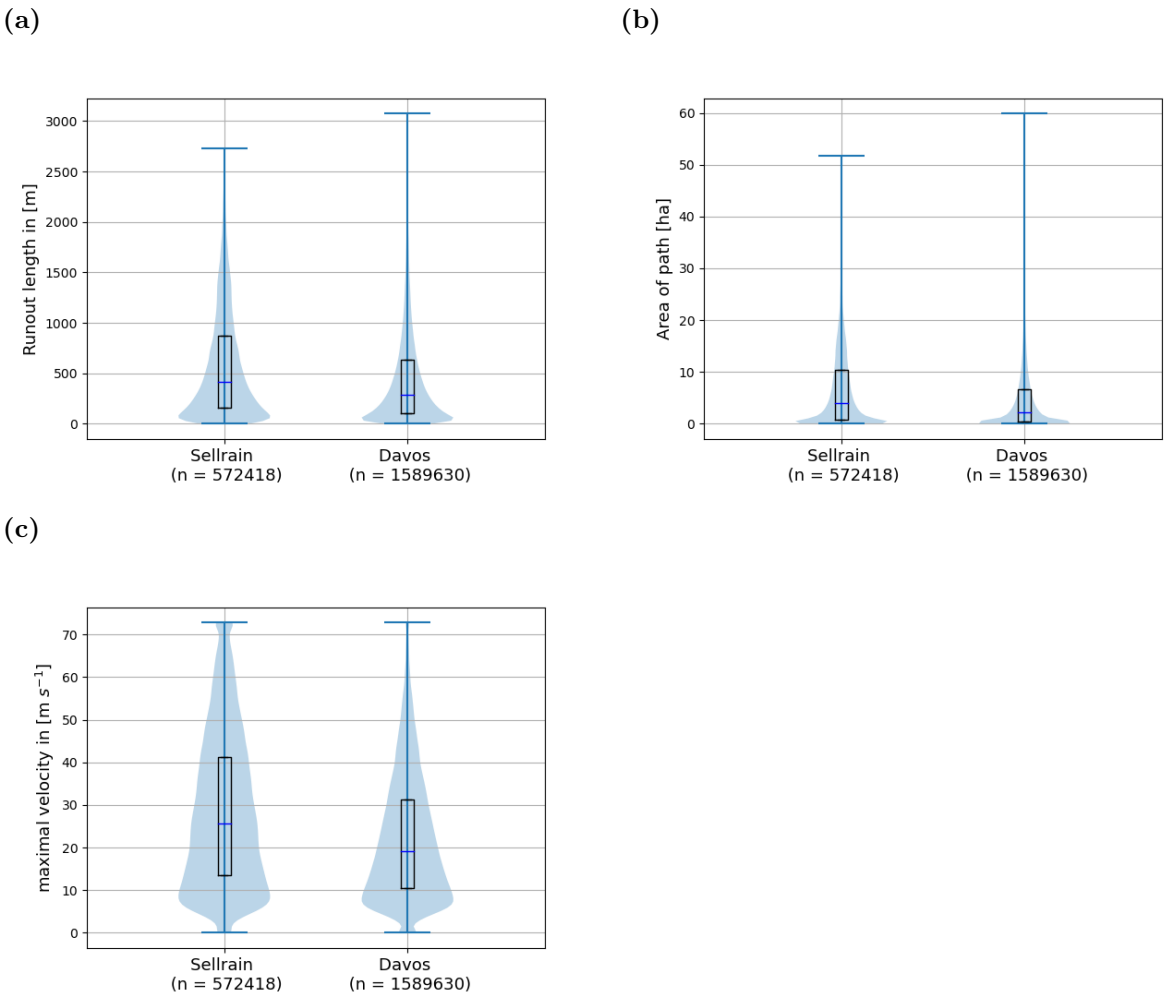

Figure 4.21: Violinplots show the distribution and density of (a) runout length, (b) affected area and (c) maximal velocity of all paths simulated with Flow-Py in Sellrain (left) and Davos (right). The boxplots inside the violinplots mark the median with the blue horizontal line and the quartiles with the box. The underlying data contains 572 418 paths in Sellrain, 1 589 630 paths in Davos.

The majority of paths is shorter in Davos than in Sellrain. In Sellrain, the median of runout length is 411 m, in Davos 284 m. 75% of the paths are shorter than 869 m in Sellrain and 631 m in Davos. Only a few outliers are longer in Davos than in

Sellrain (see Figure 4.21a).

Figure 4.21b shows that the distribution of the affected area of simulated paths is similar to the runout lengths. The median and upper quartile are lower in Davos than in Sellrain. A few outliers are larger in Davos. The majority of paths is larger (according to runout length and area) in Sellrain than in Davos. This is related to their hypsometries (see Figure 3.1). Major areas in Sellrain are situated at a higher elevation with a greater mean slope angle compared to Davos.

The velocity of an avalanche path is related to its impact pressure (see equation (2.7)) and to the destructive potential of the path. The majority of simulated avalanches shows a higher maximum of velocity in Sellrain compared to Davos (Figure 4.21c). More avalanche paths have a higher maximal impact pressure and therefore a higher destructive potential in Sellrain than in Davos.

Refering to the fifth research question *'Do the two test regions exhibit different characteristics according to typical avalanche size through their given terrain characteristics?'* (see chapter 1): The density of PRAs in the test areas, the simulated runout lengths as well as affected path areas and maximal velocities indicate that the terrain characteristics allow more avalanche paths with a higher destructive size in Sellrain than in Davos. This is supported by the distribution of ATES and CAT classes as explained in section 4.1. Sellrain is mostly classified into classes representing higher avalanche exposure compared to Davos. Figure 3.1 emphasizes the differences between the two areas. The majority of the Sellrain test area is situated at a higher elevation than Davos, and it has a lower proportion of forested terrain.

As discussed in section 4.4.2, we analyse paths and thalwegs of all release cells, not of maximum avalanche events.

Chapter 5

Conclusion and Outlook

We compared the avalanche terrain classification methods autoATES and CAT in two Alpine test regions, focusing on their end products and intermediate steps.

ATES and CAT maps are helpful tools for planning professional and recreational trips in avalanche-prone terrain. Each classification method can be created by fully automated workflows, sharing similar chain modules. They involve the computation of PRAs and the simulation the corresponding avalanche runout, requiring only a DTM and a forest layer as input data.
The autoATES workflow contains the following steps:

1. PRA algorithm
   computes PRAs (algorithm developed by Veitinger et al. (2016)).
2. Flow-Py
   simulates avalanche runout.
3. autoATES classifier combines the results with terrain characteristics to ATES classes and maps these.

CAT is generated with these tools:

1. PRA algorithm
   computes PRAs.
2. RAMMS::EXTENDED
   simulates avalanche runout.
3. Statistical tool
   calculates zones, where remote triggering is likely.

The end products contain different categories, since autoATES combines these intermediate results with terrain characteristics to four classes: 'simple', 'challenging', 'complex' and 'extreme', while CAT delineates the PRAs, zones where remote triggering is likely, maximal avalanche runout and very steep terrain. In general,

ATES and CAT maps as well as the results of their intermediate steps represent a specific scenario dependent on parameter selection. Due to its higher resolution and more detailed differentiation of the classes, CAT provides more detailed information and is more related to the represented scenario.

The different types of categories of both end products complicate their comparison. However, ATES class 1 corresponds predominantly with areas that CAT does not classify as avalanche prone terrain, while ATES class 4 closely aligns with terrain assigned as very steep by CAT. ATES classes 2 and 3 contain areas classified across all CAT categories.

Comparing the model chain modules, the focus is on avalanche runout results, since PRA results exhibit high agreement. We figured out that Flow-Py simulations result in longer avalanches compared to RAMMS::EXTENDED, and we propose several hypothetical reasons:

- The avalanche simulation results including the runout length are highly related to the terrain and input parameters. Modifying the parameterisations would result in different simulation. For example, increasing Flow-Py's friction parameter alpha would lead to shorter avalanches.

- The avalanche simulation models are based on different friction models. Flow-Py relies on the Coulomb friction, while RAMMS uses the Voellmy friction model, which includes a turbulent term in addition to Coulomb friction. Additionally, in the RAMMS-parameterisation for the CAT workflow, friction values are used and locally adapted that result in higher friction forces compared to the Flow-Py constant parameterisation in the autoATES workflow.

- RAMMS considers forest in the simulation by modifying friction parameters in forested areas to account for the decelerating effects of trees. In contrast, Flow-Py does not include these effects due to forests. As a result, Flow-Py simulations may result in longer and potentially less realistic avalanches in forested areas compared to RAMMS.

To overcome the absent interaction of avalanches and forest in the ATES maps, we implemented a feature in Flow-Py that counts and stores the number of forested cells an avalanche path passed. The autoATES classifier reclassifies these forest interaction cells to lower ATES classes, reflecting the reduced exposure to avalanches due to protective effects of forested terrain. This implementation into the autoATES workflow results in qualitatively improved ATES maps, particularly below forested areas.

For a more detailed analysis of the simulated avalanche paths with Flow-Py, we implement a feature to store various parameters of all simulated paths and corresponding thalwegs. These results offer data to interpret and evaluate the Flow-Py simulations. We classify the avalanche size according to runout length, impact pressure received from the thalweg and affected path area. The majority of the paths are classified as medium and large avalanches (sizes 2 and 3) as we intended. Nevertheless, Flow-Py also simulates some avalanches classified as sizes 4 and 5, contingent on the terrain. Moreover, the analyses of the simulated paths enable comparisons of terrain characteristics among different regions in terms of runout length, destructiveness, and the potential avalanche size. When comparing the two test regions, we simulate more paths with a higher destructive size in Sellrain than in Davos. We analyse the paths and thalwegs of each raster cell assigned to a potential release area. Segmentation of cells into a contiguous release area and segmentation of their corresponding thalwegs could provide information about a maximum potential avalanche event.

Validation of ATES and CAT maps would require ground truth data. Therefore, classification maps manually created by experts could be used to verify the algorithm based maps. Additionally, to validate the runout data, mapped avalanches could serve as references.

A further interesting analysis could involve comparing the provided ATES maps with ATES maps derived from the intermediate steps of CAT. This entails using the CAT PRA and RAMMS avalanche runout as input data for the autoATES classifier. Comparison results would show the impact of underlying intermediate steps on ATES and highlight differences between the intermediate steps. Furthermore, we could improve the avalanche results of Flow-Py by implementing the Voellmy friction model to Flow-Py or adopting another, less simplified, process based avalanche simulation model for computing avalanche runout in order to avoid simulating avalanches larger than size 3.

Not only the alpha angle determines the runout length of avalanches simulated by Flow-Py. Adjusting the Flow-Py input parameter Z_{lim}^{δ}, which is directly related to a maximum velocity could further limit the simulated avalanche size. We can estimate the maximum velocity according to the Voellmy friction model as a function of the flow height, slope inclination and friction values, which are determined by the terrain, elevation, annual occurrence and avalanche size. Using lower velocity limits could indirectly integrate the Voellmy friction model.

In future analyses, we could compare ATES with ATH maps. These ATH maps represent avalanche potential combined with consequences when being caught by an avalanche, expressed in continuous values. Unlike the distinct classes in CAT, a comparison of the four ATES classes with continuous values could offer more opportunities for statistical analyses.

The investigation of similarities and differences between the classification maps allows us to identify the limitations and potential for improvement of the methods. It is also crucial to communicate the limitations and differences of the classification maps to users. In general, to reduce the risk of avalanches, it is sufficient to conduct a terrain assessment. The classification maps can assist in this assessment when used correctly, including an awareness of their limitations.

Appendix A

Large Quantities of Data

Table A.1: Area and percentage agreement (of pixel cells) comparing the ATES classes with the four merged CAT classes (variant 3, see section 4.2.3). The results are shown for each test area. The values that show the matching classes (similar as True Positives) are highlighted in bold.

	Sellrain				**Davos**			
CAT	**class** 1	**class 2**	**class 3**	**class 4**	**class 1**	**class 2**	**class 3**	**class 4**
ATES								
class 1 [km²]	**15**	0.41	0.82	0.08	**240**	10	1.7	0.5
	92%	2.6%	5.1%	0.5%	**95%**	4%	0.7%	0.2%
class 2 [km²]	9.7	**3.3**	3.7	0.27	49	**42**	21	1.5
	57%	**19%**	22%	1.6%	43%	**37%**	19%	1.3%
class 3 [km²]	5.3	14	**36**	1.4	14	66	**140**	14
	9.4%	24%	**64%**	2.5%	6.2%	29%	**59%**	6.1%
class 4 [km²]	0.02	0.01	4.2	**6.7**	0.01	0.01	0.16	**0.96**
	0.21%	0.1%	39%	**61%**	1.1%	0.9%	14%	**84%**

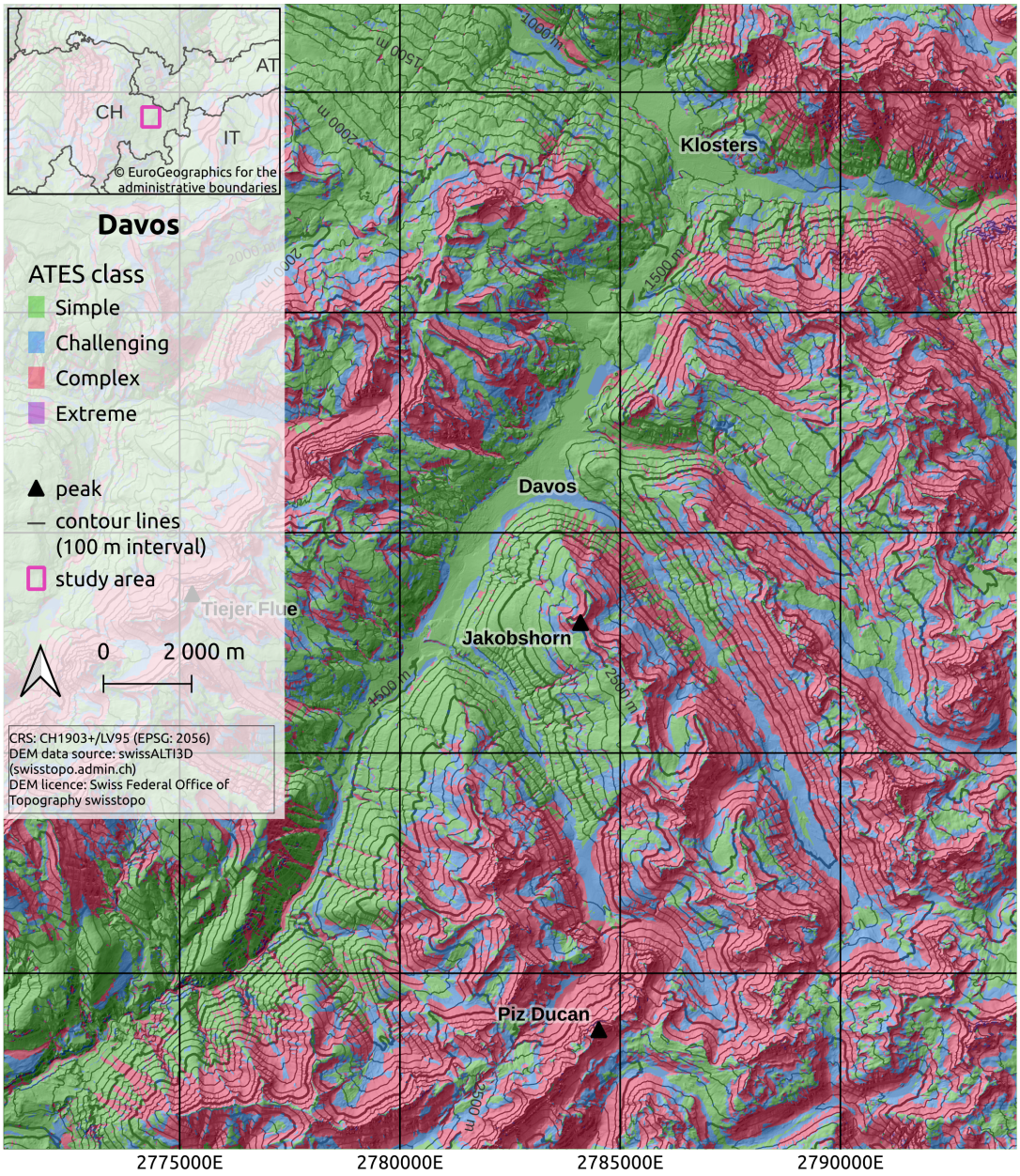

Figure A.1: Classification map ATES in the study area Sellrain. The ATES map classifies the terrain into the four ATES classes 'simple' (green), 'challenging' (blue), 'complex' (red) and 'extreme' (purple).

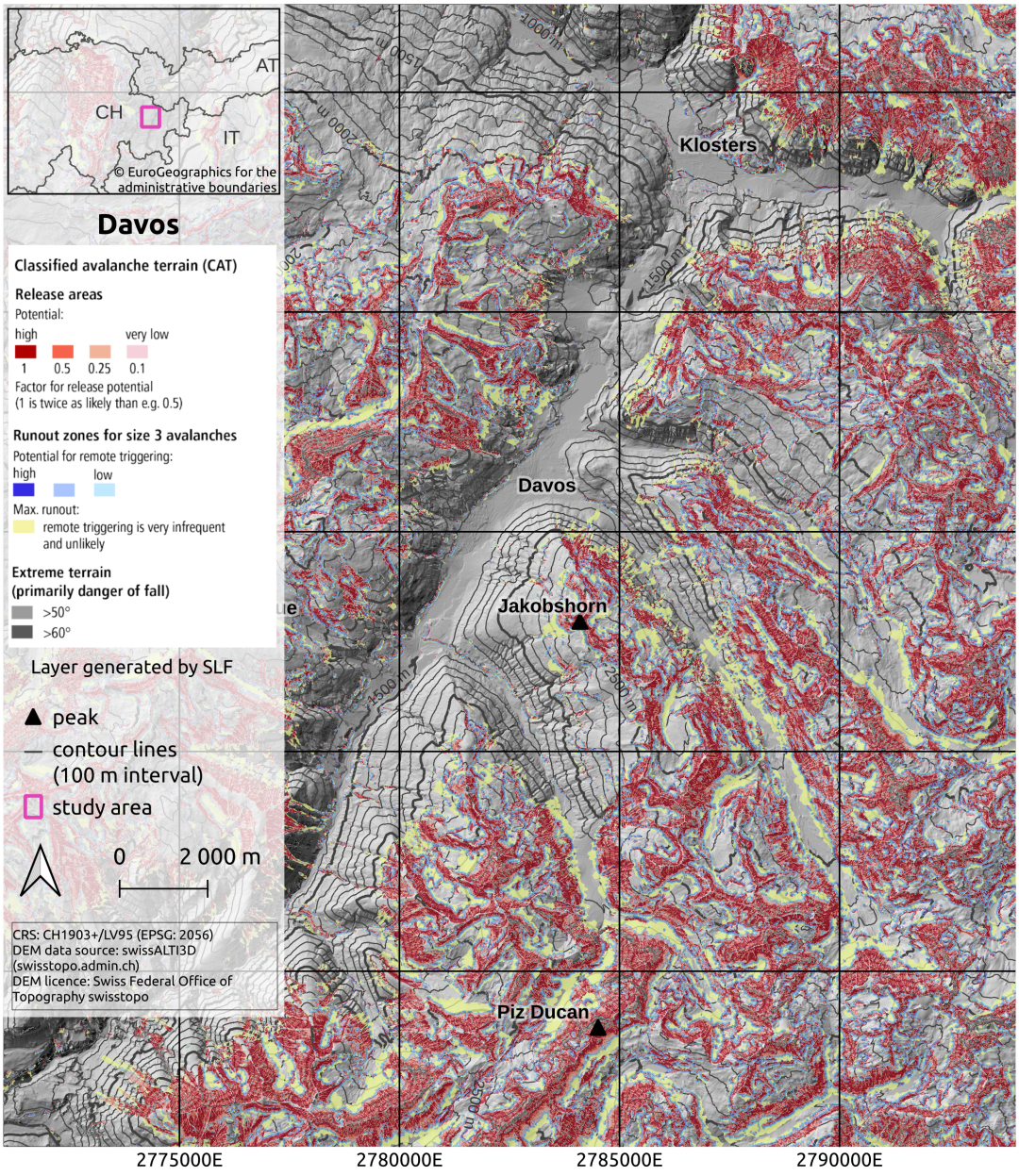

Figure A.2: Classification map CAT in the study area Sellrain. The CAT map shows the potential of release areas (red), remote triggering zones (blue), maximal avalanche runout (yellow) and areas with slopes steeper than 50° (grey) in respective colour schemes.

Bibliography

Bacardit, M., and Coauthors, 2018: AVALANCHE TERRAIN EXPOSURE SCALE MAPPING IN THE PYRENEES: AN EXPANDING PROJECT. *Proceedings of the International Snow Science Workshop*, Innsbruck, Austria, 6.

Bakkehoi, S., U. Domaas, and K. Lied, 1983: Calculation of Snow Avalanche Runout Distance. *Annals of Glaciology*, **4**, 24–29, https://doi.org/10.3189/S0260305500005188.

Bartelt, P., O. Buser, C. Vera Valero, and Y. Bühler, 2016: Configurational energy and the formation of mixed flowing/powder snow and ice avalanches. *Annals of Glaciology*, **57 (71)**, 179–188, https://doi.org/10.3189/2016AoG71A464.

Bartelt, P., Y. Bühler, O. Buser, M. Christen, and L. Meier, 2012: Modeling mass-dependent flow regime transitions to predict the stopping and depositional behavior of snow avalanches. *Journal of Geophysical Research*, **117**, F01 015, https://doi.org/10.1029/2010JF001957.

Bartelt, P., B. Salm, and U. Gruber, 1999: Calculating dense-snow avalanche runout using a Voellmy-fluid model with active/passive longitudinal straining. *Journal of Glaciology*, **45 (150)**, 242–254, https://doi.org/10.3189/S002214300000174X.

Bauerhansl, C., T. Koukal, and K. Schadauer, 2007: Erste österreichweite Waldkarte. *Forstzeitung*, **12**, 26–27.

Bebi, P., A. Bast, K. Helzel, G. Schmucki, N. Brozova, and Y. Bühler, 2022: Avalanche Protection Forest: From Process Knowledge to Interactive Maps. *Protective Forests as Ecosystem-based Solution for Disaster Risk Reduction (Eco-DRR)*, M. Teich, C. Accastello, F. Perzl, and K. Kleemayr, Eds., IntechOpen, https://doi.org/10.5772/intechopen.99514.

Bühler, Y., E. D. Hafner, B. Zweifel, M. Zesiger, and H. Heisig, 2019: Where are the avalanches? Rapid SPOT6 satellite data acquisition to map an extreme avalanche period over the Swiss Alps. *The Cryosphere*, **13 (12)**, 3225–3238, https://doi.org/10.5194/tc-13-3225-2019.

Bühler, Y., S. Kumar, J. Veitinger, M. Christen, A. Stoffel, and Snehmani, 2013: Automated identification of potential snow avalanche release areas based on digital elevation models. *Natural Hazards and Earth System Sciences*, **13 (5)**, 1321–1335, https://doi.org/10.5194/nhess-13-1321-2013.

Bühler, Y., D. von Rickenbach, A. Stoffel, S. Margreth, L. Stoffel, and M. Christen, 2018: Automated snow avalanche release area delineation – validation of existing algorithms and proposition of a new object-based approach for large-scale hazard indication mapping. *Natural Hazards and Earth System Sciences*, **18 (12)**, 3235–3251, https://doi.org/10.5194/nhess-18-3235-2018.

CAA, 2002: *Guidelines for snow avalanche risk determination and mapping in Canada*. Canadian Avalanche Association, Revelstoke, B.C.

CAA, 2016: *Observation guidelines and recording standards for weather, snowpack and avalanches*. 6th ed., Canadian Avalanche Association, Revelstoke, B.C.

Campbell, C., and B. Gould, 2013: A proposed practical model for zoning with the Avalanche Terrain Exposure Scale. *Proceedings of the International Snow Science Workshop*, Grenoble, 385–391.

Campbell, C., and B. Gould, 2014: ATES zoning model. *The Avalanche Journal*, **fall/2014**, 26–29.

Campbell, C., B. Gould, and J. Newby, 2012: ZONING WITH THE AVALANCHE TERRAIN EXPOSURE SCALE. *Proceedings of the International Snow Science Workshop*, Anchorage, Alaska, 450–457.

Campbell, C., and P. Marshall, 2010: MAPPING EXPOSURE TO AVALANCHE TERRAIN. *Proceedings of the International Snow Science Workshop*, Squaw Valley, CA, 556–560.

Christen, M., J. Kowalski, and P. Bartelt, 2010: RAMMS: Numerical simulation of dense snow avalanches in three-dimensional terrain. *Cold Regions Science and Technology*, **63 (1-2)**, 1–14, https://doi.org/10.1016/j.coldregions.2010.04.005.

Delparte, D., M. R. Peterson, J. Perkins, and J. Jackson, 2013: Integrating Gaming Technology to Map Avalanche Hazard. *Proceedings of the International Snow Science Workshop*, Grenoble, 625–631.

D'Amboise, C. J. L., M. Teich, A. Hormes, S. Steger, and F. Berger, 2022a: Modeling Protective Forests for Gravitational Natural Hazards and How It Relates to Risk-Based Decision Support Tools. *Protective Forests as Ecosystem-based Solution*

for Disaster Risk Reduction (Eco-DRR), M. Teich, C. Accastello, F. Perzl, and K. Kleemayr, Eds., IntechOpen, https://doi.org/10.5772/intechopen.99510.

D'Amboise, C. J. L., and Coauthors, 2022b: Flow-Py v1.0: a customizable, open-source simulation tool to estimate runout and intensity of gravitational mass flows. *Geoscientific Model Development*, **15 (6)**, 2423–2439, https://doi.org/10.5194/gmd-15-2423-2022.

EAWS, 2023: European Avalanche Warning Services Glossary. URL https://www.avalanches.org/standards/avalanche-size/.

Engler, M., 2001: Snowcard & Faktorencheck. *Berg und Steigen*, **4/2001**.

ESRI, 2018: Environmental Systems Research Institute (ESRI) ArcGIS software. URL https://desktop.arcgis.com/de/arcmap/latest/tools/spatial-analyst-toolbox/path-distance.htm.

FATMAP, 2023: FATMAP: 3D Map & Guides for Skiing, Hiking and Biking. URL www.fatmap.com.

Feistl, T., P. Bebi, M. Teich, Y. Bühler, M. Christen, K. Thuro, and P. Bartelt, 2014: Observations and modeling of the braking effect of forests on small and medium avalanches. *Journal of Glaciology*, **60 (219)**, 124–138, https://doi.org/10.3189/2014JoG13J055.

Gauer, P., 1999: *Blowing and drifting snow in alpine terrain: a physically-based numerical model and related field measurements*. No. 58, Mitt. Eidg. Institut für Schnee- und Lawinenforschung, Davos, Davos.

Gavaldà, J., I. Moner, and M. Bacardit, 2013: Integrating the ATES into the avalanche information in Aran Valley (Central Pyrenees). *Proceedings of the International Snow Science Workshop*, Grenoble, 381–384.

Google, 2023: 2023 CNES/ Airbus, GeoContent, Landsat / Copernicus, Maxar Technologies, Kartendaten. URL https://www.google.at/maps/.

Gould, B., P. Eng, and C. Campbell, 2014: Modern Snow Avalanche Terrain Mapping for Industrial Projects. *Proceedings of the 2014 Geohazards 6 Conference in Kingston, ON*, Geohazards 6 Conference Committee, 9.

Haegeli, P., I. McCammon, B. Jamieson, C. Israelson, and G. Statham, 2006: THE AVALUATOR – A CANADIAN RULE-BASED AVALANCHE DECISION SUPPORT TOOL FOR AMATEUR RECREATIONISTS. *Proceedings of the International Snow Science Workshop*, Telluride, Colorado, 254–263.

Harvey, S., G. Schmudlach, Y. Bühler, L. Dürr, A. Stoffel, and M. Christen, 2018: Avalanche terrain maps for backcountry skiing in Switzerland. *Proceedings of the International Snow Science Workshop*, Innsbruck, Austria, 1625–1631.

Heim, A., 1932: *Bergsturz und Menschenleben*. Beiblatt zur Vierteljahrsschrift der Naturforschenden Gesellschaft in Zürich, Fretz & Wasmuth, Zürich.

Hesselbach, C., 2023: Adaptation and Application of an Automated Avalanche Terrain Classification in Austria. Masters' Thesis, Universität für Bodenkultur, Wien.

Hirt, C., 2014: Digital Terrain Models. *Encyclopedia of Geodesy*, E. Grafarend, Ed., Springer International Publishing, Cham, 1–6, https://doi.org/10.1007/978-3-319-02370-0_31-1.

Huber, A., and Coauthors, 2023: AutoATES AUSTRIA - TESTING AND APPLICATION OF AN AUTOMATED MODEL-CHAIN FOR AVALANCHE TERRAIN CLASSIFICATION IN THE AUSTRIAN ALPS. *Proceedings of the International Snow Science Workshop*, Bend, Oregon, 929–936.

Jamieson, B., and T. Geldsetzer, 1996: *Avalanche accidents in Canada*, Vol. 4, 1984-1996. Canadian Avalanche Association.

Jang, J.-S. R., C.-T. Sun, and E. Mizutani, 1997: *Neuro-fuzzy and soft computing: a computational approach to learning and machine intelligence*. Prentice Hall, Upper Saddle River, NJ.

Körner, H. J., 1980: The Energy-Line Method in the Mechanics of avalanches. *Journal of Glaciology*, **26 (94)**, 501–505, https://doi.org/10.3189/S0022143000011023.

Larcher, M., 1999: Stop or Go - Entscheidungsstrategie für Tourengeher. *Berg und Steigen*, **4/1999**.

Larsen, H., and Coauthors, 2020a: Development of automated avalanche terrain exposure scale maps: current and future. *Virtual Snow Science Workshop, Fernie, Canada*.

Larsen, H. T., J. Hendrikx, M. Slåtten, and R. Engeset, 2018: GIS based ATES mapping in Norway, a tool for expert guided mapping. *Proceedings of the International Snow Science Workshop*, Innsbruck, Austria, 1604–1608.

Larsen, H. T., J. Hendrikx, M. S. Slåtten, and R. V. Engeset, 2020b: Developing nationwide avalanche terrain maps for Norway. *Natural Hazards*, **103 (3)**, 2829–2847, https://doi.org/10.1007/s11069-020-04104-7.

Lehning, M., H. Löwe, M. Ryser, and N. Raderschall, 2008: Inhomogeneous precipitation distribution and snow transport in steep terrain. *Water Resources Research*, **44 (7)**, W07 404, https://doi.org/10.1029/2007WR006545.

LeVeque, R. J., 2002: *Finite Volume Methods for Hyperbolic Problems*. Cambridge University Press, https://doi.org/10.1017/CBO9780511791253.

Lied, K., and S. Bakkehøi, 1980: Empirical calculations of snow-avalanche run-out distance based on topographic parameters. *Journal of Glaciology*, **26**, 165–177.

Liu, Y., Y. Zhou, S. Wen, and C. Tang, 2014: A Strategy on Selecting Performance Metrics for Classifier Evaluation:. *International Journal of Mobile Computing and Multimedia Communications*, **6 (4)**, 20–35, https://doi.org/10.4018/IJMCMC.2014100102.

Maggioni, M., and U. Gruber, 2003: The influence of topographic parameters on avalanche release dimension and frequency. *Cold Regions Science and Technology*, **37 (3)**, 407–419, https://doi.org/10.1016/S0165-232X(03)00080-6.

Margreth, S., 2004: Die Wirkung des Waldes bei Lawinen. *Forum für Wissen*, 21–26.

Martí, G., L. Trabal, J. M. Vilaplana, and C. García-Sellés, 2013: Avalanche terrain exposure classification for avalanche accidents in Catalan Pyrenees. *Proceedings of the International Snow Science Workshop*, Grenoble.

McClung, D., and P. A. Schaerer, 2006: *The avalanche handbook*. 3rd ed., Mountaineers Books, Seattle, WA.

Mitterer, C., and J. Schweizer, 2013: Analysis of the snow-atmosphere energy balance during wet-snow instabilities and implications for avalanche prediction. *The Cryosphere*, **7 (1)**, 205–216, https://doi.org/10.5194/tc-7-205-2013.

Moner, I., J. Gavaldà, and M. Bacardit, 2018: ATES mapping and typical problems in avalanche accidents or close-calls in Val d'Aran, Central Pyrenees. *Proceedings of the International Snow Science Workshop*, Innsbruck, Austria, 1216–1220.

Munter, W., 1997: *3 x 3 Lawinen: entscheiden in kritischen Situationen*. Agentur Pohl und Schellhammer, Garmisch-Partenkirchen.

Neuhauser, M., C. D'Amboise, M. Teich, A. Kofler, A. Huber, R. Fromm, and J. T. Fischer, 2021: Flow-Py: routing and stopping of gravitational mass flows. Zenodo, language: en, https://doi.org/10.5281/ZENODO.5027275.

Nåfält, S., 2016: Assessing avalanche risk by terrain analysis – An experimental GIS-approach to The Avalanche Terrain Exposure Scale (ATES). Bachelor Thesis, Lund University, Lund.

Oesterle, F., M. Tonnel, A. Wirbel, and J.-T. Fischer, 2024: avaframe/AvaFrame: Version 1.8. Zenodo, https://doi.org/10.5281/ZENODO.10664598.

Pedregosa, F., and Coauthors, 2011: Scikit-learn: Machine Learning in Python. *Journal of Machine Learning Research*, **12**, 2825–2830.

Pielmeier, C., D. Silbernagel, L. Dürr, and T. Stucki, 2014: APPLYING THE AVALANCHE TERRAIN EXPOSURE SCALE IN THE SWISS JURA MOUNTAINS. *Proceedings of the International Snow Science Workshop*, Banff, 883–889.

Plattner, C., L. N. Braun, and A. Brenning, 2004: The spatial variability of snow accumulation on Vernagtferner, Austrian Alps, in Winter 2003/2004. *Zeitschrift für Gletscherkunde und Glazialgeologie*, **39**, 43–57.

Rudolf-Miklau, F., and S. Sauermoser, Eds., 2011: *Handbuch technischer Lawinenschutz*. 1st ed., Ernst & Sohn, Berlin, Germany.

Salm, B., 1993: Flow, flow transition and runout distances of flowing avalanches. *Annals of Glaciology*, **18**, 221–226, https://doi.org/10.3189/S0260305500011551.

Salm, B., 2004: A short and personal history of snow avalanche dynamics. *Cold Regions Science and Technology*, **39 (2-3)**, 83–92, https://doi.org/10.1016/j.coldregions.2004.06.004.

Sappington, J. M., K. M. Longshore, and D. B. Thompson, 2007: Quantifying Landscape Ruggedness for Animal Habitat Analysis: A Case Study Using Bighorn Sheep in the Mojave Desert. *The Journal of Wildlife Management*, **71 (5)**, 1419–1426, https://doi.org/10.2193/2005-723.

Sauermoser, S., 2006: AVALANCHE HAZARD MAPPING - 30 YEARS EXPERIENCE IN AUSTRIA. *Proceedings of the International Snow Science Workshop*, Telluride, Colorado, 314–321.

Sauermoser, S., M. Granig, K. Kleemayr, and S. Margreth, 2014: Avalanche dynamics: models and impact. *The Technical Avalanche Protection Handbook*, F. Rudolf-Miklau, S. Sauermoser, and A. I. Mears, Eds., 1st ed., Wiley, 55–90, https://doi.org/10.1002/9783433603840.ch03.

Schmudlach, G., and J. Köhler, 2016a: Automated avalanche risk rating of backcountry ski routes. *Proceedings of the International Snow Science Workshop*, Breckenbridge, Colorado, 450–456.

Schmudlach, G., and J. Köhler, 2016b: Method for an automatized avalanche terrain classification. *Proceedings of the International Snow Science Workshop*, Breckenbridge, Colorado, 729–736.

Schmudlach, G., K. Winkler, and J. Köhler, 2018: Quantitative risk reduction method (QRM), a data-driven avalanche risk estimator. *Proceedings of the International Snow Science Workshop*, Innsbruck, Austria, 1272–1278.

Schumacher, J., H. Toft, J. P. McLean, M. Hauglin, R. Astrup, and J. Breidenbach, 2022: The utility of forest attribute maps for automated Avalanche Terrain Exposure Scale (ATES) modelling. *Scandinavian Journal of Forest Research*, **37 (4)**, 264–275, https://doi.org/10.1080/02827581.2022.2096921.

Schweizer, J., 1999: Review of dry snow slab avalanche release. *Cold Regions Science and Technology*, **30 (1-3)**, 43–57, https://doi.org/10.1016/S0165-232X(99)00025-7.

Schweizer, J., P. Bartelt, and A. Van Herwijnen, 2015: Snow Avalanches. *Snow and Ice-Related Hazards, Risks, and Disasters*, Elsevier, 395–436, https://doi.org/10.1016/B978-0-12-394849-6.00012-3.

Schweizer, J., J. Bruce Jamieson, and M. Schneebeli, 2003: Snow avalanche formation. *Reviews of Geophysics*, **41 (4)**, 2002RG000123, https://doi.org/10.1029/2002RG000123.

Schweizer, J., and M. Lütschg, 2001: Characteristics of human-triggered avalanches. *Cold Regions Science and Technology*, **33 (2-3)**, 147–162, https://doi.org/10.1016/S0165-232X(01)00037-4.

Sharp, E., 2018: EVALUATING THE EXPOSURE OF HELISKIING SKI GUIDES TO AVALANCHE TERRAIN USING A FUZZY LOGIC AVALANCHE SUSCEPTIBILITY MODEL. Masters' Thesis, University of Leeds, School of Geography, Leeds, UK, https://doi.org/10.13140/RG.2.2.18673.94567.

Sharp, E., P. Haegeli, and M. Welch, 2018: PATTERNS IN THE EXPOSURE OF SKI GUIDES TO AVALANCHE TERRAIN. *Proceedings of the International Snow Science Workshop*, Innsbruck, Austria.

Statham, G., 2008: AVALANCHE HAZARD, DANGER AND RISK – A PRACTICAL EXPLANATION. *Proceedings of the International Snow Science Workshop*, Whistler, Canada, 224–227.

Statham, G., and C. Campbell, 2023: THE AVALANCHE TERRAIN EXPOSURE SCALE V.2. *Proceedings of the International Snow Science Workshop*, Bend, Oregon, 597–605.

Statham, G., B. McMahon, and I. Tomm, 2006: The avalanche terrain exposure scale. *Proceedings of the International Snow Science Workshop*, Telluride, Colorado, 491–497.

Sykes, J., H. Toft, P. Haegeli, and G. Statham, 2024: Automated Avalanche Terrain Exposure Scale (ATES) mapping – local validation and optimization in western Canada. *Natural Hazards and Earth System Sciences*, **24 (3)**, 947–971, https://doi.org/10.5194/nhess-24-947-2024.

Techel, F., F. Jarry, G. Kronthaler, S. Mitterer, P. Nairz, M. Pavšek, M. Valt, and G. Darms, 2016: Avalanche fatalities in the European Alps: long-term trends and statistics. *Geographica Helvetica*, **71 (2)**, 147–159, https://doi.org/10.5194/gh-71-147-2016.

Techel, F., C. Mitterer, E. Ceaglio, C. Coléou, S. Morin, F. Rastelli, and R. S. Purves, 2018: Spatial consistency and bias in avalanche forecasts – a case study in the European Alps. *Natural Hazards and Earth System Sciences*, **18 (10)**, 2697–2716, https://doi.org/10.5194/nhess-18-2697-2018.

Teich, M., P. Bartelt, A. Grêt-Regamey, and P. Bebi, 2012: Snow Avalanches in Forested Terrain: Influence of Forest Parameters, Topography, and Avalanche Characteristics on Runout Distance. *Arctic, Antarctic, and Alpine Research*, **44 (4)**, 509–519, https://doi.org/10.1657/1938-4246-44.4.509.

Thumlert, S., and P. Haegeli, 2018: Describing the severity of avalanche terrain numerically using the observed terrain selection practices of professional guides. *Natural Hazards*, **91 (1)**, 89–115, https://doi.org/10.1007/s11069-017-3113-y.

Tiwari, S., S. Dixit, V. Kumar, and A. Rastogi, 2022: Analogy among Center of Gravity, Center of Mass, and Centroid of Rigid body: Analysis of Formula for Their Respective Calculation as per Configuration of Body and Utilization in Composite Application. *Applied Functional Materials*, **2 (2)**, 7–13, https://doi.org/10.35745/afm2022v02.02.0002.

Toft, H. B., 2022: Potential Release Area Algorithm. URL https://github.com/hvtola/potential_release_areas.

Toft, H. B., J. Sykes, A. Schauer, J. Hendrikx, and A. Hetland, 2023: AutoATES v2.0: Automated avalanche terrain exposure scale mapping. Natural Hazards and Earth System Sciences Discussions, https://doi.org/10.5194/nhess-2023-114.

UNESCO, Ed., 1981: *Avalanche atlas - Illustrated International Avalanche Classification*. No. 2, Natural hazards, Paris, France.

Van Rossum, G., J. Drake, and L. Fred, 1995: *Python reference manual*. Centrum voor Wiskunde en Informatica Amsterdam.

Veitinger, J., R. S. Purves, and B. Sovilla, 2016: Potential slab avalanche release area identification from estimated winter terrain: a multi-scale, fuzzy logic approach. *Natural Hazards and Earth System Sciences*, **16 (10)**, 2211–2225, https://doi.org/10.5194/nhess-16-2211-2016.

Voellmy, A., 1955: Über die Zerstörungskraft von Lawinen. https://doi.org/10.5169/SEALS-61891.

Vontobel, I., 2011: Geländeanalysen von Unfalllawinen. Masters' Thesis, Department of Geography, University of Zurich, Zurich.

Wichmann, V., 2017: The Gravitational Process Path (GPP) model (v1.0) – a GIS-based simulation framework for gravitational processes. *Geoscientific Model Development*, **10 (9)**, 3309–3327, https://doi.org/10.5194/gmd-10-3309-2017.

Winstral, A., K. Elder, and R. E. Davis, 2002: Spatial Snow Modeling of Wind-Redistributed Snow Using Terrain-Based Parameters. *Journal of Hydrometeorology*, **3 (5)**, 524–538, https://doi.org/10.1175/1525-7541(2002)003⟨0524:SSMOWR⟩2.0.CO;2.

Zadeh, L., 1965: Fuzzy sets. *Information and Control*, **8 (3)**, 338–353, https://doi.org/10.1016/S0019-9958(65)90241-X.